Floaters on Faraday waves: Clustering and Heterogeneous Flow

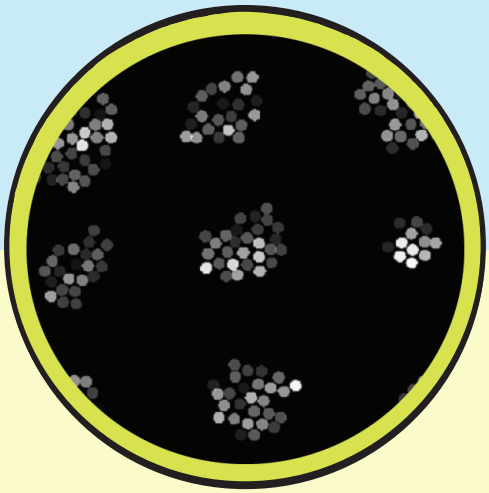

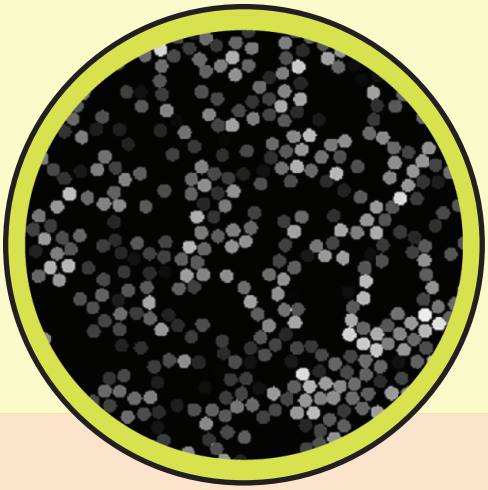

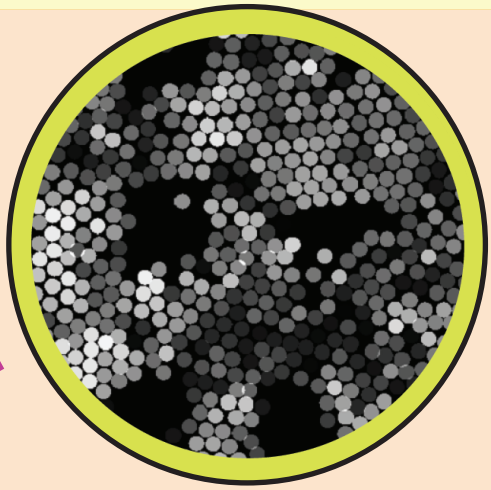

Ceyda Sanlı

Floaters on Faraday Waves:

Clustering and Heterogeneous Flow

Ceyda Sanli

Samenstelling promotiecommissie:

Prof. dr. G. van der Steenhoven (voorzitter)	Universiteit Twente
Prof. dr. Detlef Lohse (promotor)	Universiteit Twente
Dr. Devaraj van der Meer (assistent-promotor)	Universiteit Twente
Prof. dr. Karen E. Daniels	North Carolina State University
Prof. dr. J. Frits Dijksman	Universiteit Twente
Dr. Dirk van den Ende	Universiteit Twente
Prof. dr. Stefan Luding	Universiteit Twente
Dr. Peter Schall	Universiteit van Amsterdam

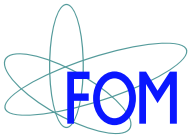

The work in this thesis was carried out at the Physics of Fluids group of the Faculty of Science and Technology of the University of Twente. It is part of the research programme of the Foundation for Fundamental Research on Matter (FOM), which is financially supported by the Netherlands Organisation for Scientific Research (NWO).

Nederlandse titel:
Drijvende deeltjes op Faraday golven: over clustering en heterogene dynamica.

Publisher:
Ceyda Sanlı, Physics of Fluids, University of Twente,
P.O. Box 217, 7500 AE Enschede, The Netherlands.
pof.tnw.utwente.nl
cedaysan@gmail.com & ceydasanli.com (WordPress)

Cover Illustration: Ceyda Sanlı & Deniz Çakır

ISBN: 978-90-365-3359-1

FLOATERS ON FARADAY WAVES:

CLUSTERING AND HETEROGENEOUS FLOW

PROEFSCHRIFT

ter verkrijging van
de graad van doctor aan de Universiteit Twente,
op gezag van de rector magnificus,
Prof. dr. H. Brinksma,
volgens besluit van het College voor Promoties
in het openbaar te verdedigen
op vrijdag 6 juli 2012 om 16.45 uur

door

Ceyda Sanlı
geboren op 9 januari 1983
te Kayseri, Türkiye

Dit proefschrift is goedgekeurd door de promotor:

Prof. dr. rer. nat. Detlef Lohse

en de assistent-promotor:

Dr. Devaraj van der Meer

BUT STILL TRY, FOR WHO KNOWS WHAT IS POSSIBLE…

MICHAEL FARADAY

Dedicated to the memories of my friend Göknur Temiz and my grandfather Ali Kırgezen.

Ve, çok sevdiğim biricik Denizciğime...

CONTENTS

1

General introduction

Floating objects can be found in our life in various situations. However, we may hardly recognize their surprising behavior. When you pour your favorite bubbly drink into a glass cup you experience that, a few seconds later, bubbles aggregate at the free surface and most of them position at the wall of the glass cup. (Just do it to realize that this is indeed what happens! Then, why don't you also try to pour your drink into a plastic cup and observe the position of the bubbles in that case?) Furthermore, if you take a vacation nearby a sea region you probably experience that, in a windy day, a lump of waste or a collection of sea plants floats on a wavy sea surface. A careful observer can recognize some surprising behavior of such a group of floaters. The motion of the group suggests that they may move in a certain direction rather than randomly. Sometimes, they change their direction with respect to the surface wave elevation, and sometimes they just oscillate with the wave.

Let's discuss the characteristics of such floaters based on these two different examples, namely bubbles floating at a liquid-air interface and floater clusters moving on a surface wave. The first example is well-known as the "Cheerios effect". The name is inspired by breakfast cereals floating on milk: The cereals aggregate and either stay in the middle of the surface or move to the wall of the breakfast bowl [1]. Both the agglomeration and the motion towards the wall are induced by surface ten-

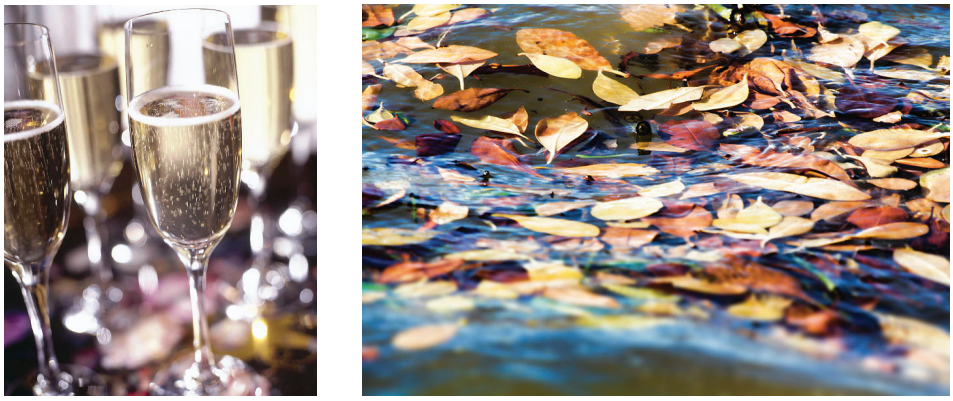

Figure 1.1: Champagne bubbles, aggregated at the wall of a wine glass, and accumulated leaves floating on a wavy sea surface [3].

sion. The surface profile around each floater is not axisymmetric in the presence of an other floater so that the floaters are driven to each other. This attractive interaction among floaters is called gravity-induced capillary interaction. (A repulsive interaction is also possible, but only if the floaters have different wetting properties or densities.) Similarly, the wall disturbs the surface profile, and so it drives an attraction (or repulsion) between the floaters and the wall. Both floater-to-floater and floater-to-wall interactions can be well formulated when the meniscus deformation is small by minimizing the total potential energy (both gravity and surface tension) of the floaters [1, 2]. In the present Thesis, "floater" refers to an object floating on a liquid, which is exposed to not only gravity and Archimedes' buoyancy, but also surface tension.

Without applying any calculation, one can conceptually understand [1] why a bubble floating on champagne is attracted by the wall of a wine glass as shown in Fig. 1.1. Consider a bubble floating on champagne. In the static case, there are three vertical forces acting on the bubble, namely the weight, the buoyancy, and the surface tension. Since the bubble is much lighter than the champagne, the buoyancy is much larger than its weight. To create a balance, the surface tension acts downwards which creates a convex-shaped surface profile around the bubble. However, there is a physical limit such that the surface tension cannot bend the meniscus beyond a certain angle. Therefore, there is an excess upwards force due to lack of downwards forces. On the other side, the glass wall creates a meniscus with also a convex-shape

so that the free surface is not flat, but it increases towards the wall [1]. Therefore, by the help of excess upwards force, the bubble moves towards the wall so that there is an attraction between a bubble and a glass wall. On the other hand, there is a repulsion generated between the bubble and the wall of a plastic cup since the plastic wall creates a meniscus with a concave shape, and so the bubble tends to stay in the middle of the interface.

Bubble aggregation as seen in Fig. 1.1 can be explained in a similar way. As described above, the meniscus around each bubble is convex. So, the interface rises towards the contacts of the bubbles. By considering that there is an excess upwards force for each bubble, the bubbles utilize this by coming towards each other so that an attractive interaction is generated.

The Cheerios effect and floater agglomerations have been studied experimentally, theoretically, and numerically for some decades [2, 4–8], and the attractive capillary interaction, in certain limits, has been well-formulated [9–11]. Recently, scientists have found some more interesting behavior of a floater raft, a monolayer of floaters at a fluid-fluid interface. Heterogeneity of the floater packing in the raft has been characterized, and the role of the cohesion held together by capillary forces has been investigated [12]. Furthermore, it has been found that such a cohesive floater raft exhibits granular behavior [13]: The stress profile of the compressed floater raft shows an exponential decay away from the boundaries. This is very similar to the Janssen effect [14, 15] in a granular silo, which states that the vertical pressure in the silo is not hydrostatic, but it grows as $1-\exp(-z/\alpha)$ with increasing depth of the silo z until a certain constant value. (Here, α is a constant composed of geometrical properties of the silo and frictional coefficients.)

Besides their scientific interest, floater rafts and other agglomerations of cohesive grains which are trapped at a fluid-fluid interface have various practical usages. Examples are the separation processes of ore particles in aqueous systems [16], removing impurities in a melted metal surface [17, 18], and removing plastic contaminants of a paper pulp by injecting gas bubbles [19, 20]. This last example utilizes the attractive interaction between the contaminants and the bubbles which aggregate and rise onto the pulp surface since their densities are lower than the pulp. All these examples have in common that the interfaces of interest are generally neither static nor flat. The theories on the other hand assume flat and static interfaces. This brings us to the question: How does the interface dynamics influence the floater agglomerations?

Consider that the interface is not flat, but curved and that its shape varies in time. This would be the case when we observe the motion of accumulated waste or plants on a sea surface in a windy day, which is the second example introduced in the first paragraph. So, to be more specific, let us now examine accumulations of floaters on a surface wave. Floaters, tracer particles and macroscopic beads moving on surface waves have been studied for some systems. Diffusive, erratic, and clustering behavior of floaters have been analyzed in several different regimes [21–24], from which the enormous complexity of the floater dynamics and the great challenges in understanding them become clear. This complexity comes from both the characteristics of a surface wave and from floater-to-wave interactions, as well as the attractive capillary interaction discussed above for macroscopic floaters. To restrict the problem and to increase the reproducibility, one can create well-controlled periodic surface waves, by using a standing Faraday wave setup [25, 26], and focus on the motion of macroscopic beads. For a small group of micron or millimeter size spheres, surprisingly, a very robust drift motion towards a standing Faraday wave maximum has been observed [27] (and also towards its minimum for certain cases).

The exact mechanism of a single floater on a standing wave, and so the origin of the drift motion have been understood and formulated in Ref. [27]. There are two contributions to the drift for a single floater: a motion driven by a curved surface and inertia effects. The first one can be easily observed in the static case by a tabletop experiment. Take a drop on a desk, and then put a small bubble on its inclined surface. You see that the bubble climbs up, similar to the way in which bubbles on your drink climb up the meniscus generated at the wall of a glass cup due to the excess upward force [1] as was discussed above. As a reminder, the buoyancy force for the bubble is larger than the total of its weight and the applied surface tension force, which is downwards in this case since the bubble is hydrophilic (wetting) and lighter than the carrier liquid. The opposite scenario is expected for an hydrophobic (non-wetting) heavy particle, and so the particle slides down the inclined surface of the drop [28].

The second contribution to the drift comes from an inertia difference between a floater and the oscillating carrier liquid. For a standing wave, a liquid particle at the surface just oscillates together with the wave. However, when a floater is placed on the wave, an inertial effect is generated such that the floater does not simply oscillate, but in addition drifts. There are three fundamental contributions to this inertial effect: The density difference between the floater and its carrier liquid, the surface tension, and an effective weight of the floater imposed by varying both the direction

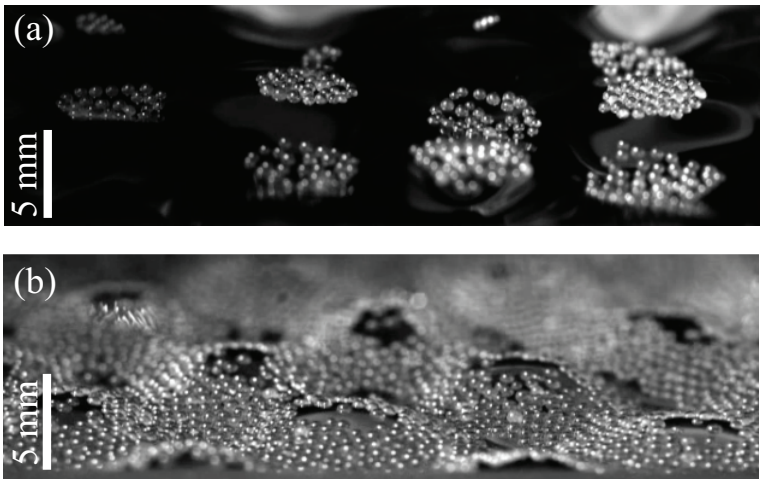

Figure 1.2: Floating patterns of millimeter size hydrophilic spheres form on a standing Faraday wave. The carrier liquid is pure water and the spheres are slightly heavier than the water. (a) A few identical floaters organize into clusters at the antinodes of the standing Faraday wave, where there is maximum vertical displacement in the wave amplitude. (b) Just by increasing the number of floaters on the surface, the same spheres spontaneously accumulate at the nodal lines of the wave, thereby completely inverting the self-organized particle pattern on the wave. The white bars indicate a length scale of 5 mm.

and the magnitude of the surface wave acceleration within a standing wave cycle. These all combinedly vary the submerged part of the floater such that it is not in the equilibrium situation where it would be if no surface wave would be present. The deviations from equilibrium during a single cycle do not sum up to zero, but to a finite value, i.e., the floater drifts. The process described here has been mathematically well-formulated for a one-dimensional standing wave in Ref. [27] where also the form of the corresponding drift force has been given. However, this approach is valid for a single floater and, again in Ref. [27], it has been shown experimentally that the formalism works up to a limited number of floaters. For larger numbers the approach is bound to fail because the attractive capillary interaction has not been included. Fig. 1.2 presents our experimental observations of millimeter size hydrophilic spheres, that are slightly heavier than the carrier liquid pure water, float on a standing Faraday wave.

For these spheres, the single particle drift is towards the amplitude maximum (antinodes) of the standing wave, where there is maximum vertical displacement in

the wave amplitude. Therefore, a few of these identical spheres indeed cluster at the antinodes [Fig. 1.2(a)]. However, larger numbers of the same spheres cluster at the nodal line of the wave [Fig. 1.2(b)], where there is no vertical displacement. It is good to stress that the inverted nodal pattern forms just by increasing the number of floating spheres, and none of the driving parameters, i.e., neither the wavelength nor amplitude of the wave, is varied. This makes our observation stand apart from other systems with pattern formation and inversion such as vegetation patterns including spots, stripes, and holes due to the variation in the aridity [29], and the pattern inversion in the accumulation of dry granular particles from the nodes of a vertically shaken plate (Chladni patterns) to the antinodes when the driving acceleration is dropped below the acceleration of gravity or when the air drag becomes dominant for the particle motion [30, 31].

The main objective of this thesis is to combine these two independent research problems, namely a static densely packed floater raft and initially loosely packed floaters on surface waves into a single experiment. Before going into our research problem in more detail, we will provide some background information for the reader in Chapter 2. Here, we will introduce floaters at a static interface, i.e., static balance and capillary interaction, and floaters at a moving interface, i.e., a single floater drift.

Subsequently, we focus on how the two main mechanisms driving the dynamic floater raft, namely the drift of a single floater due to the standing wave and the attractive capillary interaction among the floaters, change the system with increasing floater number. To this end, in Chapter 3, we will present our experimental observations of spherical macroscopic particles floating on a standing Faraday wave. By changing the floater number in each experiment, we will show that a floater pattern spontaneously forms, and that its characteristics highly depend on the floater number: The floater pattern surprisingly can be inverted just by increasing the floater number. Previous work on Faraday waves with floaters [27, 28] cannot be generalized to explain this pattern inversion. Therefore, to understand the floater dynamics even further and to check the agreement between our observations and the combined theories, we will develop an energy argument. The approach is based on calculating the potential energy of artificially created patterns inspired by the observed patterns. Finally, we will compare the experimental results and the energy argument.

After discussing the spontaneous pattern formation of the floaters by increasing the floater number both experimentally and theoretically, Chapter 4 aims to quantify the floater patterns as a function of the floater number. Our underlying motivation

is that characterizing the patterns morphologically can give us an understanding why the system prefers to form a certain configuration at a certain floater number. Here, the standing Faraday wave wavelength is much larger than the floater size so that both these two length scales are expected to play a role in the resulting patterns. Therefore, the morphology of the patterns is evaluated in two different ways: Global analysis by calculating the Minkowski functionals, which is the technique borrowed from the astrophysicists, and local analysis by the pair correlation function and the local bond orientational order parameter, which both are used extensively in soft condensed matter for many purposes. Consequently, we will show that these three distinct techniques successfully clarify the differences in the patterns when the floater number increases.

In Chapter 5, we will turn to a different regime. In that case, we will be out of the standing Faraday wave limit. Instead, we work with nonlinear chaotic waves, namely capillary Faraday waves with a wavelength of the order of the floater size. In this case, the single particle drift force is not present and the floaters are mainly driven by the attractive capillary force together with erratic driving forces due to the capillary Faraday waves. When the floaters are densely packed on the capillary Faraday waves, we will demonstrate that their dynamics is highly heterogeneous in space and irregular in time. The heterogeneities will be analyzed by a technique borrowed from the literature, the four-point dynamic susceptibility. Furthermore, we observe that the flow is composed of floater domains: Small floater groups initially moving together, break-up in a certain way at some time later. By using the technique we develop in Chapter 4, i.e., utilizing the Minkowski functionals, we will quantify the morphology of the break-up process. More specifically, we will calculate the size of the groups and their break-up time. The break-up time will be evaluated for different group.

Finally, Chapter 6 presents some overall conclusions and suggests possibilities for further research studies and applications.

References

[1] D. Vella and L. Mahadevan, “The Cheerios effect”, Am. J. Phys. **73**, 817–825 (2005).

[2] D. Y. C. Chan, J. D. Henry, Jr., and L. R. White, “The interaction of colloidal particles collected at fluid interfaces”, J. Colloid Interface Sci. **79**, 410–418 (1981).

[3] The photo reference person is Chiara Shannon (left), and the photographer is Douglas Barnard (right).

[4] M. M. Nicolson, "The interaction betweeen floating particles", Proc. Cambridge Philos. Soc. **45**, 288–295 (1949).

[5] J. B. Keller, "Surface tension force on a partly submerged body", Phys. Fluids **10**, 3009–3010 (1998).

[6] P. A. Kralchevsky and K. Nagayama, "Capillary interactions between particles bound to interfaces, liquid films and biomembranes", Adv. Colloid Interface Sci. **85**, 145–192 (2000).

[7] D. Stamou, and C. Duschl, and D. Johannsmann, "Long-range attraction between colloidal spheres at the air-water interface: The consequence of an irregular meniscus", Phys. Rev. E **62**, 5263–5272 (2000).

[8] A. Vincze, A. Agod, J. Kartész, M. Zrínyi, and Z. Hórvölgyi, "Aggregation kinetics in two dimensions: Real experiments and computer simulations", J. Chem. Phys. **114**, 520–529 (2001).

[9] N. D. Vassileva, "Behavior of 2D aggregates in shear flow", PhD Thesis, University of Twente (2006).

[10] N. D. Vassileva, D. van den Ende, F. Mugele, and J. Mellema, "Capillary forces between spherical particles floating at a liquid-liquid interface", Langmuir **21**, 11190–11200 (2005).

[11] M.-J. Dalbe, D. Cosic, M. Berhanu, and A. Kudrolli, "Aggregation of frictional particles due to capillary attraction", Phys. Rev. E **83**, 051403-1–10 (2011).

[12] M. Berhanu and A. Kudrolli, "Heterogeneous structure of granular aggregates with capillary interactions", Phys. Rev. Lett. **105**, 098002-1–4 (2010).

[13] P. Cicuta and D. Vella, "Granular character of particle rafts", Phys. Rev. Lett. **102**, 138302-1–4 (2009).

[14] H. A. Janssen, Zeitschr. d.Vereines deutscher Ingenieure **39**, 1045 (1895).

[15] M. Sperl, "Experiments on corn pressure in silo cellstranslation and comment of Janssens paper from 1895", Granular Matter **8**, 59–65 (2006).

[16] J. D. Henry, M. E. Prudich, and K. R. Vaidyanathan, "Novel separation processes for solid/liquid separations in coal derived liquids", Separa-

tion and Purification Reviews **8**, 81–118 (1979).

[17] H. Shibata, H. Yin, and T. Emi, "The capillary effect promoting collision and agglomeration of inclusion particles at the inert gas-steel interface", Phil. Trans. R. Soc. Lond. A **356**, 957–966 (1998).

[18] K. Nakajima and S. Mizoguch, "Capillary interaction between inclusion particles on the 16Cr stainless steel melt surface", Metall. Mater. Trans. B **32**, 629–641 (2001).

[19] J. Ralston, D. Fornasiero, and R. Hayes, "Bubble-particle attachment and detachment in flotation", Int. J. Miner. Process. **56**, 133–164 (1999).

[20] A. V. Nguyen and H. J. Schulze, "Colloidal Science of Flotation (Surfactant Science)", CRC Press, New York (2003).

[21] K. Herterich and K. Hasselmann, "The horizontal diffusion of tracers by surface waves", J. Phys. Ocean. **12**, 704–711 (1982).

[22] R. Ramshankar, D. Berlin, and J. P. Gollub, "Transport by capillary waves. Part I: Particle trajectories", Phys. Fluids A **2**, 1956–1965 (1990); R. Ramshankar and J. P. Gollub, "Transport by capillary waves. Part II: Scalar dispersion and structure of the concentration field", Phys. Fluids A **3**, 1344–1350 (1991); O. N. Mesquita, S. Kane, and J. P. Gollub, "Transport by capillary waves: Fluctuating Stokes drift", Phys. Rev. A **45**, 3700–3705 (1992).

[23] N. Tokugawa, M. Umeki, and T. Kambe, "Statistical analysis of particle drifts on Faraday waves", Fluid Dyn. Res. **16**, 43–55 (1995).

[24] J. Larkin, M. M. Bandi, A. Pumir, and W. I. Goldburg, "Power-law distributions of particle concentration in free-surface flows", Phys. Rev. E **80**, 066301-1–5 (2009).

[25] S. Douady, "Experimental study of the Faraday instability", J. Fluid Mech. **221**, 383–408 (1990).

[26] E. G. T. Bosch, "An experimental investigation of Faraday waves and spatio-temporal chaos", PhD Thesis, Technical University of Eindhoven (1995);

[27] G. Falkovich, A. Weinberg, P. Denissenko, and S. Lukaschuk, "Floater clustering in a standing wave", Nature (London) **435**, 1045–1046 (2005).

[28] S. Lukaschuk, P. Denissenko, and G. Falkovich, "Nodal patterns of floaters in surface waves", Eur. Phys. J. Special Topics **145**, 125–136 (2007).

[29] J. von Hardenberg, E. Meron, M. Shachak, and Y. Zarmi, "Diversity of Vegetation Patterns and Desertification", Phys. Rev. Lett. **198101**-1–4 (2001).

[30] H. J. van Gerner, M. A. van der Hoef, D. van der Meer, and K. van der Weele, "Inversion of Chladni patterns by tuning the vibrational acceleration", Phys. Rev. E **82**, 012301-1–4 (2010).

[31] H. J. van Gerner, K. van der Weele, M. A. van der Hoef, and D. van der Meer, "Air-induced inverse Chladni patterns", J. Fluid Mech. **689**, 203–220 (2011).

2

PLAYING WITH SURFACE TENSION UNDER GRAVITY * †

It may seem that macroscopic spheres floating at a liquid-air interface constitute one of the simplest systems to demonstrate in a fluid physics laboratory. However, even by playing with one sphere or a few spheres having different physical properties it is easy to demonstrate the complexity of the system. Furthermore, when you take a piece of paper and a pen, and then try to explain your observations analytically you may be lost in the physical constants and parameters. For more fun, a sphere can be placed on a surface standing wave. Similar to the static case, you will see very complex phenomena in the presence of the wave due to the additional complexities the latter induces an amplitude. Surprisingly, you will see that the sphere prefers to be either at a wave amplitude maximum or an amplitude minimum depending on its physical property. Here, using the results from the literature, we will summarize the intricate dynamics of the floaters. This Chapter will thus provide background information for readers who are not expert on "spheres floating at static and moving interfaces". We also aim to elucidate some important points that are hidden in the literature, to serve as a guide to the reader for the following

*Part of this work will be submitted as Ceyda Sanlı, Detlef Lohse, and Devaraj van der Meer, "Playing with surface tension under gravity: A close looking on capillary interaction and a particle drift due to a standing wave", to Am. J. Phys.

†We acknowledge Jacco Snoeijer to introduce us to the world of small particles.

Chapters.

2.1 Introduction

Objects can float on a surface if their density is lower than the density of the carrier fluid, which is very well-known as Archimedes' law of buoyancy. However, small objects violate this, i.e., heavy objects can float by the help of surface tension. When a small heavy sphere floats at a liquid-air interface, the surface profile surrounding the sphere is bent downwards towards the sphere. Therefore, an additional upward capillary force is generated that balances the weight of the sphere together with the buoyancy force. In the present Thesis, we use the word "floater" to refer to a macroscopic sphere driving by not only gravity and Archimedes' buoyancy forces, but also surface tension force.

Whether the meniscus shape around the sphere is convex or concave can be easily determined by equating the sum of the vertical forces to zero [1]. In Section 2.2, we will present this static balance depending on the wetting properties and the density of the sphere relative to the carrier liquid. If one places a second identical sphere at a distance away from the first sphere, they attract each other. In this case, the surface profile for each sphere is not axisymmetric anymore which drives the attraction. (A repulsive interaction is also possible, but only if the floaters have different wetting properties or densities.)

Floater to floater interaction was first modeled by Nicolson for spherical bubbles [2]. There, he assumed that the attractive force on a bubble is only due to the surface profile created by the other bubble, neglecting the interaction of the moving bubble with its own meniscus. This assumption has been utilized by Chan *et al.* [3] to calculate the interaction energy between floating spheres and cylinders. There, the interaction energy has been defined as a multiplication of the surface height and the effective weight of the floater after evaluating the buoyancy and the surface tension. Consequently, the interaction force is simply the spatial gradient of the interaction energy. In this limit, interaction between many spheres is just calculated as the sum of the interactions of pairs of spheres, i.e., a superposition principle is assumed to hold.

Later, Vassileva and co-workers [4, 5] were able to go beyond the two-floater limit, and reported the interaction force for many floaters in an exact form. For a stationary eight-floater aggregate composed of identical small spheres, they showed that the difference between the force of two interacting floaters calculating in the

Nicolson approximation and the force calculated using the exact method is less than 2%. Recently, Dalbe and co-workers [6] considered the attractive interaction of frictional spheres in the viscous limit. They indicated the morphological differences in floater agglomeration by increasing the floater number. Whereas three macroscopic spheres form a compact triangular cluster, a chain-shaped cluster has been observed beyond a certain number of spheres. ‡ In Section 2.2.3, we will provide the capillary force and energy for two spheres considering the superposition principle [3].

In the present thesis, we are not only interested in floating spheres at a static liquid-air interface, but also in spheres floating on a dynamic curved interface, namely floaters on a standing wave. Even though the dynamics of a small sphere in a nonuniform flow had been described [7], the dynamics of a sphere floating on a surface standing wave has not been studied in detail until the pioneering work of Falkovich and co-workers [8–10]. They have shown experimentally and theoretically that, depending on the wetting properties and density of the sphere, the sphere will either drift to an amplitude maximum (antinode) or a minimum (node) of a standing wave. In Section 2.3, we will provide the theory of the dynamics of a sphere floating on a standing wave based on Refs. [8, 10].

2.2 Floaters at a static interface

In the present Section, we will discuss what happens small spheres float on a static flat interface. First, the force balance of a single sphere at a liquid-air interface will be discussed in Section 2.2.1. Subsequently, the attractive capillary energy and force will be examined for two identical spheres in Sections 2.2.2 and 2.2.3, respectively. Finally, in Section 2.2.4, the attractive capillary energy of many identical spheres will be defined.

2.2.1 Static force balance for a single sphere

Here, we will discuss the static force balance introduced in Ref. [1]. When a spherical floater with density ρ_s and contact angle θ is put on an air-liquid interface, the sur-

‡In Chapter 4 of this Thesis, we will examine the morphological properties of the floater agglomeration on a standing Faraday wave. There, we will show that similar to the static system of Ref. [6], compact, circular floater clusters composed of a few floaters evolve into filamentary clusters beyond a certain number of floaters. This morphologic deformation from a compact shape to an elongated structure with increasing the number of floaters may have a common characteristics of floater agglomerations, however, a detailed comparison is beyond the present Thesis.

face of the liquid (with density ρ_l) is deformed to satisfy the vertical force balance. This means that the weight of the sphere, the buoyancy force and the surface tension force (with surface tension coefficient σ) must sum up to zero.

The surface deformation due to a single sphere in a static equilibrium is shown schematically in Fig. 2.1 for four distinct spheres, namely (a) hydrophilic [wetting, i.e., $\theta < \pi/2$] and heavy [$\rho_s > \rho_l$], (b) hydrophobic [non-wetting, i.e., $\theta > \pi/2$] and heavy, (c) hydrophilic and light [$\rho_s < \rho_l$], and finally (d) hydrophobic and light.

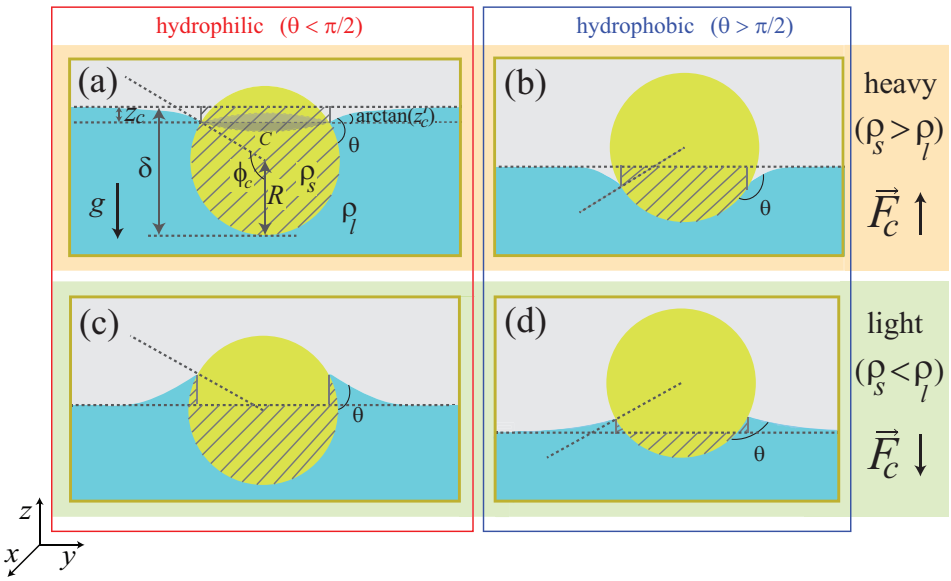

Figure 2.1: A floating sphere trapped at a liquid-air interface in the static case: (a) Hydrophilic heavy sphere, (b) hydrophobic heavy sphere, (c) hydrophilic light sphere, and (d) hydrophobic light sphere. The shaded regions indicate the volume of the liquid displaced by the corresponding sphere as calculated in Ref. [11]. In (d), the total displaced liquid volume is the shaded volume below the dashed line with subtracting the volume of the shaded triangular regions. In (a), the sphere radius R, the contact angle θ, the submerged part δ, the interfacial profile of the surface height far away from the meniscus z_c and the interfacial slope z_c' at the contact point are shown. The line contour of the dark shaded region C, the sphere density ρ_s, the liquid density ρ_l, and the acceleration of the gravity g are also presented. Since the meniscus induced by the sphere is convex in (a, b) and concave in (c, d), the corresponding surface tension $\vec{F}_c$ acts upwards in (a, b) and downwards in (c, d).

As shown in the figures, the meniscus shape around each sphere is different. The meniscus is convex for the situations described in Figs. 2.1(a, b) so that the resultant surface tension force $\vec{F}_c$ acts upwards. On the other hand, in Figs. 2.1(c, d), the meniscus is concave and therefore $\vec{F}_c$ acts downwards.

$\vec{F}_c$ is a line force and can be calculated by integrating the line contour of the shaded region C described in Fig. 2.1(a). The expression of $\vec{F}_c$ can then be given as

$$\vec{F}_c = \sigma \int_C ds \, \sin\phi_c \, \hat{\mathbf{r}} \times \hat{\mathbf{n}}, \tag{2.1}$$

where $\hat{\mathbf{r}}$ is the unit vector pointing radially out of C and $\hat{\mathbf{n}}$ is the unit vector pointing out of the liquid. Here, s is the arc length of C and ϕ_c is the angle described in Fig. 2.1(a). Due to axisymmetry, the line integral along C yields $2\pi R$, where R is the radius of the sphere. Thus,

$$\vec{F}_c = \sigma \, 2\pi R \, \sin\phi_c \, \sin(\arctan z_c') \, \hat{\mathbf{z}}. \tag{2.2}$$

Here, z_c' is the interfacial slope at the contact point as illustrated in Fig. 2.1(a).

We now calculate the buoyancy force F_b, which is upwards for all cases. In Archimedes' law, $F_b = m_d g$, where m_d is the liquid mass displaced by an object and g is the acceleration of the gravity. However, for a sphere with a certain meniscus around it, defining m_d is not trivial. The rigorous derivation of m_d in this case has been given by Keller [11], by integrating the force due to the hydrostatic pressure on the wetted part of the sphere. However, in this Section, we will only give the results without considering detailed calculations.

In Archimedes' buoyancy where the deformation of the liquid at the contact line is assumed to be negligible, all the wetted part of a sphere is evaluated to determine m_d. However, in the presence of the meniscus, a certain region should be either added or removed depending on the shape of the meniscus, i.e., the sign of $\vec{F}_c$. If the meniscus is convex (positive $\vec{F}_c$), the liquid mass which fills the volume trapped between the contact point where the liquid touches the sphere and the liquid level far away is added to m_d. On the other hand, if the meniscus is concave (negative $\vec{F}_c$), the liquid mass which fills the trapped volume is removed. Therefore, F_b is the liquid mass which fills the total shaded region described in Figs. 2.1(a-d). Exceptionally, in Fig. 2.1(d), two small triangular regions are removed from the below shaded region to determine the total volume displaced by the liquid. Therefore, F_b for the configuration illustrated in Fig. 2.1(a) is equal to

$$F_b = m_d \, g = \rho \, \pi R^3 \left(\frac{2}{3} - \cos\phi_c + \frac{\cos^3\phi_c}{3} + \frac{\sin^2\phi_c}{R} \, z_c \right) g. \tag{2.3}$$

Here, the total volume is calculated by summing the volume of a circular cylinder of radius $R\sin\phi_c$ and height z_c, and the volume of the submerged part of the sphere.

We can now equate the sum of all vertical forces to zero to satisfy the static force balance, i.e., $\vec{W} + F_b\hat{\mathbf{z}} + \vec{F}_c = 0$. Here, the weight of the sphere $\vec{W} = -\frac{4}{3}\pi R^3\rho_s\hat{\mathbf{z}}$. Considering Fig. 2.1(a) where $\vec{F}_c$ is positive, the balance is

$$F_b + F_c = \frac{4}{3}\pi R^3\rho_s g. \tag{2.4}$$

Using Eq. 2.2 and Eq. 2.3 in the above equation gives

$$\rho_l\,\pi R^3\left(\frac{2}{3} - \cos\phi_c + \frac{\cos^3\phi_c}{3} + \frac{\sin^2\phi_c}{R}\,z_c\right)g + \sigma\,2\pi R\,\sin\phi_c\,\sin(\arctan z_c') = \frac{4}{3}\pi R^3\rho_s g. \tag{2.5}$$

If terms of second and higher order in z_c' are neglected, $\sin(\arctan z_c') \approx z_c'$. This is a valid approximation if one assumes a small curvature. Geometrically, $\phi_c = \pi - \theta - \arctan(z_c')$. Considering again only terms linear in z_c', goniometric relations give $\sin\phi_c \approx \sin\theta - \cos\theta z_c'$ and $\cos\phi_c \approx -\cos\theta - \sin\theta z_c'$. Inserting these into Eq. 2.5 and making some rearrangements in the terms give [1]

$$z_c'\sin\phi_c = B\left[\frac{2D-1}{3} - \frac{1}{2}\cos\theta + \frac{\cos^3\theta}{6} + \mathcal{O}(B)\right]. \tag{2.6}$$

Here, the Bond number, $B = \rho_l g R^2/\sigma$, is one of the most important dimensionless parameters in the system. Since B gives the ratio of gravity versus surface tension, it determines the meniscus. Furthermore, $D = \rho_s/\rho_l$, and $\mathcal{O}(B)$ includes the higher order terms with respect to B starting with B^2.

It is straightforward to show that the above calculation also holds for the other cases of Fig. 2.1. Here, the sign of the curvature gives the direction of the capillary force $\vec{F}_c$. In the left hand side of Eq. 2.6, since $\phi_c < \pi$, i.e., $\sin\phi_c > 0$, the sign of z_c' can be determined by the sign of the right hand side of the equation. For small spheres, $B \ll 1$, only the linear term needs to be evaluated[§] such that [1]

$$\boxed{z_c'\sin\phi_c \approx B\left[\frac{2D-1}{3} - \frac{1}{2}\cos\theta + \frac{\cos^3\theta}{6}\right] \equiv B\Sigma(\theta, D).} \tag{2.7}$$

In conclusion, the direction of $\vec{F}_c$ is determined by the sign of the curvature z_c', which in turn is provided by that of $B\Sigma(\theta, D)$ (Eq. 2.7).

[§]In the present Thesis, the maximum $B = 0.02$. Since the nonlinear terms in Eq. 2.6 starts with B^2, the expected percentage error is around 0.02% for a single sphere. For many spheres, Eq. 2.6 cannot be employed since the approximation $\sin(\arctan z_c') \approx z_c'$ is not valid anymore due to larger curvature z_c' compared to the single sphere case.

In Fig. 2.2(a), the sign of the curvature, i.e., $B\Sigma(\theta, D)$, is shown for several hydrophilic ($\theta < \pi/2$) and hydrophobic ($\theta > \pi/2$) spheres being both lighter ($\rho_s < \rho_l$) and heavier ($\rho_s > \rho_l$) than the carrier liquid. $B\Sigma(\theta, D) > 0$[¶] represents the situation that the resultant surface tension $\vec{F}_c$ acts upwards, whereas $B\Sigma(\theta, D) < 0$ represents the case that $\vec{F}_c$ acts downwards. This plot indicates that common understanding, i.e., $\vec{F}_c$ acting upwards for hydrophobic spheres and downwards for hydrophilic spheres, oversimplifies the situation. The reason behind this is the fact that is the relative density $D = \rho_s/\rho_l$ brings additional complexity: $B\Sigma(\theta, D)$ contains both the contact angle of the sphere θ and the relative density D. Therefore, the four cases of a sphere at a static liquid-air interface presented in Fig.2.1(a-d) are theoretically understood.

The last issue we will discuss here is how to determine the depth of the submerged part δ. As shown in Fig. 2.1(a), $\delta = R[1 - \cos\phi_c]$. When the approximated $\cos\phi_c$ defined above [Eq. 2.6] is used, we find with the help of Eq. 2.7,

$$\boxed{\delta \approx R[1 + \cos\theta + B\Sigma(\theta, D)].} \tag{2.8}$$

In Fig. 2.2(b), the corresponding δ is presented. The fact that for all presented curves $\delta/2R$ is smaller than 1 indicates that not only heavy hydrophobic spheres but also heavy hydrophilic spheres can float, which is less-known.

[¶]Of course, these sign conditions are on $\Sigma(\theta, D)$ only since B is always positive. The reason why we keep this multiplication [i.e., $B\Sigma(\theta, D)$] is to preserve its physical meaning.

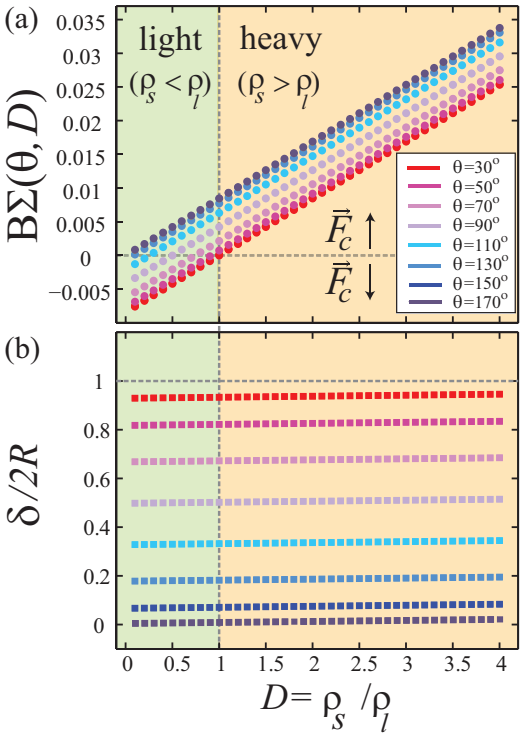

Figure 2.2: (a) $B\Sigma(\theta D)$, which determines the sign of the curvature induced by a single floating sphere, for various contact angle θ and sphere density ρ_s combinations as a function of $D = \rho_s/\rho_l$. (b) The corresponding normalized submerged part of the sphere $\delta/2R$ also as a function of D. It is smaller than 1 for even $D > 1$ indicating that both heavy hydrophobic and heavy hydrophilic spheres can float on that carrier liquid with density ρ_l. For both graphs, the sphere radius R and ρ_l are fixed to $R = 0.31$ mm and $\rho_l = 998$ kg/m^3, respectively. $B = 0.0091$ and $\sigma = 72.8 \cdot 10^{-3}$ N/m. The green regions are for light spheres, i.e., $\rho_s < \rho_l$, whereas the orange regions are for heavy spheres, i.e., $\rho_s > \rho_l$. θ increases from the most hydrophilic case (red) to the most hydrophobic one (blue). The small difference in $\delta/2R$ for increasing D reflects that the curves presented here are for small spheres ($B \ll 1$). In addition, beyond a certain D, the results presented here may not be valid since the curvature would not be small enough to satisfy the linear approximations used in Eq. 2.5. Consequently, taking the leading order of B [see Eq. 2.7] may be insufficient.

Determining the contact angle of a floating sphere

Usually, contact angles are measured by a goniometer, where a sessile drop is placed on a surface, and then the angle between the drop and the surface is determined. However, this method gives inaccurate results for small substrates and curved surfaces. In our case, since we are dealing with small spheres, the contact angle at the position where the sphere touches the drop is hard to measure accurately.

We therefore calculate the contact angle of a polystyrene sphere[‖] with radius $R = 0.26$ mm floating at a liquid-air interface by considered the *static balance* discussed earlier. As shown in Fig. 2.3, the weight of the sphere, Mg, is larger than the buoyancy force, $m_d\, g$, so that the surface tension force acts upwards. The fact that the contact angle θ is smaller than 90° indicates that the floater is hydrophilic. The interface cannot be photographed well enough to accurately determine θ by image analysis. To determine θ nevertheless, we measure δ and calculate θ using Eq. 2.8, derived in the previous Subsection.

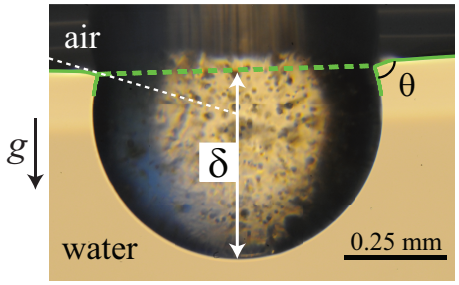

Figure 2.3: A polystyrene sphere floating at an air-water interface in a static equilibrium is imaged from the side. The solid green line represents the interface. The green dashed line displays the circular contact line around the floater. The white dashed line indicates the surface normal of the contact line. The contact angle θ and the depth of the submerged part δ are shown when the floater is at the vertical force balance: The surface tension acts upwards to satisfy the balance since $M > m_d$.

In our case, $B = 0.0091$ and the calculation gives $\boxed{\theta \approx 74.3^\circ}$ when the physical constants of air and water are taken to be the standard literature values assuming a temperature of 20 °C.

[‖] The sphere is cleaned by applying the cleaning protocol given in Ref. [12], which consists of rinsing the sphere with isopropanol. Then, the sphere is dried, and further heated to remove all the chemicals. Since the sphere is hydrophilic polystyrene, the suggested heating temperature is 70 °C at most. We heated the sphere at 65 °C for 1 hour. Finally, the sphere is left to cool to ambient temperature.

2.2.2 Capillary energy of two identical spheres

The behavior of a single floater at a static liquid-air interface has been discussed above. When a second identical sphere is placed at the interface at some position far away from the first sphere, the two spheres mutually attract and move towards each other until they touch. Intuitively, one can understand that coming together should be energetically more favorable than being apart: The surface deformation of two spheres that touch is less than the surface deformation of two isolated spheres. Therefore, the total potential energy including both gravity and surface tension should become smaller when the distance between the spheres becomes shorter.

Here, we will give the definition of the capillary energy of two identical spheres by considering the Nicolson superposition principle [2] first utilized by Chan *et al.* [3]. As a reminder, in the superposition principle, the sphere is attracted by the surface profile created by the other sphere without taking the interaction with its own surface deformation into account. Therefore, the potential energy can be found as the product of the vertical displacement of the sphere, determined by the meniscus of the other sphere, and the reduced weight of the sphere which is the resultant of the buoyancy and the surface tension.

The reduced weight can be approximated by the static case discussed in the previous Subsection, where we found that $\vec{F}_c = (W - F_b)\hat{\mathbf{z}}$. Considering Eq. 2.2 with the assumption that $\sin(\arctan z_c') \approx z_c'$, we have

$$\vec{F}_c = \sigma\, 2\pi R\, \sin\phi_c\, z_c'\, \hat{\mathbf{z}}. \tag{2.9}$$

Here, $\sin\phi_c\, z_c'$ can be approximated as $B\Sigma(\theta, D)$ [Eq. 2.7]. Therefore,

$$\boxed{\vec{F}_c = \sigma\, 2\pi R\, B\Sigma(\theta, D),} \tag{2.10}$$

which is called the reduced weight of the sphere [1]. Furthermore, for small spheres, i.e., $B \ll 1$, the surface height $z(r)$ deformed by a single sphere at a distance r is given as [3] **

$$z(r) = -L_c z_c' \frac{K_0(r/L_c)}{K_1(R\sin\phi_c/L_c)}, \tag{2.11}$$

where the capillary length $L_c = \sqrt{\sigma/\rho_l g}$, K_0 and K_1 are the zeroth and the first order of the Bessel functions of the second kind, respectively.

**The Young-Laplace equation $\sigma\Delta z(r) = \rho_l g z(r)$ is solved to determine $z(r)$ [3]. Here, Δ is the Laplacian, which in axisymmetric cylindrical form equals $\Delta = \frac{d^2}{dr^2} + \frac{1}{r}\frac{d}{dr}$. Therefore, the solutions are Bessel functions.

For small spheres, $R\sin\phi_c \ll L_c$ so that $K_1(R\sin\phi_c/L_c) \approx L_c/R\sin\phi_c$ [1]. Thus, $z(r)$ becomes

$$\boxed{z(r) = -z_c' R\sin\phi_c K_0(r/L_c) = -RB\Sigma K_0(r/L_c).} \tag{2.12}$$

We now finally calculate the gravity-induced capillary potential energy $E_c(r)$ by multiplying the reduced weight of a single sphere , i.e., $\vec{F}_c$ [Eq. 2.10], and the height difference induced by the other sphere $z(r)$ [Eq. 2.12], leading to [1, 3]

$$\boxed{E_c(r) = -\sigma\, 2\pi R^2\, B^2\, \Sigma^2(\theta, D)\, K_0(r/L_c).} \tag{2.13}$$

2.2.3 Capillary force of two identical spheres

The gravity-induced capillary force can be determined by [1, 3]

$$\boxed{\vec{F}_c(r) = -\frac{dE(r)}{dr} = -\sigma\, 2\pi R\, B^{5/2}\, \Sigma^2(\theta, D)\, K_1(r/L_c).} \tag{2.14}$$

Here, the direction of $\vec{F}_c(r)$ indicates that the force is always attractive for two identical spheres.

By performing a simple experiment, we can check how well Eq. 2.14 works for two small spheres. We put two polystyrene spheres with a radius 0.35 mm on pure water at around 6 particle distances away from each other. The measured distance between the spheres $r(t)$ is shown as a function of time in Fig. 2.4 by the green line.

To check the agreement between our measurement and the theory given in Eq. 2.14, we consider the force balance between the capillary force, given in Eq. 2.14, and the viscous drag force. This is reasonable if one realizes that for a small sphere which is largely submerged in the liquid, the drag term in the equation of motion is much larger than the acceleration term [1]. Therefore, for small spheres ($B \ll 1$) the balance between the Stokes drag and the capillary interaction yields [1][††].

$$3\pi\mu\, R\, \alpha \frac{dr}{dt} = -\sigma\, 2\pi R\, B^{5/2}\, \Sigma^2(\theta, D)\, K_1(r(t)/L_c), \tag{2.15}$$

where μ is the dynamic viscosity of the carrier liquid, which is water in the present case, and $\alpha \approx \delta/R$. This factor takes into account that only part of the particle is submerged and subject to drag. Furthermore, we consider the asymptotic form of

[††]In Ref. [1], the factor 6 is used instead of 3 in the Stokes drag term, but it should be 3. The reason is as follows: The equation for the one sphere is $6\pi\mu R\alpha \frac{d\vec{r}_1}{dt} = \vec{F}_c(|\vec{r}_1 - \vec{r}_2|)$ and the equation for the second sphere is $6\pi\mu R\alpha \frac{d\vec{r}_2}{dt} = -\vec{F}_c(|\vec{r}_1 - \vec{r}_2|)$. When the first equation is subtracted by the second one, we have $6\pi\mu R\alpha \frac{d(\vec{r}_1 - \vec{r}_2)}{dt} = 2\vec{F}_c(|\vec{r}_1 - \vec{r}_2|)$. Consequently, $3\pi\mu R\alpha \frac{d\vec{r}}{dt} = \vec{F}_c(r)$.

$K_1(r(t)/L_c) \approx L_c/r(t)$. This can be valid when $r(t) \ll L_c$ (which may not be satisfied for all t in our case since $L_c = 2.7$ mm in a water-air interface at 20°C). Then, with $L_c = R/B^{1/2}$, Eq. 2.17 becomes

$$r(t)\,dr = -\frac{2}{3}\frac{\sigma}{\mu} R^2\, B^2\, \frac{\Sigma^2(\theta, D)}{\delta(\theta)}\, dt. \tag{2.16}$$

Here, using the contact angle θ as a fitting parameter, which is readily integrated to

$$r(t) = \sqrt{r(0)^2 - \frac{4}{3}\frac{\sigma}{\mu} R^2\, B^2\, \frac{\Sigma^2(\theta, D)}{\delta(\theta)}\, t}. \tag{2.17}$$

The resultant $r(t)$ is presented in Fig. 2.4 by the brown line.

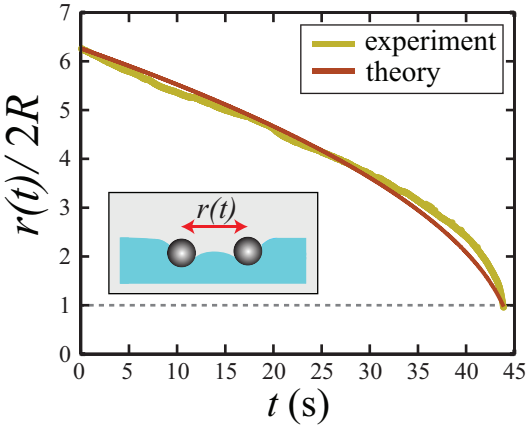

Figure 2.4: The distance between two identical spheres, floating at a static water-air interface, with radius R=0.35 mm and $B = 0.0164$ as a function of time. The green line presents the experimental measurement and the brown line is the result of the theory, equating the capillary force with the viscous drag force. The measured $r(t)$ and the theoretical one both agree with each other quite well when $\theta \approx 75.1°$. (Inset) The surface deformation due to the presence of two floating spheres at a liquid-air interface. Since an asymmetry in the meniscus is generated around each sphere, the spheres experience an attractive interaction.

We find that $\theta \approx 75.1°$ gives the best agreement between the measured and the estimated curves. This is very close to the result determined from the static balance, $\theta \approx 74.3°$ [see Fig. 2.3]. The small discrepancy may be explained from the fact that the polystyrene spheres have a slightly different R due to the polydispersity of the particle sample we use.

2.2.4 Capillary energy of many identical spheres

In the linear approximation, the capillary energy of many identical spheres can be obtained by summing the contributions of each particle pair in the system such that

$$E_c^T = \sum_{\substack{i=1 \\ i \neq j}}^{N} \sum_{j=1}^{N} E_c(\mid \vec{r}_i - \vec{r}_j \mid). \tag{2.18}$$

Here, E_c^T is the total capillary energy summing over all N particles. $E_c(\mid \vec{r}_i - \vec{r}_j \mid)$ is the capillary energy [Eq. 2.13] of each pair of particles i and j, where $\mid \vec{r}_i - \vec{r}_j \mid$ is the distance between i and j. We will use this definition in Chapter 3.

2.3 A floater on a standing wave

In previous Section, we have discussed a single floater in a static equilibrium and floater-to-floater interaction for two identical spheres in an approximate limit. In this Section, we will describe the dynamics of a single sphere floating on a standing wave, as was already studied by Falkovich and co-workers both experimentally and theoretically [8–10], with some new suggestions and further extensions. Falkovich and co-workers reported that, on a standing surface wave, the sphere does not simply oscillate, but in addition drifts[‡‡] either towards the wave amplitude maxima (antinodes) or the amplitude minima (nodes), depending on the wetting property and the density of the sphere. The direction of the surface tension $\vec{F}_c$, and so the sign of the curvature $B\Sigma(\theta, D)$ [see Fig. 2.2(a)] determines the direction of the drift.

In Refs. [8–10], it has been explained that if $\vec{F}_c > 0$ the sphere drifts to the antinodes, otherwise, if $\vec{F}_c < 0$ the sphere drifts to the nodes. The authors of Refs. [8–10] have simplified this rule by stating that a heavy and hydrophobic sphere drifts to the antinodes, whereas a light and hydrophilic sphere drifts to the nodes. However, there is a subtlety here, which becomes clear if one looks at Fig. 2.2. If the physical parameters of the sphere, i.e., ρ_s and θ, satisfy $B\Sigma(\theta, D) > 0$ [i.e., $\Sigma(\theta, D) > 0$], the drift is towards the antinodes, otherwise, if both satisfy $B\Sigma(\theta, D) < 0$ [i.e, $\Sigma(\theta, D) < 0$], the drift is towards the nodes. This means that not only hydrophobic but also hydrophilic floating particles will move to the antinodes, as long as their density is larger than that of water. Vice versa, floating particles that are lighter than water will always move to the nodes, regardless of their wetting properties. The drift mechanism is sketched in Fig. 2.5.

2.3.1 Drift force

A small sphere floating on a surface standing wave drifts when it experiences a finite surface tension. The drift, considered in the present thesis, is a horizontal motion of a rigid sphere on a standing wave surface relative to a fluid particle oscillating on the surface. As illustrated in Fig. 2.5, the direction of the drift depends on the wetting property of the sphere θ and its density relative to the carrier liquid $D = \rho_s/\rho_l$. We now discuss the derivation of the drift force in more detail following the line of

[‡‡]The drift mentioned in the present thesis is observed for a particle floating on a surface standing wave. Therefore, although it is reminiscent of the Stokes drift, which is generated by a traveling wave, it is also different. For Stokes' drift, the fluid particle Lagrangian velocity on a traveling wave surface deviates from the Eulerian velocity so that the particle drifts [13]. The present phenomenon bears much more similarity to a periodic rolling over an oscillating plate [14, 15]

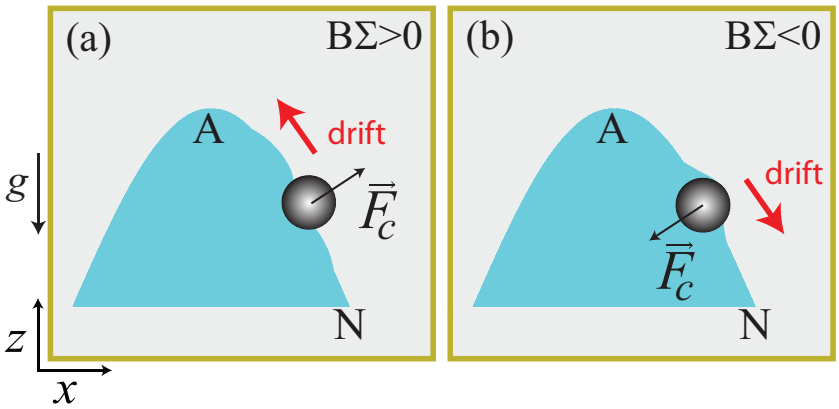

Figure 2.5: Single sphere drift due to a standing wave. (a) The drift is towards the antinode (A) when the sphere experiences upward surface tension [$\vec{F}_c > 0$]. This occurs if the meniscus around the sphere is bent upwards [$B\Sigma > 0$]. (b) The drift is towards the nodes (N) when the opposite situation is created such that $\vec{F}_c < 0$, e.g. $B\Sigma < 0$.

reasoning in Ref. [10], both to convince the reader of the phenomenon described in Fig. 2.5 and because we will use the expression derived below in the present and the next Chapters of this Thesis.

The horizontal motion of a small rigid sphere on a one dimensional surface standing wave has been described by Maxey and Riley [7]. Following [10] we add a surface tension term which gives

$$M\frac{dV}{dt} = m_d(\delta)\frac{Du}{Dt} + m_{ad}\frac{d}{dt}(u-V) + M\gamma_h(u-V) + F_c(\delta)\frac{\partial\zeta}{\partial x}. \tag{2.19}$$

Here, the mass terms M, m_d, and m_{ad} are for that of the sphere, the displaced liquid, and the added mass, respectively. (The Basset history force, evaluating the delay in the boundary layer due to viscous effects, presented in Ref. [7] is neglected.) In addition, V is the horizontal component of the sphere velocity and u the fluid particle horizontal velocity at the surface $u = u_0 \sin\omega t \cos kx$, where ω is the angular wave frequency and k is the wave number (the subscript in ω_k is dropped for notational convenience).

The Stokes drag coefficient γ_h can be approximated as $6\pi\mu R\alpha/M$ with liquid dynamic viscosity μ and $\alpha \approx \delta/R$ as defined in Section 2.2.3). The capillary force F_c has been multiplied with the sine of the local inclination angle of the wave, which for

small wave amplitudes can be approximated as the derivative $\partial\zeta/\partial x$ of the surface wave elevation $\zeta = -(u_0/\omega)\cos\omega t \sin kx$. Finally, the material derivatives are defined as follows [7]

$$\begin{aligned} \left.\frac{Du}{Dt}\right|_{x=X(t)} &= \left.\left(\frac{\partial u}{\partial t} + u\frac{\partial u}{\partial x}\right)\right|_{x=X(t)}, \\ \left.\frac{du}{dt}\right|_{x=X(t)} &= \left.\left(\frac{\partial u}{\partial t} + V\frac{\partial u}{\partial x}\right)\right|_{x=X(t)}, \end{aligned} \tag{2.20}$$

where $X(t)$ is the horizontal position of the sphere. One can neglect the higher order terms with respect to u_0 for small wave amplitudes. Consequently, the convective terms in Eq. 2.20 are approximately to zero such that

$$\begin{aligned} \left.\frac{Du}{Dt}\right|_{x=X(t)} &\approx \left.\frac{\partial u}{\partial t}\right|_{x=X(t)}, \\ \left.\frac{du}{dt}\right|_{x=X(t)} &\approx \left.\frac{\partial u}{\partial t}\right|_{x=X(t)}. \end{aligned} \tag{2.21}$$

Since $dV/dt = \partial V/\partial t$, all time derivatives now become partial time derivatives $\partial/\partial t$.

To determine the horizontal acceleration of the sphere relative to the acceleration of the fluid particle, we rearrange Eq. 2.19 such that the terms including V are moved to the left side, also considering the assumptions in Eq. 2.21

$$M\frac{\partial V}{\partial t} + M\gamma_h(V-u) + m_{ad}\frac{\partial}{\partial t}(V-u) = m_d(\delta)\frac{\partial u}{\partial t} + F_c(\delta)\frac{\partial \zeta}{\partial x}. \tag{2.22}$$

By subtracting $M\frac{\partial u}{\partial t}$ from both sides, we have

$$(M+m_{ad})\left(\frac{\partial V}{\partial t} - \frac{\partial u}{\partial t}\right) + \gamma_h(V-u) = m_d(\delta)\frac{\partial u}{\partial t} - M\frac{\partial u}{\partial t} + F_c(\delta)\frac{\partial \zeta}{\partial x}. \tag{2.23}$$

If we now abbreviate the right hand side of Eq. 2.23 as $f(x(t),t)$ and reverse the equation we have

$$f(x(t),t) = (M+m_{ad})\left(\frac{\partial V}{\partial t} - \frac{\partial u}{\partial t}\right) + \gamma_h(V-u). \tag{2.24}$$

Averaging both sides over a single wave period T yields

$$f(x) \equiv \frac{1}{T}\int_0^T f(x(t),t)\,dt = \frac{1}{T}\int_0^T \left[(M+m_{ad})\left(\frac{\partial V}{\partial t} - \frac{\partial u}{\partial t}\right) + \gamma_h(V-u)\right] dt. \tag{2.25}$$

First evaluating the right hand side of Eq. 2.25 we note that contributions coming from the wave gives zero

$$\frac{1}{T}\int_0^T u(x,t)\,dt = \frac{1}{T}\int_0^T u_0 \sin\omega t \cos kx\,dt = 0, \tag{2.26}$$
$$\frac{1}{T}\int_0^T \frac{\partial u}{\partial t}\,dt = \frac{1}{T}\int_0^T u_0\omega \cos\omega t \cos kx\,dt = 0,$$

with which Eq. 2.25 now becomes

$$f(x) = (M+m_{ad})\left[\frac{V(T)-V(0)}{T}\right] + \gamma_h\left[\frac{X(T)-X(0)}{T}\right], \tag{2.27}$$

where we still need to calculate $f(x)$. Before we do so, we first note that the right hand side of this equation represents mass times acceleration and drag force on the sphere on time scales much larger than the period T of the standing wave.*

To determine $f(x)$, let us turn back to Eq. 2.23. Averaging the right side of the equation over a single wave period T gives

$$f(x) = \frac{1}{T}\int_0^T \left[m_d\frac{\partial u}{\partial t} - M\frac{\partial u}{\partial t} + F_c(\delta)\frac{\partial \zeta}{\partial x}\right] dt, \tag{2.28}$$

where there is no contribution from the first two terms due to Eq. 2.26. This implies that

$$f(x) = \frac{1}{T}\int_0^T F_c(\delta)\frac{\partial \zeta}{\partial x}\,dt. \tag{2.29}$$

In Ref. [8, 10], $F_c(\delta)$ is calculated by solving the vertical equation of motion of the submerged part of the sphere δ

$$M\left(\frac{\partial^2\delta}{\partial t^2} + \gamma_v\frac{\partial\delta}{\partial t}\right) = [M - m_d(\delta)]\left(g + \frac{\partial^2\zeta}{\partial t^2}\right) + F_c(\delta), \tag{2.30}$$

where γ_v is the vertical friction coefficient. Subsequently, one assumes that the time-dependence of δ is small such that $\delta(t)$ can be set to its equilibrium value δ_0, and $\partial^2\delta/\partial t^2 = \partial\delta/\partial t = 0$ in Eq. 2.30 which leads to

$$F_c(\delta) \approx F_c(\delta_0) = -[M - m_d(\delta_0)]\left(g + \frac{\partial^2\zeta}{\partial t^2}\right). \tag{2.31}$$

*In Ref. [8, 10], the dispersion relation for gravity waves is used explicitly, whereas the derivation provided here is independent of the choice of dispersion relation.

Inserting this result into Eq. 2.29 and again approximating $\delta(t) \approx \delta_0$ we obtain

$$f(x) = -\frac{1}{T}\int_0^T \left[[M - m_d(\delta_0)]\left(g + \frac{\partial^2\zeta}{\partial t^2}\right)\frac{\partial\zeta}{\partial x}\right] dt, \tag{2.32}$$

where $\partial^2\zeta/\partial t^2 = u_0\omega\cos\omega t\sin kx$ and $\partial\zeta/\partial x = -ku_0/\omega\cos\omega t\cos kx$. Consequently, the time integration gives

$$\boxed{\vec{f}(x) = [M - m_d(\delta_0)]\frac{u_0^2 k}{4}\sin 2kx\,\hat{\mathbf{x}},} \tag{2.33}$$

which is the drift force. In this result, the direction of the time averaged drift depends on the sign of $[M - m_d(\delta)]$: If the value is positive the drift is towards the antinodes, otherwise, the drift is towards the nodes. This mass difference can be positive for a floating sphere only if $\vec{F}_c > 0$, i.e., $B\Sigma(\theta, D) > 0$, and vice versa for the negative mass difference. Thus, the phenomenon described in Fig. 2.5 is proven, and it is good to stress that it describes *time averaged situation*.

Falkovich *et al.* derive their average displacement for the static case from the vertical equation of motion (Eq. 2.30) where they set $\delta = \delta_0$, $\partial^2\delta/\partial t^2 = \partial\delta/\partial t = 0$. We have a better alternative, namely Eq. 2.8. Let us consider these two situations in detail. In Eq. 2.33, m_d can be approximated as $m_{d_{\text{approx}}}(\delta_0) \approx \pi\rho_l(R\delta_0^2 - \delta_0^3/3)$ if $\delta_0 < R$ (which is the liquid mass filling the submerged spherical cap with radius $R\cos\phi_c$ and height δ_0). When $\delta_0 > R$, m_d is similarly approximated to the liquid mass filling the remaining volume of the sphere subtracting the cap so that $m_{d_{\text{approx}}}(\delta_0) \approx \rho_l\left[\frac{4}{3}\pi R^3 - \pi(R\delta_0^2 - \delta_0^3/3)\right]$. We now improve this further using our knowledge of the *static balance* that has been discussed in Section 2.2.1. So, applying Eq. 2.3 with $\cos\phi_c \approx -\cos\theta - \sin\theta z_c'$ and neglecting higher order terms with respect to B, m_d can be written as

$$m_d(B,\Sigma) = \rho_l\pi R^3\left[\frac{2}{3} + \cos\theta - \cos^3\theta + (1 - 3\cos^2\theta)B\Sigma(\theta, D)\right]. \tag{2.34}$$

We have realized that $\vec{f}(x)$ with this more accurate m_d gives qualitatively similar, but quantitatively different results in some limits relative to $\vec{f}(x)$ using the approximated m_d. Before discussing the differences, we will redefine Eq. 2.33 as

$$\boxed{\vec{f}_{\text{approx}}(x) = [M - m_{d_{\text{approx}}}(\delta_0)]\frac{u_0^2 k}{4}\sin 2kx\,\hat{\mathbf{x}}, \text{ and}} \tag{2.35}$$

$$\boxed{\vec{f}^*(x) = [M - m_d(B,\Sigma)]\frac{u_0^2 k}{4}\sin 2kx\,\hat{\mathbf{x}}.} \tag{2.36}$$

To summarize, $\vec{f}_{\text{approx}}(x)$ is the drift force that has been used in the literature [8, 10] up to now. It has the disadvantage that the static balance is less accurate then it could be. Therefore, $\vec{f}^*(x)$, which contains the correct static balance, is the drift force considered in the present Thesis.

Let us compare $\vec{f}_{\text{approx}}(x)$ and $\vec{f}^*(x)$. To perform this efficiently, several combinations of the contact angle of sphere θ and the relative density $D = \rho_s/\rho_l$ are checked. In Fig. 2.6, we show that although all plots are qualitatively similar, they are quantitatively different.

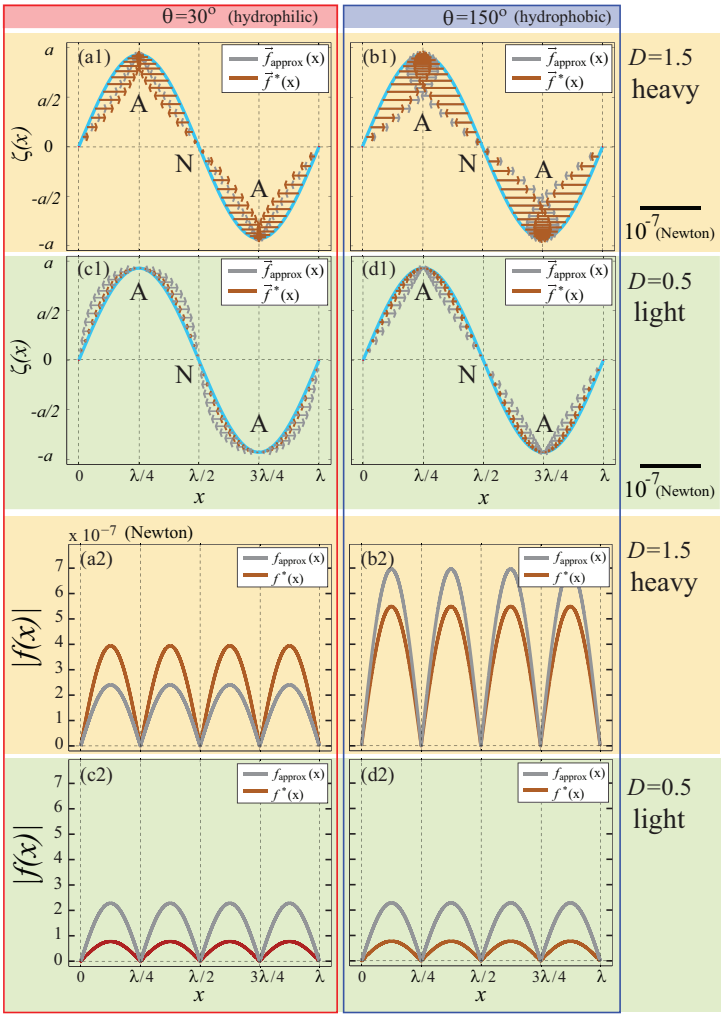

Figure 2.6: Approximate and corrected drift forces, $\vec{f}_{\text{approx}}(x)$ [gray arrows] and $\vec{f}^{*}(x)$ [brown arrows], on a one dimensional standing wave with elevation $\zeta(x)$ [blue lines] for different values of the contact angle θ and the relative density $D = \rho_s/\rho_l$. λ and a are the wavelength and the wave amplitude, respectively. (a1)-(d1) are for the corresponding spheres sketched in Fig. 2.1(a1-d1), respectively. For all cases, the corresponding forces qualitatively give the same results, i.e., drifting towards the antinodes [A] in (a,b,d) and drifting towards the nodes [N] in (c). [These are expected results if one checks Fig. 2.5 with Fig. 2.2(a).] However, they are quantitatively different for all cases. Remarkably, the difference in the magnitudes of the forces when $D = 0.5$ suggests that $\vec{f}_{\text{approx}}(x)$ is less accurate for smaller curvatures. Furthermore, both forces are larger when $D = 1.5$ states that the sharper the meniscus is created by the sphere, the larger the drift is observed. [The bar indicates a force scale of 10^{-7} Newton.] Below panel (a2-d2): The magnitude of the corresponding approximated $f_{\text{approx}}(x)$ [gray lines] and corrected $f^{*}(x)$ [brown lines] drift forces are shown. The differences in the magnitude are clearly presented.

Consequently, θ and D are important to determine both the direction and the magnitude of the drift force. One can also realize the importance of x, the position of the sphere, on the magnitude of drift. In Fig. 2.6, we observe that for all cases the magnitude of the drift is maximum when x is between A [antinodes] and N [nodes], and decreases while x is towards either A or N. Furthermore, it is zero when x is at A or N. Therefore, the sphere being initially placed either at A or at N experiences no drift, however, if the sphere is initially at $(2n+1)\lambda/8$ with an integer n and the wavelength λ, it drifts most strongly.

2D generalization of the drift force and the corresponding drift energy

The derivation of the drift force $\vec{f}(x)$ has been presented for the one-dimensional case, and we now extend this to a rectangular two-dimensional standing wave, i.e., $\vec{f}(x,y)$. So, Eq. 2.32 with the corrected displaced mass $m_d(B,\Sigma)$ can be written in $2D$ as

$$\vec{f}(x,y) = -\frac{1}{T}\int_0^T [M - m_d(B,\Sigma)]\left(g + \frac{\partial^2\zeta}{\partial t^2}\right)\left(\frac{\partial\zeta}{\partial x}\,\widehat{\mathbf{x}} + \frac{d\zeta}{dy}\,\widehat{\mathbf{y}}\right) dt, \tag{2.37}$$

Here, ζ is the surface wave elevation, and so $\partial^2\zeta/\partial t^2$ is the surface wave acceleration in z-direction. (We will continue using $m_d(B,\Sigma)$ in $\vec{f}(x,y;t)$. However, the asterisk * introduced in Eq. 2.36 is dropped for convenience.)

In 2D, $\zeta(x,y;t)$ is maximum at the antinodes [when both x and y positions are equal to $(2n+1)\lambda/4$ with integer n] and minimum at the nodes, when both x and y positions are equal to $(n+1)\lambda/2$. Therefore,

$$\begin{aligned} \zeta &= -\frac{u_0}{\omega_{k_xk_y}}\cos\omega_{k_xk_y}t\,\sin k_x x\,\sin k_y y, \\ \frac{\partial^2\zeta}{\partial t^2} &= -u_0\omega_{k_xk_y}\cos\omega_{k_x\,k_y}t\,\sin k_x x\,\sin k_y y, \end{aligned} \tag{2.38}$$

where k_x and k_y are the corresponding wave numbers of x and y, respectively.

By inserting expressions given in Eq. 2.38 into Eq. 2.37, the 2D drift force is

$$\begin{aligned} \vec{f}(x,y) &= \frac{M - m_d(B,\Sigma)}{4}\,u_0^2\,\times \\ &\quad -\frac{1}{T}\int_0^T \left(\left[k_x \sin 2k_x x\,(1-\cos 2k_y y)\,\widehat{\mathbf{x}} + k_y\,\sin 2k_y y\,(1-\cos 2k_x x)\,\widehat{\mathbf{y}}\right]\cos^2\omega t\right) dt. \end{aligned} \tag{2.39}$$

After carrying out the integration over time we obtain

$$\vec{f}(x,y) = \frac{M-m_d(B,\Sigma)}{8}u_0^2 \times \left[k_x \sin 2k_x x(1-\cos 2k_y y)\,\hat{\mathbf{x}} + k_y \sin 2k_y y(1-\cos 2k_x x)\,\hat{\mathbf{y}}\right]. \tag{2.40}$$

As discussed in the one-dimensional case, when $M-m_d(B,\Sigma)>0$, i.e., $B\Sigma>0$, the drift is towards the antinodes. Fig. 2.7 presents the resultant time averaged drift force averaged over a period for the sphere with $M-m_d(B,\Sigma)>0$, and consequently the drift is towards the antinodes. On the other hand, when $M-m_d(B,\Sigma)<0$, i.e., $B\Sigma<0$, the drift is towards the nodes.

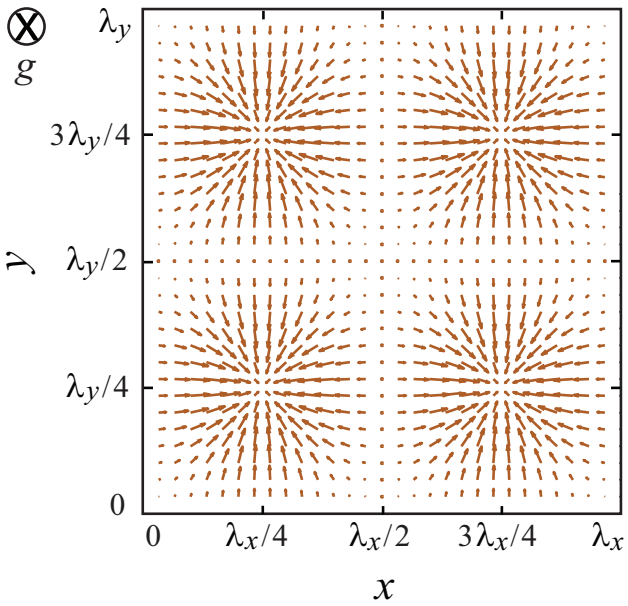

Figure 2.7: The drift force on a two-dimensional standing wave. The antinode points are at $\left((2n+1)\frac{\lambda}{4},(2n+1)\frac{\lambda}{4}\right)$ and the nodal lines are at $\left((n+1)\frac{\lambda}{2},(n+1)\frac{\lambda}{2}\right)$ with integer n. The time averaged drift force is shown for a sphere with $M-m_d(B,\Sigma)>0$ [the contact angle $\theta=74.3^\circ$ and the density ratio $D=1.05$]. As calculated in this case using Eq. 2.40, the drift is towards the antinodes.

Drift energy– The drift energy $E_d(x,y)$ is obtained by integrating the resultant 2D force $\vec{f}(x,y)$ with respect to the space. It is straightforward to check that the force field Eq. 2.40 is conservative and after integrating, the drift energy $E_d(x,y)$ is obtained as

$$E_d(x,y) = -\frac{M - m_d(B,\Sigma)}{16} u_0^2 [1 - \cos 2k_y y][1 - \cos 2k_x x]. \tag{2.41}$$

Here, the reference point $E_d(x,y) = 0$ is set to the nodal line. Therefore, when $M - m_d(B,\Sigma) > 0$ E_d is minimum at the antinode points, whereas when $M - m_d(B,\Sigma) < 0$ E_d is maximum at the antinodes. The equipotential lines of $E_d(x,y)$ are drawn for $M - m_d(B,\Sigma) > 0$ in Fig. 2.8.

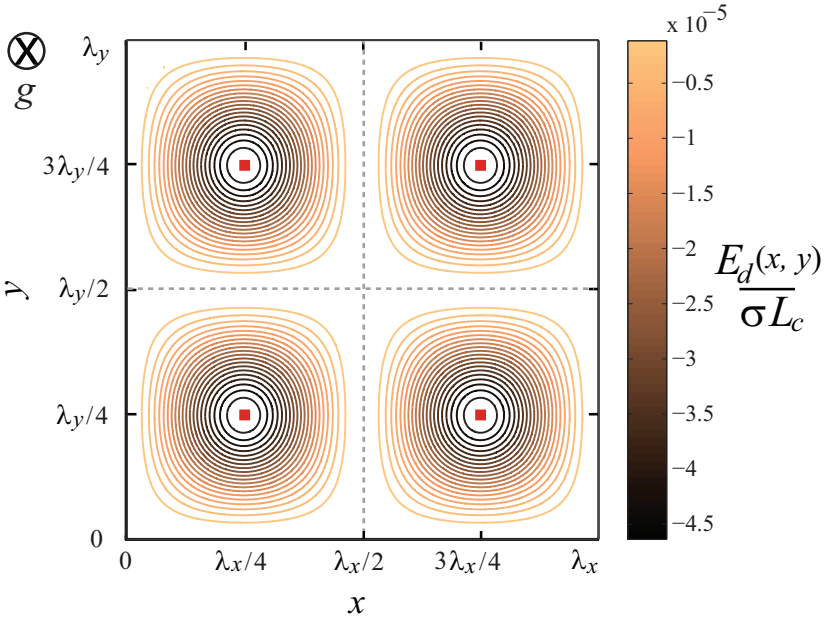

Figure 2.8: The equipotential energy contours of the drift energy $E_d(x,y)$ is presented for a sphere with $M - m_d(B,\Sigma) > 0$ on a two-dimensional standing wave. The colorbar indicates the magnitude of $E_d(x,y)$, non-dimensionalized by the surface tension coefficient σ and the capillary length $L_c = \sqrt{\sigma/\rho_l g}$ with liquid density ρ_l and acceleration of the gravity g, such that the energy is minimum at the dark regions and maximum at the bright regions. Note that the reference point $E_d(x,y) = 0$ is set to the nodal line. Therefore, since the antinodes (shown by small red rectangles) are more favorable than the nodes (shown by the gray dashed lines) for this sphere, the contours are brighter for the regions being close to the nodal lines.

2.4 The wave elevator

In the previous Section, we have discussed the drift force ignoring the time dependency of the submerged depth δ [see Eq. 2.30]. Even though the time dependency coming from the vertical displacement may have a negligible contribution to the resultant drift motion averaged over time, there would be some interesting dynamics hidden in a single wave period which has been also suggested in Refs. [8, 10]. Therefore, here, we will try to elucidate the time dependency of the sphere position on a standing wave in some more detail using qualitative arguments, without attempting a rigorous proof.

In Chapter 1, *General introduction*, the motion of a bubble induced by a concave static meniscus has been discussed. There, it has been stated that the unbalanced excess vertical force drives the bubble towards a local maximum so that the bubble climbs up. The bubble is hydrophilic and it is lighter than any carrier liquid. Therefore, the corresponding $B\Sigma(\theta, D) < 0$. If one makes an analogy for a sphere with $B\Sigma(\theta, D) > 0$, on the contrary to the bubble, the sphere moves towards a local minimum. These are valid for static curved interfaces.

However, for an oscillating curved interface, *i.e, a standing wave surface*, local minima and maxima vary within a wave period T. When $t < T/2$, the local minimum is the wave antinode (A) and the local maximum is the node (N). On the other hand, when $t > T/2$, the local minimum is the wave node (N) and the local maximum is the antinode (A). Consequently, the bubble moves towards N for $t < T/2$ and moves towards A for $t > T/2$, whereas the sphere with $B\Sigma > 0$ moves towards A for $t < T/2$ and moves towards N for $t > T/2$. Then, where is the resultant position of a small object floating on a standing wave?

The vertical wave acceleration $\ddot{\zeta}\,\hat{\mathbf{z}}$ oscillates with respect to t. (Here, we use $\ddot{\zeta} = \partial^2\zeta/\partial t^2$ for simplicity.) The vertical acceleration which the floater experiences is $g+\ddot{\zeta}$ when $t < T/2$ and $g-\ddot{\zeta}$ when $t > T/2$. Since the floater acceleration is larger for $t < T/2$ the contribution of this part of the wave cycle to the drift is larger. Therefore, in the *time averaged situation*, the bubble ($B\Sigma < 0$) drifts towards N, and so the sphere ($B\Sigma > 0$) towards A. This is consistent with the result suggested by the derived drift force given in Eq. 2.33. The time dependent drift within T is sketched in Fig. 2.9(a) for the sphere and in Fig. 2.9(b) for the bubble. The mechanism discussed here resembles an accelerating elevator, and so can be called a wave elevator.

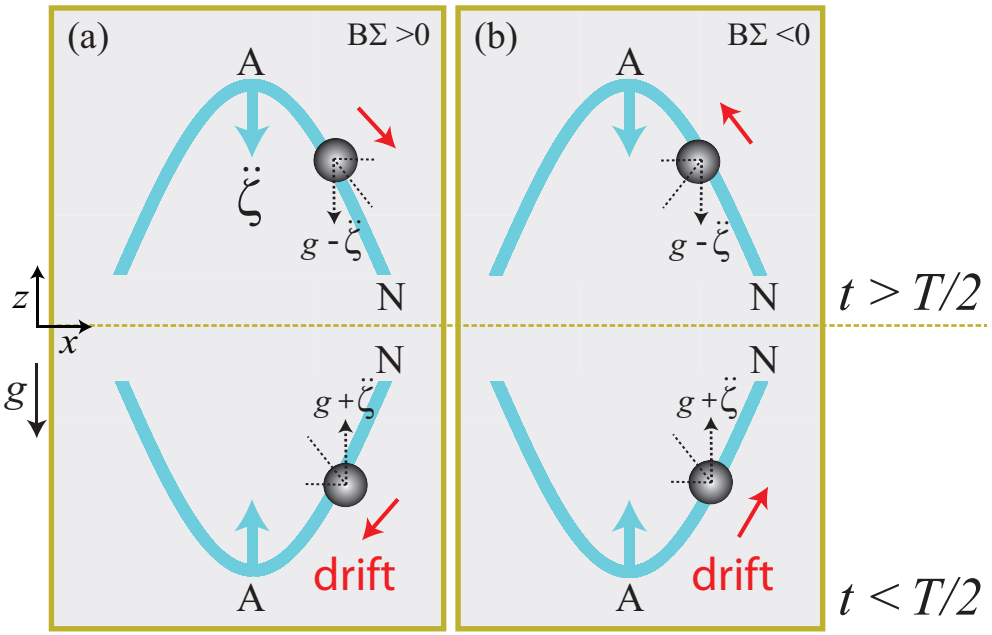

Figure 2.9: The wave elevator: The asymmetry in the vertical floater acceleration and the corresponding drift are illustrated for a sphere with $B\Sigma > 0$ (a), and a sphere or a bubble with $B\Sigma < 0$ (b). $\ddot{\zeta} = \partial^2\zeta/\partial t^2$ is the vertical surface wave acceleration and T is the wave period. Since the contribution of the drift in the lower cycle ($t < T/2$) is larger than the one shown above ($t > T/2$), on average, the floater in (a) drifts towards the antinode (A), whereas the floater in (b) drifts towards the node (N).

2.5 Conclusion

We have provided a summary of the physics of *floaters at interfaces under the influence of gravity*. More specifically, the static balance of a floating sphere, the modified buoyancy force with surface tension, and the capillary interaction between two identical floaters have been discussed. Furthermore, at an oscillating interface, the drift mechanism for a single floater has been described. Utilizing the knowledge from the static balance, the drift force provided in [8–10] has been slightly corrected. In addition, a more elaborate derivation of the drift force has been provided. Thus, we have presented the main ingredients to understand and characterize the observations of floating spheres both on static and dynamic interfaces. Additionally, we have emphasized and clarified the different regimes, i.e., the dependency on the physical parameters of the spheres.

There is an important remaining issue, namely how the drift mechanism, discussed here for a single sphere, works for many floating spheres on a standing wave. This will be the main question we will try to answer in the coming Chapter *From antinode clusters to node clusters*.

References

[1] D. Vella and L. Mahadevan, "The Cheerios effect", Am. J. Phys. **73**, 817–825 (2005).

[2] M. M. Nicolson, "The interaction betweeen floating particles", Proc. Cambridge Philos. Soc. **45**, 288–295 (1949).

[3] D. Y. C. Chan, J. D. Henry, Jr., and L. R. White, "The interaction of colloidal particles collected at fluid interfaces", J. Colloid Interface Sci. **79**, 410–418 (1981).

[4] N. D. Vassileva, "Behavior of 2D aggregates in shear flow", PhD Thesis, University of Twente (2006).

[5] N. D. Vassileva, D. van den Ende, F. Mugele, and J. Mellema, "Capillary forces between spherical particles floating at a liquid-liquid interface", Langmuir **21**, 11190–11200 (2005).

[6] M.-J. Dalbe, D. Cosic, M. Berhanu, and A. Kudrolli, "Aggregation of fric-

tional particles due to capillary attraction", Phys. Rev. E **83**, 051403-1–10 (2011).

[7] M. R. Maxey and J. J. Riley, "Equation of motion for a small rigid sphere in a nonuniform flow", Phys. Fluids **26**, 883–889 (1983).

[8] G. Falkovich, A. Weinberg, P. Denissenko, and S. Lukaschuk, "Floater clustering in a standing wave", Nature (London) **435**, 1045–1046 (2005).

[9] P. Denissenko, G. Falkovich, and S. Lukaschuk, "How waves affect the distribution of particles that float on a liquid surface", Phys. Rev. Lett. **97**, 244501-1–4 (2006).

[10] S. Lukaschuk, P. Denissenko, and G. Falkovich, "Nodal patterns of floaters in surface waves", Eur. Phys. J. Special Topics **145**, 125–136 (2007).

[11] J. B. Keller, "Surface tension force on a partly submerged body", Phys. Fluids **10**, 3009–3010 (1998).

[12] C. Duez, C. Ybert, C. Clanet, L. Bocquet, "Making a splash with water repellency", Nat. Phys. **3**, 180–183 (2007).

[13] P. K. Kundu and I. M. Cohen, *Fluid Mechanics*, (Elsevier Inc., USA) (2008).

[14] H. J. van Gerner, M. A. van der Hoef, D. van der Meer, and K. van der Weele, "Inversion of Chladni patterns by tuning the vibrational acceleration", Phys. Rev. E **82**, 012301-1–4 (2010).

[15] H. J. van Gerner, K. van der Weele, M. A. van der Hoef, and D. van der Meer, "Air-induced inverse Chladni patterns", J. Fluid Mech. **689**, 203–220 (2011).

3

From antinode clusters to node clusters *

A hydrophilic floating sphere that is denser than water drifts to an amplitude maximum (antinode) of a surface standing wave. A few identical floaters therefore organize into antinode clusters. However, beyond a transitional value of the floater concentration ϕ, we observe that the same spheres spontaneously accumulate at the nodal lines, completely inverting the self-organized particle pattern on the wave. From a potential energy estimate we show that at low ϕ antinode clusters are energetically favorable over nodal ones and how this situation reverses at high ϕ, in agreement with the experiment.

*Submitted as: Ceyda Sanlı, Detlef Lohse, and Devaraj van der Meer, "From antinode clusters to node clusters: The concentration dependent transition of floaters on a standing Faraday wave", Phys. Rev. Lett. (2012) and available at arXiv:1202.0051v1 .

3.1 Introduction

A small floating object at a liquid-gas interface exhibits a fascinating phenomenon when it is exposed to a periodic oscillation: On a standing wave surface, the floater moves either towards an amplitude maximum (antinode) or to an amplitude minimum (node) of the standing wave.[†] Whether a single floater goes to the node or to the antinode is determined by both the relative density of the floater compared to that of the carrier fluid and the floater hydrophobicity [1–3]: When the floater mass is larger than the displaced liquid mass [‡] the floater drifts to the antinode. In contrast, the floater drifts to the node when the floater mass is smaller than the displaced liquid mass. Furthermore, the drift continues throughout each wave period until the floater reaches the steady state position either at the antinode or at the node [1–3].

The dynamics of a single floater on a standing wave is understood, and the observation of the node clusters with a few hydrophilic light floaters is also reported in Ref. [1–3]. However, the collective motion of a monolayer of the floaters on a standing wave in the dense regime is an open question. Such kind of densely packed monolayer of floaters is called a floater (or particle) raft [4] and it has been shown that the floater raft has a peculiar behavior due to the attractive capillary interaction among the floaters [5, 6]. In the static case, heterogeneity of the floater packing [7] and both granular and elastic response of the floater raft [4] have been reported. However, how the floater raft behaves under driving is still unknown.

In this Chapter, we will combine these two independent research problems, namely initially loosely packed floaters on a standing wave and a static densely packed floater raft into a single experiment: We will study the position of hydrophilic heavy floaters on a standing Faraday wave as a function of the floater concentration ϕ, which is measured by determining the area fraction covered by the floaters in the area of interest, by simply adding additional floaters to the surface. In Section 5.2, we will experimentally show that the position of the floaters highly depends on ϕ. For low ϕ, our floaters accumulate at the antinode of the standing Faraday wave as would be expected from the theory and the previous experiments [1–3]. When we increase ϕ we will observe that the same hydrophilic heavy floaters cluster in the nodal region of the wave. Importantly, this inverted clustering is a collective effect of the floaters, and is not related to the inverted drift of a single floater by changing

[†] The mechanism is entirely discussed in Section 2.3 in the previous Chapter, but here we will give a brief summary.

[‡] In this case, both heavy hydrophilic and hydrophobic floaters can float by the help of surface tension. See Section 2.2.1 in the previous Chapter for further details.

the physical properties of the floater as discussed in the first paragraph. In our case, the single floater drift is always directed towards the antinodes.

To characterize the transition from the antinode clusters (low ϕ) to the node clusters (high ϕ), we will apply a spatial analysis of experimental image sequences for various ϕ in Section 5.2. We further focus on how the two main mechanisms driving the floater raft, the drift of a single floater due to the standing wave and the attractive capillary interaction among the floaters, vary by increasing ϕ. To understand this, a potential energy estimation of the floaters is developed in the scope of experimentally studied ϕ region in Section 3.3. Consequently, an agreement between the experiment and this energy argument is comparatively discussed.

3.2 Experiment

A schematic illustration of the experimental setup is shown in Fig. 3.1. A container, made from transparent hydrophilic glass with 10 mm height and 81×45 mm^2 rectangular cross section is attached to a shaker. The container is completely filled with purified water (Millipore water with a resistivity $>$ 18 MΩ·cm) such that the water level is perfectly matched with the container edge as shown in Fig. 3.1(f). In this way, a static surface inclination induced by the boundary is avoided [1–3]. This condition is called brim-full boundary condition [8]. Spherical polystyrene floaters, contact angle[§] 74° and density 1050 kg/m^3, with average radius R around 0.31 mm and a polydispersity of approximately 14% are carefully distributed over the water surface to make a monolayer of floaters. To avoid any surfactant effects, both the container and the floaters are cleaned by performing the cleaning protocol described in Ref. [9].

A standing Faraday wave is generated using a shaker which provides a vertical sinusoidal oscillation such that the vertical position of the container varies as a function of time t as $a_0 \sin(2\pi f_0 t)$, where f_0 is the shaking frequency and a_0 is the shaking amplitude. The f_0 is chosen to obtain a rectangular wave pattern with a wavelength in the range of 17 mm-24 mm. The corresponding f_0 to observe these wavelengths are in the range of 37 Hz-42 Hz (note that the standing Faraday wave frequency is equal to $f_0/2$). When adding floaters to the surface, both f_0 and a_0 need to be slightly adjusted to obtain a well defined rectangular pattern (see Appendix for further details).

[§]The contact angle is measured by satisfying the static balance discussed in Chapter 2. See Section 2.2.1 for further details.

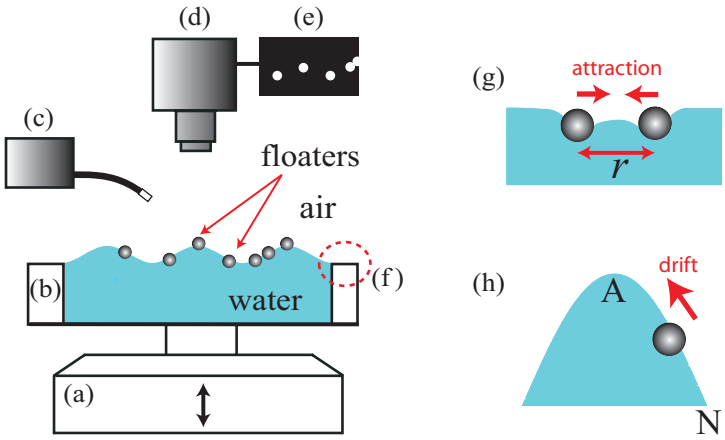

Figure 3.1: Experimental setup: (a) shaker, (b) glass container, 81×45×10 mm^3, (c) Schott fiber light source, (d) Photron Fastcam SA.1 (e) an illustration of a camera image, (f) pinned brim-full boundary condition, (g) the surface deformation around our hydrophilic heavy floaters, (h) the direction of the drift of a single floater on a standing wave, where A and N present the antinode and the node, respectively.

A continuous white fiber light source (Schott) is used to illuminate the particles from the side as shown in Fig. 3.1(c). The positions of the floaters are recorded with a high-speed camera (Photron Fastcam SA.1) at 500 frames per second. The lens (Carl Zeiss 60mm) is adjusted such that it focuses on the floaters at non-deformed water surface. Each image is 546 pixel × 1030 pixel (38 mm × 72 mm). The horizontal field of view is around 76% of the total cross section area of the container. (Total cross section is 81 mm×45 mm.) The maximum vertical displacement of the floaters is 2.5 ± 0.1mm, which is twice the maximally measured wave amplitude. The vertical depth of field is taken to be large enough to capture the floaters during this movement.

As described in Fig. 3.1(g) and Fig. 3.1(h), two competing mechanisms drive the floaters on the standing Faraday wave: The first one is the attractive capillary interaction [5, 6] due to the surface deformation around the floaters as shown in Fig. 3.1(g) provided that the distance between the floaters r is comparably less than the capillary length $L_c = \sqrt{\sigma/\rho_l g}$. Here, σ is the surface tension coefficient of the interface, ρ_l is the liquid density, and g is the acceleration of gravity. (For an air-water interface at 20°C, $L_c = 2.7$ mm.) Secondly, the single floater drift of our hydrophilic heavy floater on the standing wave being towards the antinode [1–3] (see also Section 2.3 in the

previous Chapter) is sketched in Fig. 3.1(h).

Observation— The control parameter of the experiment is the particle concentration ϕ, which is measured by determining the area fraction covered by the floaters in the area of interest, which is equal to or slightly smaller than the total horizontal field of view given above (76% of the total cross section of 81 mm$\times$45 mm). We examine how the distribution of the clusters on the standing Faraday wave varies depending on ϕ. The cluster distributions for two distinct limits, namely low ϕ and high ϕ, are displayed in Fig. 3.2(a) and (b), respectively. The experimental images taken from the top are presented together with the corresponding wave patterns indicated by the nodal lines, i.e., the standing wave amplitude minima and the antinode points, i.e., the amplitude maxima. The remarkable difference between these two states are clear: For low ϕ [Fig. 3.2(a)] the clusters float around the antinodes, whereas for high ϕ [Fig. 3.2(b)] the clusters are located around the nodal lines.

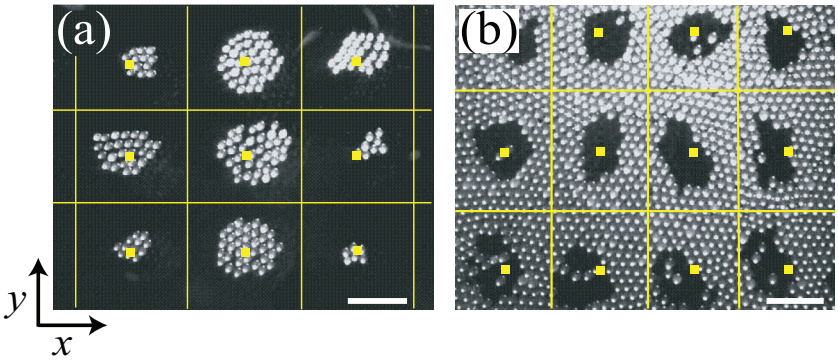

Figure 3.2: Experimental clusters of floaters on a rectangular standing wave. The nodal lines of the corresponding rectangular wave structures are represented by the yellow lines and the antinode points are indicated by the small yellow rectangles. The experimental snapshots show a stationary state when the surface wave elevation is nearly zero for the antinode clusters at ϕ=0.08 (a) and the node clusters at ϕ=0.61 (b). The white bars indicate a length scale of 5 mm.

Another remarkable difference between the antinode and the node clusters becomes clear when looking at their dynamics: The antinode clusters *breath*[¶], i.e., particles periodically move towards and away from the antinodes and, as a consequence, also from each other. In the nodal regions, there is also periodic motion (from and towards adjacent antinodes) but there the particles move collectively, and the particle

[¶]The breathing phenomenon considered in this Thesis has no relation to the breathing concept in solitons.

distance does not change. As a result, the node clusters *do not breath*. Now what is the origin of this breathing motion at the antinodes? To answer this question, the floater motion needs to be analyzed in the time-dependent case, i.e., we need to consider its motion within a wave cycle as was explained in Section 2.4 of the previous Chapter. The situation for our hydrophilic heavy floater could be summarized as follows: The floater moves to the antinodes while the surface acceleration is upwards, whereas the floater moves to the nodes while the surface acceleration is downwards. Since the contribution of the motion towards the antinodes is larger than that towards the nodes, the time averaged drift force, consequently, is towards the antinodes. Thus, the breathing motion of the antinode clusters is a resultant of both the motion in a half-wave period and the reciprocal motion in the other half-wave period like a periodically modulated source/sink. In Fig. 3.3(c), we see the source like pattern in the top-left and the bottom-right cluster and the sink-like pattern in the other two.

As a result of the breathing around the antinodes, the distance between the floaters and the antinodes varies in time so that the distances between the floaters also varies in time: Both distances increase when the surface acceleration is downwards (sources) and the distances decrease when the surface acceleration is upwards (sinks). However, the node clusters as a whole oscillate horizontally back and forth around the nodal line. So, within this motion, two adjacent floaters in the node clusters are not separated from each other [Fig. 3.3(f)], and unlikely the antinode clusters, no breathing is observed. This understanding will be used in Section 3.3 to create the floater clusters artificially on a two-dimensional wave.

In Fig. 3.3, we plot the spatial average of the distances to the first nearest neighbors as a function of time for both the antinode [Fig. 3.3(a)] and the node clusters [Fig. 3.3(d)]. The breathing effect of the antinode clusters shows up as a modulation of the average distance, which is not present in the node clusters case. Importantly, as a result of the breathing, the average distance of neighboring particles in the antinode clusters ($d_{nn}^E/2R = 1.38$) is considerably larger than that for the node clusters ($d_{nn}^E/2R = 1.17$).

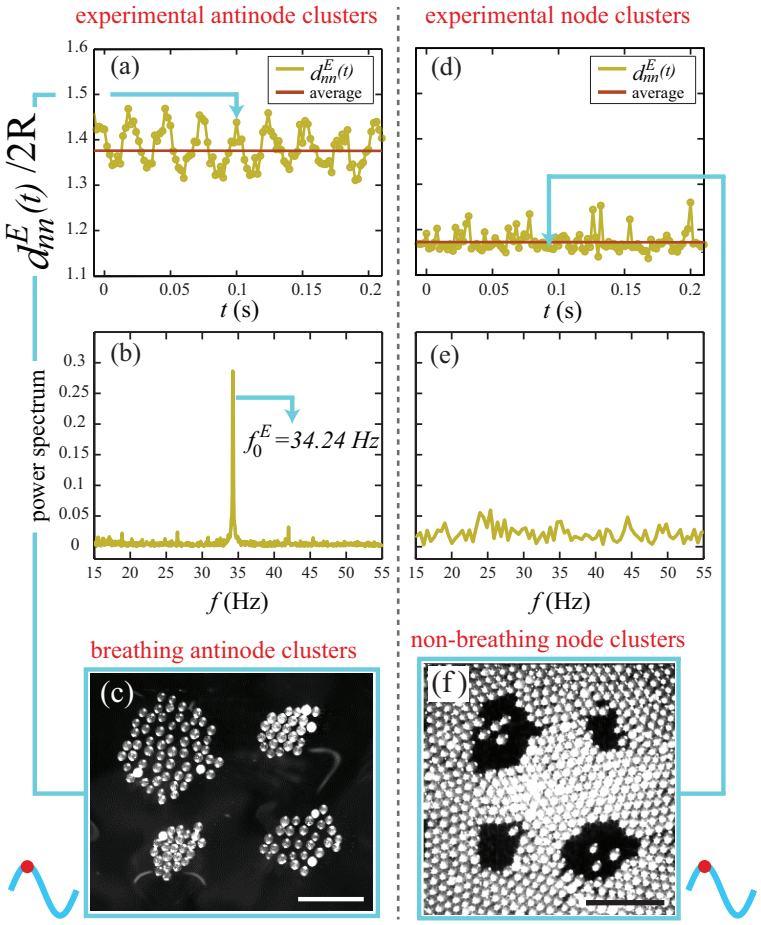

Figure 3.3: Breathing antinode clusters versus non-breathing node clusters. The experimentally measured nearest neighbor distances averaged over all particles $d^E_{nn}(t)$ normalized by the average particle diameter $2R$ is shown for the antinode clusters (a) and the node clusters (d) by the green circles. The brown lines correspond to the average values, $d^E_{nn}/2R = 1.38$ (a) and $d^E_{nn}/2R = 1.17$ (d) indicate the larger relative floater distance in the antinode clusters. The frequency analysis of $d^E_{nn}(t)$ gives the frequency component $f^E_0 = 34.24$ Hz, which is close to shaking frequency $f_0 = 37.81$ Hz when the standing Faraday wave is generated (*double* the resonance frequency of the standing Faraday wave due to the fact that there are clusters in different phases present on the different phases of the standing wave.). This suggests that the oscillation in $d^E_{nn}(t)$ is due to an asymmetric motion of the floaters within a wave cycle, and therefore the antinode clusters breath (c). No significant frequency is detected for the node case (e). Therefore, the relative distance of the floaters in the nodal line does not vary in time so that the node clusters do not breath (f). Note that here we only present small time windows (a, b, d, and e) and spatial regions (c, f), whereas both the average values and the frequency analysis are performed over 200 wave periods ($\approx 200 \times 0.05$ s$= 10$). In addition, the spatial analysis is evaluated considering the full experimental horizontal field of view. The bars indicate a length scale of 5 mm.

Experimental analysis— In order to examine this concentration dependent clustering of the floaters, we introduce the correlation c which quantifies to what extent the position of the clusters is correlated with the wave antinodes,

$$c = \frac{< \phi(\vec{r},t)a(\vec{r}) >_{\vec{r},t}}{< \phi(\vec{r},t) >_{\vec{r},t}}, \tag{3.1}$$

where $\vec{r}(x,y)$ is a two-dimensional space variable and the parenthesis $<>_{\vec{r},t}$ indicates that the average is taken with respect to both $\vec{r}$ and t. Here, $\phi(\vec{r},t)$ is the spatiotemporal floater concentration measured by converting each experimental image to a black-white (binary) image so that the fraction of white pixels provides the corresponding $\phi(\vec{r},t)$. The wave distribution $a(\vec{r})$ is a function which is positive around the antinodes and negative in the nodal regions of the standing wave. The spatial average is performed over the total horizontal field of view and the time average is computed using the experimental images over approximately 200 wave periods ($\approx 200 \times 0.05 = 10$ s). To eliminate the contribution of floater motion into the third dimension, only images where the wave elevation is nearly zero are used.

The wave distribution $a(\vec{r})$ is defined as

$$a(\vec{r}) = \begin{cases} \beta a_{cos}(\vec{r}) & \text{, when } \vec{r} \text{ is at the antinodes } (a_{cos}(\vec{r}) > 0), \\ a_{cos}(\vec{r}) & \text{, when } \vec{r} \text{ is at the nodes } (a_{cos}(\vec{r}) < 0). \end{cases}$$

Here, $a_{cos} = 2[\cos k_x(x-\Delta_x)]^2[\cos k_y(y-\Delta_y)]^2 - 1$, with k_x, k_y the wave numbers in the x,y-direction and where the spatial phase shifts Δ_x and Δ_y are chosen such that $a_{cos}(\vec{r}) = 1$ when $\vec{r}$ is at the antinode points, whereas $a_{cos}(\vec{r}) = -1$ at the nodal lines. To check the robustness of c regarding the precise form of $a(\vec{r})$, we also use a step function $a_{step}(\vec{r})$ with $a_{step}(\vec{r})$ equals 1 in the antinode regions and -1 in the node regions [$a_{cos}(\vec{r}) > 0$ and $a_{cos}(\vec{r}) < 0$, respectively]. Positive values of c thus indicate that there are more floaters around the antinodes than the nodes, and vice versa for the negative values of c. A constant β is introduced such that $c = 0$ when particles are equally distributed over the two-dimensional wave surface [‖].

In Fig. 3.4, we present $c(\phi)$ for both a_{cos} (red circles) and a_{step} (blue squares). Remarkably, three distinct regions are observed: Region I (low ϕ) where $c > 0$ represents the antinode clusters. Region II (intermediate ϕ) represents the transition state with $c \approx 0$, which in experiment are characterized by elongated clusters moving over the entire surface. Region III (high ϕ) indicates $c < 0$ where the node clusters are found. We conclude that there is a broad transition from the antinode to the node clusters.

[‖] This is necessary since the area of the nodal regions is larger than that of the antinodes.

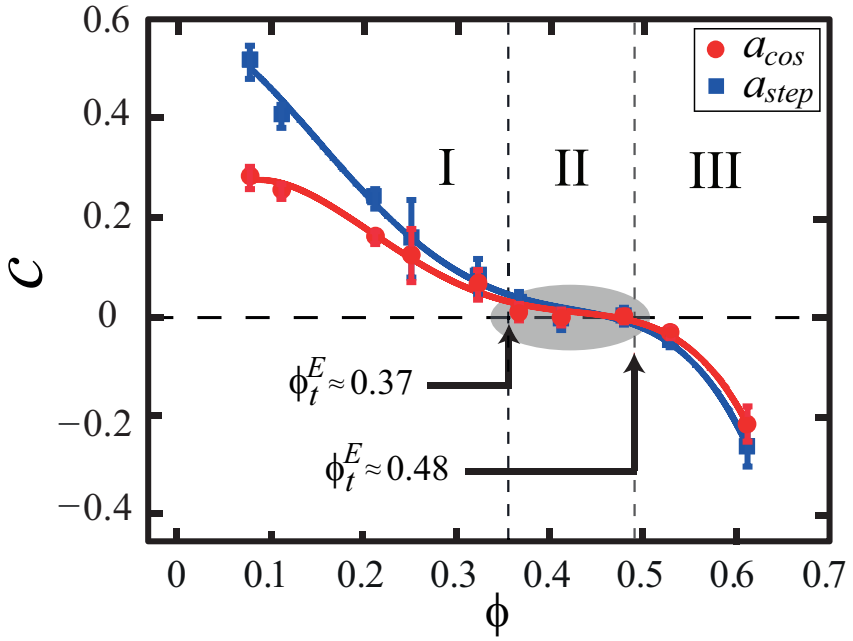

Figure 3.4: Experimental transition from the antinode to the node clusters. The correlation $c(\phi)$ is shown both for a_{cos} (red circles) and for a_{step} (blue squares). The solid lines are the polynomial fits to the data to guide the eye. The experimental transition region from the antinode to the node clusters are between $\phi_t^E \approx 0.37$ and $\phi_t^E \approx 0.48$ when $c \approx 0$ for both a_{cos} and a_{step}. The shaded area indicates the transition region. The corresponding error bars indicate the robustness of c. (The mean values of each ϕ are the overall time averages of the experimental data. The error bars are the standard deviations of the time averages obtained by using a subset of a quarter of the data from the corresponding mean value.)

3.3 Analytical model

We will now investigate how the single floater drift and the attractive capillary interaction between the floaters cooperate to create the observed patterns [Fig. 3.2(a,b)]. This we will do by comparing the potential energy of artificially created antinode and node clusters, for the construction of which it is essential to describe the experimentally observed patterns in some greater detail. Antinode clusters [Fig. 3.2(a)] are characterized by the breathing effect discussed in the previous Section: In each period of the standing wave, the clusters are alternately driven towards and away from the antinodal point, such that the average distance between the neighboring particles is considerably larger than their diameter $2R$. For the node clusters breath-

ing is absent; the floaters move collectively, as rafts, and the distance between the nearest neighbors is equal to $2R$ at the nodal lines.

To artificially determine the floater positions in the clusters, we create *two different* two-dimensional hexagonal lattices, one centered at the antinode [Fig. 3.5(a)] and the other centered at the node [Fig. 3.5(b)]. To account for the breathing effect, the distance between the neighboring particles is larger than $2R$ in the center of the antinode cluster. The distance decreases towards the edge to $2R$, and vice versa for the node cluster.

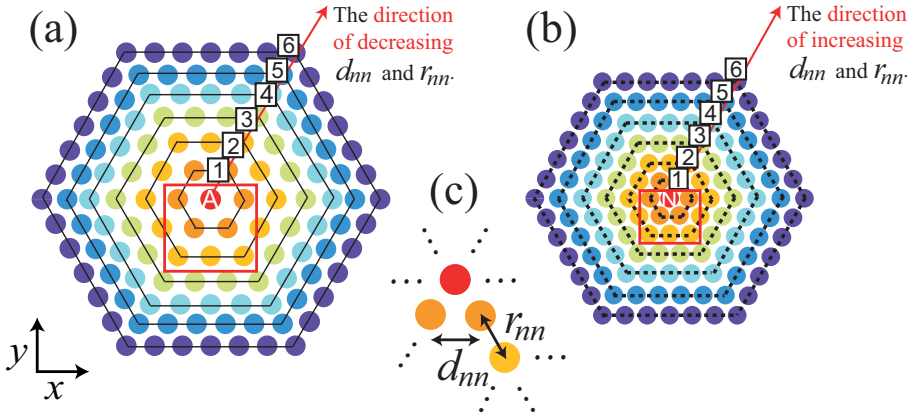

Figure 3.5: To include the effect of breathing in our analysis, we artificially design antinode clusters (a) and node clusters (b). For each case, a hexagonal lattice is grown by adding centered hexagonal rings (solid and dashed lines). There, the nearest neighbor distance d_{nn} [Fig. (c)], for both cases, is chosen to match the larger distance between the particles in the antinodes. By this way, agreement with the breathing observed in the experiment is satisfied. Similar to this procedure, the distance r_{nn} between the rings is also fixed. Details can be found in the following Section.

Designing two-dimensional artificial clusters on a standing wave

We will describe how the antinode clusters and the node clusters are artificially created to perform the energy estimation of the floaters. In this study, the three-dimensional time-dependent floater motion on a wave surface is approximated as a two-dimensional motion, namely the motion in $xy-$plane. Moreover, in contrast to the polydisperse spheres (with polydispersity 14%) used in the experiment, the floaters here are assumed to be monodisperse disks. For simplicity, furthermore,

hexagonal packing is considered in the clustering for each floater concentration ϕ. Finally, to increase ϕ, hexagonal rings are drawn around a centered floater (either at the antinode or at the node) as presented in Fig. 3.6(a) with dotted dashed lines. The floater number in each hexagonal ring is equal to $6i$, where i is the hexagonal ring index.

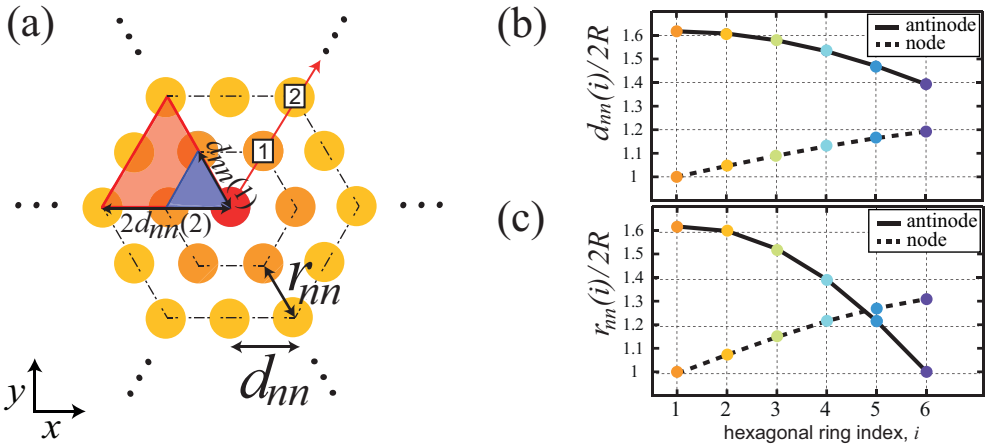

Figure 3.6: (a) The methodology to design artificial floater clusters. The centered red floater is either at the antinode or at the node. The centered hexagonal rings, described with dotted dashed lines, are drawn for the index $i = 1, 2, \ldots$. The nearest neighbor distance within the ring d_{nn} and the nearest neighbor distance between two nearby hexagonal rings r_{nn} are shown. The small [blue shaded] and the big [red shaded] equilateral triangles are illustrative to derive the expression for r_{nn}. To perform an artificial breathing, $d_{nn}(i)$ (b) and $r_{nn}(i)$ (c) both non-dimensionalized by $2R$ are shown for the antinode clusters [solid line] and for the node clusters [dashed line].

To perform the breathing motion of the clusters as explained in the earlier Section, the distance between the floaters decreases from the antinodes to the nodes both for the antinode clusters and the node clusters. So, the following distances are needed to be defined, namely d_{nn}, i.e., the distance between the nearest neighbors within a hexagonal ring, and r_{nn}, i.e., the distance of the nearest neighbors between two nearby hexagonal rings as described in Fig. 3.6(a). First, $d_{nn}(i)$ is defined as

$$d_{nn}(i) = (\xi\, a - 2R)\, \sin k\, i\, 2R + 2R, \tag{3.2}$$

where ξ is a constant, a is the wave amplitude, k is the wave number, and R is the average radius of the floater. (Hexagonal ring index i used in this expression should not

be confused with the imaginary unit i defined in complex numbers.) In the present analysis, $\xi = 1.24$ for the antinode clusters and $\xi = 0.6$ for the node clusters are fixed. By using tracer particles, we measure $a \sim 0.8$ mm for the antinode clusters and $a \sim 1.2$ mm for the node clusters.

In Fig. 3.6(b), the corresponding values of $d_{nn}(i)$ are plotted. Decreasing behavior of $d_{nn}(i)$ from the antinodes [low i] to the nodes [high i] for the cluster centered at the antinode is shown by the solid line, whereas increasing behavior of $d_{nn}(i)$ from the nodes [low i] to the antinodes [high i] for the cluster centered at the node is shown by the dashed line.

Furthermore, $r_{nn}(i)$ is derived from a recurrence relation deduced from the equilateral triangles [Fig. 3.6(a)]: Each length of the equilateral triangle is equal to $i\,d_{nn}(i)$. Similarly, each length of the nearest smallest equilateral triangle is equal to $(i-1)\,d_{nn}(i-1)$. Consequently, r_{nn} is

$$r_{nn}(i) = i\,d_{nn}(i) - (i-1)\,d_{nn}(i-1). \tag{3.3}$$

Similar to $d_{nn}(i)$ [Fig. 3.6(b)], in Fig. 3.6(c), decreasing behavior of $r_{nn}(i)$ from the antinodes [low i] to the nodes [high i] for the configuration of an antinode cluster is shown by the solid line. In contrast, increasing behavior of $d_{nn}(i)$ from the nodes [low i] to the antinodes [high i] for the configuration of a node cluster is shown by the dashed line.

Therefore, the resultant designed antinode and node clusters, inspired by the experimental counterparts demonstrated in Fig. 3.2, are described in Fig. 3.7(a, b), respectively.

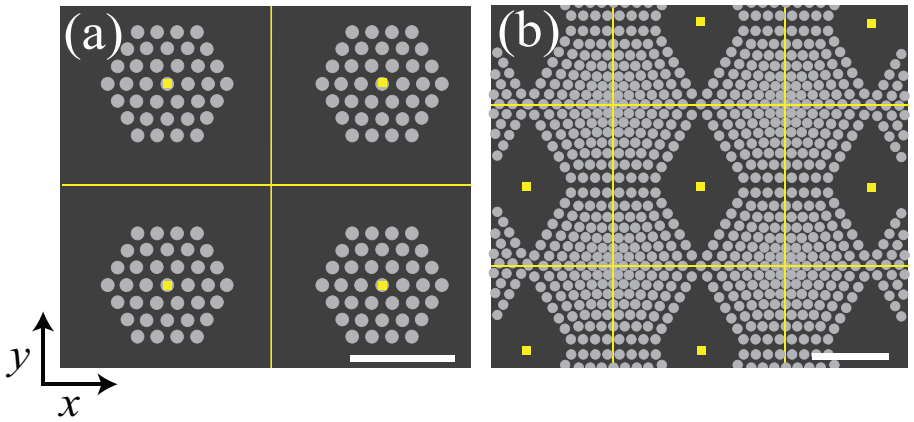

Figure 3.7: The configurated antinode clusters at ϕ=0.1 (a) and node clusters at ϕ=0.44 (b) are shown with indicating the corresponding rectangular wave patterns. The nodal lines are represented by the yellow lines and the antinode points are marked by the small yellow rectangles. The white bars indicate a length scale of 5 mm.

Energy calculation

We will calculate the potential energy of the floaters for both the antinode [Fig. 3.7(a)] and the node [Fig. 3.7(b)] configurations: The first contribution to the total potential energy $E(\phi)$ is the capillary energy $E_c^T(\phi)$, which we estimate as the sum of the capillary energies $E_c(r)$ of all floater pairs as was already defined in Section 2.2.4 in the previous Chapter. Here, r is the (two-dimensional) distance between the floaters in each pair. We use the approximation $E_c(r) \propto K_0(r/L_c)$, which is valid for small surface deformations [5, 6]. Here, K_0 is the zeroth order modified Bessel function of the second kind and L_c the capillary length. The second contribution is the drift energy $E_d(\phi)$, which is the sum of the drift energies $E_d(x,y) \propto (1-\cos 2k_y y)(1-\cos 2k_x x)$ of the single floaters that depend on their positions (x,y) with respect to the wave [1–3]. The more detailed information about $E_c(r)$ and $E_d(x,y)$, and their full expressions including the corresponding prefactors are provided in Section 2.2.2 in the previous Chapter.

In Fig. 3.8(a) we plot the total potential energy for both the configuration of the antinode clusters and that for the node clusters. When ϕ increases, the potential energy per floater increases for the configuration of the antinode clusters, whereas it decreases for the the configuration of the node clusters. There is a crossover, the calculated transition point, $\phi_t^C \approx 0.36$, separating the low ϕ region, where the config-

urated antinode clusters are seen to be energetically favorable, from the high ϕ case where the configurated node clusters have the lowest potential energy. In addition, this crossover value is very close to the values lying in the experimental transitional region of Fig. 3.4, i.e., $\phi_t^E \approx 0.37$ and $\phi_t^E \approx 0.48$, and is therefore in good agreement with our experimental observations. (The superscript in $E_c^T(\phi)$ is dropped for notational convenience.)

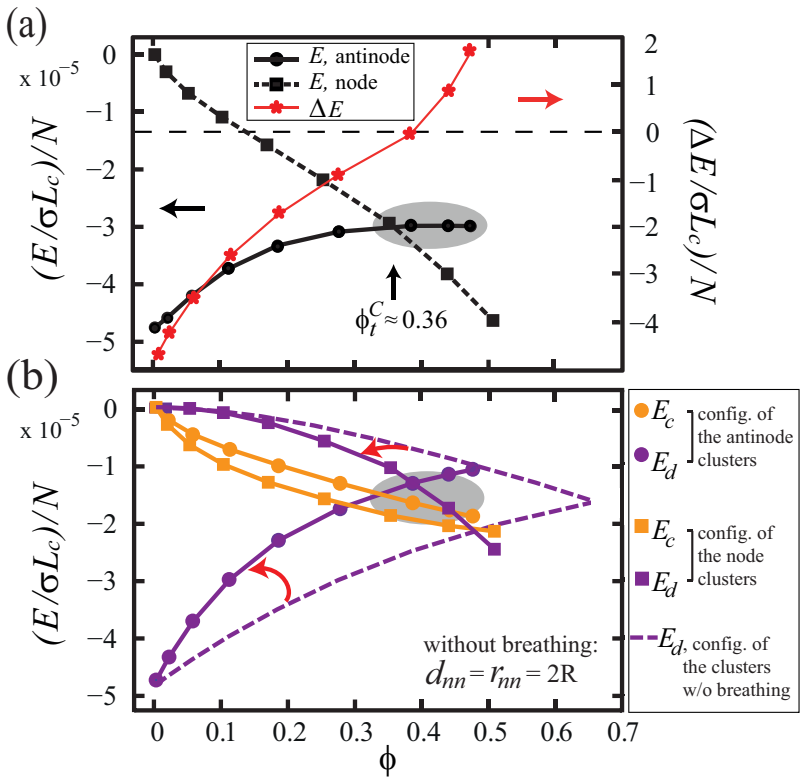

Figure 3.8: Calculated transition from the configurated antinode clusters to the configurated node clusters by the energy calculation. (a) The total potential energy of the floaters $E(\phi)$, non-dimensionalized by σL_c and further normalized by the number of floaters N, is shown both for the configurated antinode clusters (circles with a solid line) and that for the configurated node clusters (squares with a dashed line). $\Delta E(\phi)$ (red stars) represents the energy difference between the configurated antinode and node clusters. (b) The capillary energies $E_c(\phi)$ for the configurated antinode (orange circles) and node (orange squares) clusters together with the drift energies $E_d(\phi)$ for the configurated antinode (purple circles) and node (purple squares) clusters. The purple dashed lines represent the corresponding drift energies without taking the breathing effect into account. In both plots, the shaded areas indicate the transition region suggested by the experiment [Fig. 3.4].

To understand the origin of the crossover we now turn to the drift [$E_d(\phi)$] and capillary [$E_c(\phi)$] constituents of $E(\phi)$ in Fig. 3.8(b). Let us discuss $E_d(\phi)$ first. Since the single floater drift is towards the antinodes, $E_d(\phi)$ of the antinode clusters is minimum at low ϕ. When the clusters centered at the antinodes are grown, the floaters are placed at the regions close to the nodes, where $E_d(\phi)$ is higher. Thus, $E_d(\phi)$ increases for higher ϕ. The reverse scenario is valid for the node clusters, so that $E_d(\phi)$ decreases for higher ϕ. The crossover of $E_d(\phi)$, which happens for almost the same value of ϕ as that of $E(\phi)$, emphasizes the importance of E_d in the transition. The breathing effect is essential for the existence of the crossover: When we set the nearest neighbor distance to the particle diameter $2R$ in everywhere, the energy of the configurated node clusters is always higher than that of the configurated antinode clusters up to a very high value of ϕ [dashed lines in Fig. 3.8(b)]. Therefore, no crossover in the experimental transitional region is determined without implementing the breathing. Turning to the capillary potential energy $E_c(\phi)$, we see that there is only a small difference: Due to the breathing, $E_c(\phi)$ decreases slightly sharper for the configurated node clusters since the average distance between the floaters there is smaller than that of the configurated antinode clusters.

From the above we learn that viewing the antinode-to-node-cluster transition as a competition between the drift (driving floaters towards the antinodes) and the capillary attraction (which is weakened in the antinodes due to the breathing effect) is simply wrong. The dominant effect is that the breathing induces a low packing fraction around the antinodes, which in turn causes a steep increase of the drift energy with the number of floaters. This makes nodal clusters energetically favorable already when only drift energy is taken into account. The role of the capillary interaction is just to keep the floater particles self-organized in rafts; without this attractive interaction the floaters would be freely drifting around instead of forming clusters.

3.4 Conclusion

In summary, in this Chapter we study the role of the floater concentration ϕ on the spatial distribution of the floaters on the standing Faraday wave. By performing several well-controlled experiments, we observe that, at low ϕ, the hydrophilic heavy floaters form clusters at the antinodes of the standing Faraday wave. The result at low ϕ suggests agreement with the theory of [1–3]. At high ϕ, with the same floaters, unexpectedly inverted patterns, with clusters at the nodal lines of the wave, are observed. To understand such a collective behavior of the floaters, the total energy

of the floater system is calculated, which explains the observations for both ϕ limits. More specifically, the transition point found from our energy calculation (ϕ_t^C) lies within the experimental transitional region (ϕ_t^E). The differences between the experiment and the analysis may well be explained from the fact that in the latter we assume a hexagonal packing: The experimentally observed patterns exhibit a variety of shapes and packings to reach an energetically minimum configuration at certain ϕ values, whereas in our energy estimation, the clusters are designed by only considering the hexagonal symmetry for all ϕ for simplicity. Therefore, this would imply a more complex scenario than the one we assume here, and therefore for an even better quantitative agreement the morphological information of the clustering at intermediate ϕ would need to be included. To this end, in the following Chapter *Morphology of the clusters*, we will characterize the morphological differences in the clustering when ϕ increases in detail.

Appendix

Generating a standing Faraday wave with floaters

Frequency and amplitude of a standing Faraday wave— A standing Faraday wave is generated by a vertically vibrated container filled with a fluid. When the fluid layer with a free surface is vertically oscillated, a parametric instability occurs while the oscillating amplitude a_0 becomes greater than a critical amplitude a_c. The phenomenon was first investigated by Faraday [10] and associated with his name after that. The resultant standing surface wave, in our case, is only a subharmonic response of the vertical driving such that the resonance frequency of the wave $f = f_0/2$, where f_0 is the shaking frequency at the resonance and f is the wave frequency.

In this study, the presence of the floaters alters the physical properties of the water such as the surface tension σ and the density ρ_l near the free surface. So, the resonance frequency of the wave f cannot be represented by the inviscid dispersion relation [11] $\omega_k^2 = \left[gk + (\sigma/\rho_l k^3)\right] \tanh kH$, where $\omega = 2\pi f$, k is the wave number, g is the acceleration of the gravity, and H is the depth of the water. The resonance frequency f is experimentally determined by sweeping the shaking frequency to obtain a rectangular wave pattern. By adding more floaters to the system, the procedure is repeated to find the corresponding f. The shaking amplitude a_0 is an important parameter, and should be adjusted to work with a well-defined rectangular pattern. Therefore, f, in other words f_0, is checked for several a_0 values to obtain the pattern

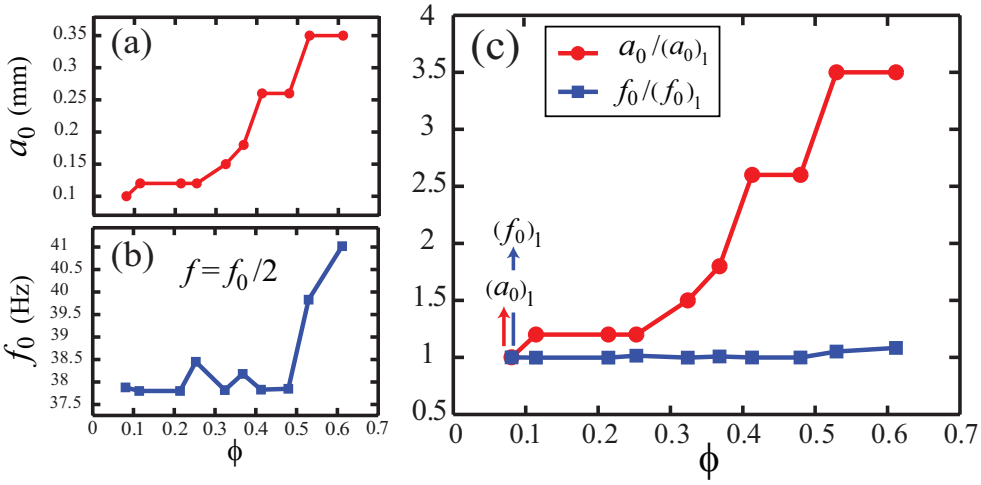

Figure 3.9: (a) The shaking amplitude a_0 and (b) the shaking frequency at the resonance f_0 to create the standing Faraday wave with floaters are represented as a function of ϕ. The standing wave frequency $f = f_0/2$. The resultant wave pattern for each ϕ is rectangular with a wavelength in the range of 17 mm-24 mm both for $x-$direction and for $y-$direction. (c) a_0 normalized by a_0 of the lowest ϕ $(a_0)_1$ is shown as the red circles, and f_0 normalized by f_0 of the lowest ϕ $(f_0)_1$ is presented as the blue squares.

with desirable wavelengths for each floater concentration ϕ. In the experiment, f_0 is in the range of 37 Hz-42 Hz, a_0 is in the range of 0.1 mm-0.35 mm, and the subharmonic response with $f = f_0/2$ observed for each f_0 and a_0 combination. The reason why the rectangular pattern is desired is to be able to identify the wave structure, namely the antinodes and the nodal lines, based on two dimensional experimental image sequences. In Fig. 3.9(a)(b), $a_0(\phi)$ and $f_0(\phi)$ are presented, respectively. However, Fig. 3.9(c) can be more instructive. Detailed study is necessary to obtain a more precise form of $a_0(\phi)$ and $f_0(\phi)$.

Initial conditions– On the undisturbed water surface, the floaters initially form clusters induced by the attractive capillary interaction [5, 6]. To dissipate the initial clusters and to produce the stationary standing wave, the method used in Refs. [1–3] is applied. An important adjusting parameter is ε, $\varepsilon = (a_0 - a_c)/a_c$, where a_c is the minimum required shaking amplitude to exhibit the parametric instability. First, at a slowly varying frequency, the system is vibrated with a small vibration amplitude a_0, namely $\varepsilon \ll 1$. Then, a_0 is increased such that $\varepsilon \gg 1$, considerably, to randomize

the floater distribution. By keeping slowly varying frequency, we decrease a_0 while still satisfying $\varepsilon > 1$. When a rectangular stationary standing wave is generated, a_0 and f_0 are kept fixed. Consequently, the required parameters, a_0 and f_0, are found experimentally to generate the standing wave and this procedure is repeated after adding more floaters to the system.

References

[1] G. Falkovich, A. Weinberg, P. Denissenko, and S. Lukaschuk, "Floater clustering in a standing wave", Nature (London) **435**, 1045–1046 (2005).

[2] P. Denissenko, G. Falkovich, and S. Lukaschuk, "How waves affect the distribution of particles that float on a liquid surface", Phys. Rev. Lett. **97**, 244501-1–4 (2006).

[3] S. Lukaschuk, P. Denissenko, and G. Falkovich, "Nodal patterns of floaters in surface waves", Eur. Phys. J. Special Topics **145**, 125–136 (2007).

[4] P. Cicuta and D. Vella, "Granular character of particle rafts", Phys. Rev. Lett. **102**, 138302-1–4 (2009).

[5] D. Vella and L. Mahadevan, "The Cheerios effect", Am. J. Phys. **73**, 817–825 (2005).

[6] D. Y. C. Chan, J. D. Henry, Jr., and L. R. White, "The interaction of colloidal particles collected at fluid interfaces", J. Colloid Interface Sci. **79**, 410–418 (1981).

[7] M. Berhanu and A. Kudrolli, "Heterogeneous structure of granular aggregates with capillary interactions", Phys. Rev. Lett. **105**, 098002-1–4 (2010).

[8] S. Douady, "Experimental study of the Faraday instability", J. Fluid Mech. **221**, 383–408 (1990).

[9] C. Duez, C. Ybert, C. Clanet, L. Bocquet, Nat. Phys. 3, 180 (2007). See the section Methods for the cleaning protocol of both hydrophilic (wetting) glass material and hydrophobic teflon (non-wetting) particles. Note that we immerse the hydrophilic glass container in piranha solution (1 vol H2O2, 2 vol H2SO4) for 25 min. The cleaning procedure for our hdrophilic polystyrene consists of rinsing the spheres with isopropanol. Then, both the container and the spheres are dried separately, and fur-

ther heated to remove all the chemicals. Since the spheres are hydrophilic polystyrene, the suggested heating temperature is 70°C at most. We heated the spheres, as well as the container, at 65°C for 1 hour. Finally, both the container and the spheres are left to cool to ambient temperature.

[10] M. Faraday, "On the forms and states assumed by fluids in contact with vibrating elastic surfaces", Philos. Trans. R. Soc. London 121, 319–340 (1831).

[11] P. K. Kundu and I. M. Cohen, *Fluid Mechanics*, (Elsevier Inc., USA) (2008).

4

Morphological analysis of floater patterns on a standing Faraday wave * †

Macroscopic spherical particles spontaneously form rich patterns on a standing Faraday wave. These patterns are found to follow a very systematic trend depending on the floater concentration ϕ: The same floaters that accumulate at amplitude maxima (antinodes) of the wave at low ϕ, surprisingly move towards the nodal lines when ϕ is beyond a certain value. In more detail, the circular irregularly packed antinode clusters at low ϕ are replaced by loosely packed filamentary structures at intermediate ϕ, and then followed by densely packed grid-shaped node clusters at high ϕ. Here, we characterize the morphology of these patterns in various ways. The observed variations in the cluster formation as a function of ϕ can be quantified through either a global or a local analysis. More specifically, we employ Minkowski functionals, the local bond orientational order parameter, and the pair correlation function for this quantification. Furthermore, we compare the results from this analysis to that obtained from the global correlation coefficient introduced in Chapter 3.

*Ceyda Sanlı, Detlef Lohse, and Devaraj van der Meer, "Morphological analysis of floater patterns on a standing Faraday wave" (to be submitted to Phys. Rev. E, 2012).

†We acknowledge Sascha Hilgenfeldt for useful discussions.

4.1 Introduction

Both physical and biological many-body systems show emergence of collective behavior. In ferromagnetic systems, by decreasing the temperature, spins align themselves even without any external field and exhibit a spontaneous magnetization [1]. In nonequilibrium two-dimensional Ising models, the transverse and the longitudinal segregation of up and down spins, with respect to the direction of the slowest spin exchange rate, have been analytically predicted [2]. In macroscopic systems such as vertically shaken dry granular media, a swirling motion [3] and also several forms of orientational order [4] have been observed for anisotropic beads, and rotation rate-dependent stratification patterns induced by granular avalanche in a rotating drum have been demonstrated [5, 6]. (A detailed, extensive review on pattern formation and collective behavior in granular matter can be found in Ref. [6].)

Similar to physical systems, in biological systems biological cells form patterns spontaneously [7, 8]. Furthermore, swarms of birds move collectively in a randomly chosen direction, and so reach the emergence of ordered states [9]. In addition, hybrid models have been introduced to connect the collective behavior in granular media (and also any other particle-based system) to that in swarming agents [10, 11]. For all examples, the corresponding length scale that emerges in such macroscopic phenomena, spontaneous magnetization, segregation, rotation, pattern formation and swarm groups, is much larger than any of the microscopic length scales, i.e., spin, bead, cell, or fish sizes or distances. The fact that this large-scale behavior appears to have many similarities suggests that there are universal laws or characterizations that explain this large variety of phenomena.

In the present Chapter, we specifically consider the collective behavior of floating small spheres on a standing Faraday wave. These floaters exhibit a surprising transition as a function of the floater concentration ϕ [See Chapter 3]: At low ϕ, the floaters accumulate at amplitude maxima (antinodes) of the wave, whereas the same floaters move towards the nodal lines when ϕ is beyond a certain value. In more detail, the circular irregularly packed antinode clusters at low ϕ are replaced by loosely packed filamentary structures at intermediate ϕ, and then followed by densely packed grid-shaped node clusters at high ϕ. Here, we will calculate and interpret the morphological details of this variety of patterns. More specifically, we will use Minkowski functionals, the local bond orientational order parameter, and the pair correlation function for analysis. We stress that our system is distinctly different from dry granular matter since the floaters experience an attractive force as a result of the gravity-induced capillary interaction. In addition, there is a drift force,

that drives the floaters to the antinodes of the standing wave. Both the attractive capillary force and the drift force have been discussed in detail in Chapter 2.

The attractive capillary and the drift forces compete with each other. Consequently, the floaters organize themselves in different patterns, depending on which force dominates. The mechanism by which the pattern formation occurs is distinct from the other physical and biological systems that have been studied in the literature. However, similar to those the resultant floater patterns have long-range order (relative to the size of an individual floater). Before introducing the floater patterns, we first turn to Faraday wave systems without floaters which have been studied extensively [12–18].

Faraday waves, which appear on the free surface of a vertically shaken liquid layer, have in their own right been one of favorite sources to study pattern formation in physics for decades. The rich variety of patterns obtained by varying the mode numbers of a standing Faraday wave were analyzed experimentally [12]. There, quasi-linear theories were successful to explain the parametrically excited eigenmodes of the free surface for both inviscid [13] and viscous [14] liquids. Beyond this quasi-linear regime, there is a broad nonlinear region which has been revealed by several experimental studies: There exist chaotic wave patterns [15] in containers with different geometries and wetting properties that are large compared to the wavelengths; there are rotationally symmetric patterns [16] which were also predicted by theory [17] in a circular container, and scarred patterns were observed in a stadium-shaped container [18]. All of these can be considered as just a few examples taken from the extensive literature on nonlinear Faraday wave patterns with a free surface.

Pattern formation associated with Faraday waves has become an even richer field with the observation of the patterns that floating spheres form on such a wave pattern [19–21]. It has been shown that macroscopic spherical particles floating on a standing Faraday wave with a rectangular wave pattern spontaneously form very organized clusters. These patterns can be traced back to a drift that the floaters experience due to the standing wave when the floater radius R is small relative to the wavelength λ, (see Section 2.3.1 in Chapter 2 for further details). Through this mechanism, a small number of identical hydrophilic heavy spherical floaters organizes into antinode clusters. On the same rectangular wave pattern, we found that, just by increasing the number of floaters, the floater pattern completely inverts: The floaters now cluster along the nodal lines instead of the antinodes (see Chaper 3 and Ref. [22]).

In this Chapter, we focus on the characterization of the details of the cluster formation. When we go from the antinode cluster to the node clusters by increasing the floater concentration ϕ, we observe that not only the position of the clusters, but also their size and shape vary. As also mentioned above, two competing mechanisms are expected to create the floater clusters, namely drift and attractive capillary forces (both of which have been discussed in detail in Chapter 2). Therefore, the wavelength λ, the capillary length $L_c = \sqrt{\sigma/\rho_l g}$, and the floater radius R are the typical length scales which should characterize the resultant clusters. Here, σ is the surface tension coefficient of the interface, ρ_l is the liquid density (the liquid is water in this study), and g is the acceleration of gravity. (For an air-water interface at 20°C, $L_c = 2.7$ mm.) For our system $\lambda \gg L_c \gg R$. This wide range of length scales of interest makes us perform the analysis of our system both globally ($\sim \lambda$) and locally ($\sim R$).

Before discussing the methodology and the analysis, in Sec. 4.2, we will present our experimentally observed floater patterns including the intermediate ϕ case. To characterize the patterns specifically with respect to λ, in Section 4.3, we will then introduce and discuss the Minkowski point pattern approach followed by our analysis of the patterns as a function of ϕ. Our aim is not only to examine global characteristics but also the nature of the packing and short-range order within the clusters. To this end, in Section 4.4, we will use the local bond orientational order parameter and the pair correlation function, with which we will quantify order and disorder in the packings and the clusters for length scales smaller than L_c.

4.2 Floater patterns

The experimentally observed floater patterns on a standing Faraday wave are shown in Fig. 4.1 where snapshots have been taken from the top at a phase in which the wave elevation is nearly zero. For all cases, the wave pattern itself is rectangular with wavelengths $\lambda_x \approx \lambda_y \approx 20R$ for the x and y-direction respectively.

Clearly, the route from the antinode clusters at low ϕ [Fig. 4.1(a)] to the node clusters at high ϕ [Fig. 4.1(f)] includes many different stages of varying particle mobility: We observe mobile antinode clusters [Fig. 4.1(b)], large, loosely packed clusters [Fig. 4.1(c)], loosely packed filamentary clusters [Fig. 4.1(d)], and densely clustered regions [Fig. 4.1(e)]. It is clear that, the quantitative analysis of such variety of structures and packings poses a considerable challenge. Therefore, several methods will be employed to arrive at a satisfactory understanding and quantification.

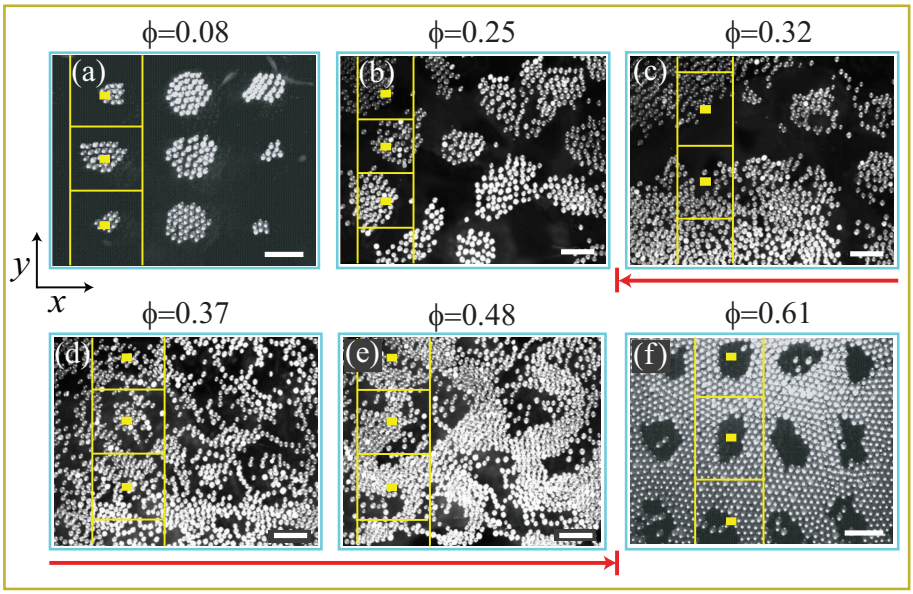

Figure 4.1: Floater patterns on a standing Faraday wave with a rectangular wave pattern for various floater concentrations ϕ. To indicate the corresponding wave structures, in a small subset of the field of view the antinodes and the nodes are presented by small yellow rectangles and yellow lines, respectively. The images which lie in (also nearby) the transition region from antinode to node clusters (see Chapter 3), are marked by the red line. The morphological differences in the clusters are clear: At low ϕ, circular, irregularly packed antinode clusters are observed (a, b). At intermediate ϕ, when we enter the transition region, clusters with a large heterogeneity in space evolve (c). Further into the transitional region, loosely packed filamentary structures occur (d), which when ϕ increases even more evolve into densely clustered regions (e) from which finally densely packed grid-shaped node clusters form (f). The white bars indicate a length scale of 5 mm.

4.3 Global analysis

In this Section, Minkowski functionals will be used to quantify the floater patterns illustrated in Fig. 4.1 in a global manner. We naturally restrict ourselves to the Minkowski functionals point pattern approach in two dimensions. Before introducing the functionals and discussing the approach, we will first give a brief background.

The Minkowski functionals are a set of functionals which provide information of geometry, shape (i.e. curvature), and connectivity of any pattern of interest. They have been successfully employed to characterize large-scale structures such as galaxy samples [23], turbulent and regular patterns in chemical reaction-diffusion systems [24], spinodal decomposition structures in a simulation [25] and also in an experiment of a colloid-polymer mixture [26], particle and bubble distributions in turbulent flow [27], and aggregations of colloids at fluid interfaces [28]. Detailed extensive reviews can be found in Refs. [29, 30], and the sensitivity of the method for some data sets in comparison with the other methods are discussed in Ref. [31].

The Minkowski functionals $\widetilde{M}_0(D), \widetilde{M}_1(D), \widetilde{M}_2(D), \ldots, \widetilde{M}_\nu(D)$ are functionals of integral geometry, which are additive, motion-invariant, and continuous on a given domain D in $d-$dimensional Euclidean space [25]. Mathematically, the $\widetilde{M}_\nu(D)$ are defined as [26]

$$\begin{aligned} \widetilde{M}_0(D) &= \int_D d^d\vec{r}, \qquad (4.1) \\ \widetilde{M}_\nu(D) &= \frac{\omega_{d-\nu}}{\omega_\nu \omega_d} \frac{(\nu-1)!(d-\nu)!}{d!} \int_{\partial D} \sum_{\{i_1,\ldots,i_{\nu-1}\}} \frac{1}{R_{i_1}\ldots R_{i_{\nu-1}}} d^{d-1}\vec{r}, \text{ when } \nu \geq 1, \end{aligned}$$

where $\omega_d = \pi^{d/2}/\Gamma(1+d/2)$ is the unit volume in d dimensions, ∂D is the boundary of the domain D, and R_i are the principal radii of curvature with $i = 1, \ldots, d-1$. Here, the summation is performed over the multiplication of all permutations i_ν of $d-1$ curvatures.

In two dimensions ($d = 2$, $\nu \leq 2$), using Eq. 4.1, there are three Minkowski functionals [26]

$$\begin{aligned} \widetilde{M}_0(D) &= \int_D d^2\vec{r}, \\ \widetilde{M}_1(D) &= \frac{1}{2\pi}\int_{\partial D} d\vec{r}, \\ \widetilde{M}_2(D) &= \frac{1}{2\pi^2}\int_{\partial D}\frac{1}{R}\, d\vec{r}, \end{aligned} \tag{4.2}$$

where $d^2\vec{r}$ and $d\vec{r}$ are the Lebesgue measures in two and one-dimensional Euclidean spaces, respectively. Here, $M_0(D)$ is the area of D, $M_1(D)$ is proportional to the perimeter of D, and $M_2(D)$ is proportional to the measure of the connectivity, called Euler characteristic (commonly labeled by χ). In this study, instead of the exact values of the functionals, we are interested in their actual physical meanings. Therefore, as is also done in Ref. [28], we slightly redefine the prefactors in Eq. 4.2

$$\begin{aligned} M_0(D) &= \boxed{\text{area of } D,} \\ M_1(D) &= \boxed{\text{perimeter of } D} \quad \Big(= 2\pi\widetilde{M}_1(D)\Big), \\ M_2(D) &= \boxed{\text{Euler characteristic of } D} \quad \Big(= \pi\widetilde{M}_2(D)\Big). \end{aligned} \tag{4.3}$$

The Euler characteristic may appear to be a complicated quantity, but we point out that for a circular cluster with radius $R_\circ$ with the definition in Eq. 4.3 we simply have

$$M_2(D) = \frac{1}{2\pi}\int_0^{2\pi}\frac{1}{R_\circ}\, R_\circ\, d\varphi = 1, \tag{4.4}$$

whereas for a circular hole of radius $R_\circ$, we obtain

$$M_2(D) = \frac{1}{2\pi}\int_0^{2\pi}\left(-\frac{1}{R_\circ}\right) R_\circ\, d\varphi = -1. \tag{4.5}$$

The above results can be shown to hold for non-circular clusters and holes too, such that the Euler characteristic is simply found to be equal to

$$\boxed{\text{Euler characteristic} = \text{number of clusters} - \text{number of holes.}} \tag{4.6}$$

Therefore, if there are only distinct clusters, the Euler characteristic $M_2(D) > 0$, whereas if there are only distinct holes $M_2(D) < 0$. (In the present Thesis, the connectivity or

the Euler characteristic is called M_2 in contrast to the common notation χ used in the literature to keep the notation consistent with the other Minkowski functionals.)

We will now introduce some further quantities that will help us in the physical interpretation of the Minkowski functionals. To this end, $M_\nu(D)$ can be decomposed to two parts, one for the clusters and the other for the holes such that

- $[M_0(D)]_{\text{clusters}}$=total area of D,
  (i.e., including the area occupied by the holes of D),
- $[M_1(D)]_{\text{clusters}}$=total external perimeter of D,
  (i.e., disregarding the perimeter occupied by the holes of D),
- $[M_0(D)]_{\text{holes}}$=total area of holes in D,
  (i.e., total area occupied by the holes of D),
- $[M_1(D)]_{\text{holes}}$=total perimeter of holes in D,
  (i.e., total perimeter of the holes in D).

Furthermore, $M_2(D)$ is already in its decomposed form [Eq. 4.6]. If we connect these decomposed quantities with the actual $M_0(D)$ and $M_1(D)$, we have

$$\begin{aligned} M_0(D) &= [M_0(D)]_{\text{clusters}} - [M_0(D)]_{\text{holes}}, \\ M_1(D) &= [M_1(D)]_{\text{clusters}} + [M_1(D)]_{\text{holes}}. \end{aligned} \tag{4.7}$$

$M_2(D)$ has already been given in Eq. 4.6. Both the clusters and the holes can be visualized for an arbitrary pattern. An example can be found in Fig. 4.2, which demonstrates one of M. C. Escher's famous drawing constructed of repeating white fish (representing the clusters in this example) on a black background and black birds (representing the holes).

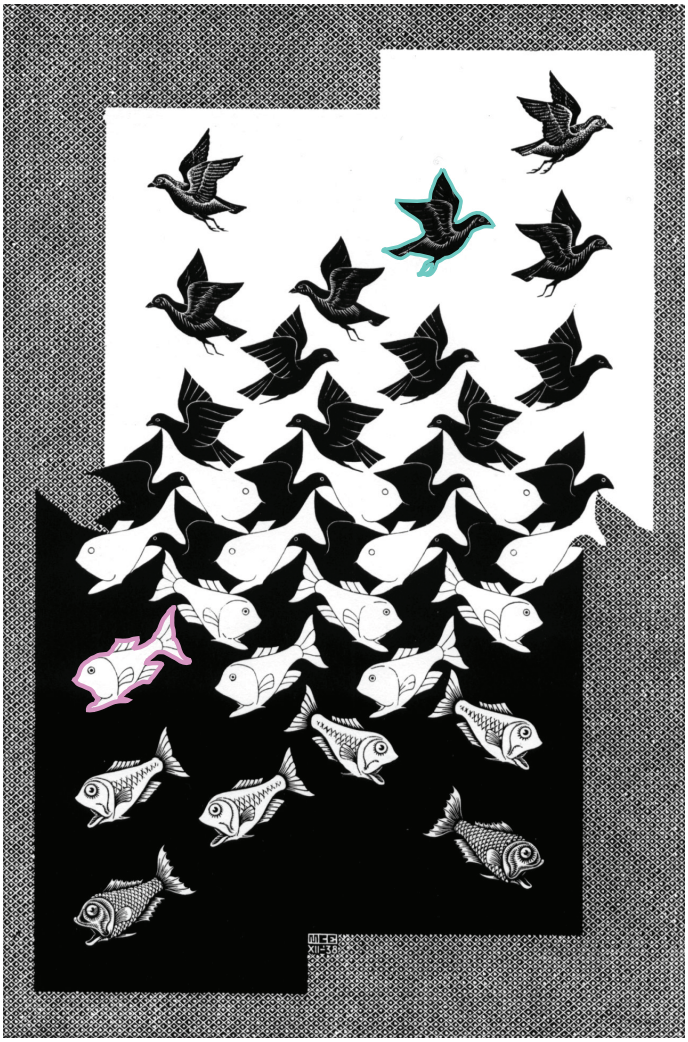

Figure 4.2: Illustration of clusters and holes in Escher's drawing of repeating fish and birds. Here, the white fish on a black background enclosed by the pink line indicates a cluster, whereas the black bird on a white background enclosed by the blue line indicates a hole. Consequently, $[M_0(D)]_{\text{clusters}}$ and $[M_1(D)]_{\text{clusters}}$ are the total area and the total perimeter of the region enclosed by the pink line. In addition, the corresponding $M_2(D) = 1$. On the other hand, the area and the perimeter of the region enclosed by the blue line are $[M_0(D)]_{\text{holes}}$ and $[M_1(D)]_{\text{holes}}$, respectively. In this case, $M_2(D) = -1$.

4.3.1 Minkowski point pattern approach

A system of particles can be viewed as a collection of points defined by the positions of the particle centers. To study the morphological properties of the set of points (such as clustering), discs of radius r are drawn around each particle center and then r is varied. As an example of a pattern constructed with discs of increasing radius r for an intermediate floater concentration ($\phi = 0.37$, in the transition region) we show in Fig. 4.3. With r increasing from the particle radius R to $3R$, the resultant pattern changes due to the merging of isolated particles into groups (of particles), as shown in Fig. 4.3(a) to (c). In the first figure, all particles are separate, whereas in the second they almost all become connected. The large number of holes disappear when r is further increased, as illustrated by the third figure.

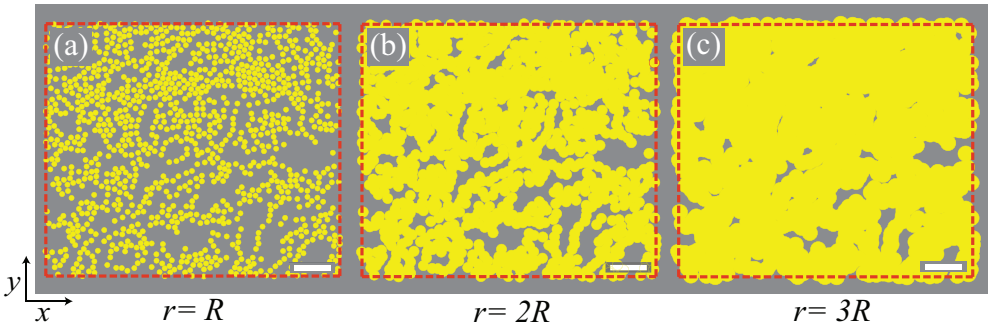

Figure 4.3: The Minkowski point pattern approach is demonstrated using the particle pattern at the intermediate floater concentration $\phi = 0.37$ [see Fig. 4.1(d) for the corresponding experimental image]. Here, we show the morphological deformation of the particle pattern when the Minkowski radius r increases from the particle radius R (a), which provides an image identical to the experimental one, to twice the radius $2R$ (b), and finally to three times the radius $r = 3R$ (c). The dashed (brown) lines are the boundaries of the corresponding experimental image. The white bars indicate a length scale of 5 mm.

The morphology of this pattern can be quantified by the Minkowski functionals, which are introduced in Eqs. 4.3-4.7. In short, we now determine the area, perimeter, and Euler characteristic of the particle pattern in Fig. 4.3 as a function of the Minkowski radius r.

4.3.2 Experimental results

The three Minkowski functionals in two dimensions are given by Eq. 4.3. In this case, since the corresponding domain D varies by increasing r, the functionals are called $M_v(r)$. Here, we also use their dimensionless forms

$$\begin{aligned} M_0^*(r) &= \frac{M_0(r)}{N\pi r^2}, \\ M_1^*(r) &= \frac{M_1(r)}{N2\pi r}, \\ M_2^*(r) &= \frac{M_2(r)}{N}, \end{aligned} \tag{4.8}$$

where N is the total number of floaters. With this non-dimensionalization we compare the area of the pattern $M_0(r)$ with the area of just as many non-overlapping discs of the same size, and similarly for $M_1(r)$ we divide the perimeter of the pattern with the sum of the perimeters of N non-overlapping discs. Finally, $M_2(r)$ is non-dimensionalized by the Euler characteristic of N non-overlapping spheres, which is N.

The reason behind this particular non-dimensionalization is that $M_0(r)$ and $M_1(r)$ trivially increase with the radius r as the surface area (πr^2) and perimeter $(2\pi r)$ of a disc of radius r. Non-dimensionalizing the Minkowski functionals as proposed in Eq. 4.8 compensates for this trivial scaling of the Minkowski functionals. In addition, the extra factor N by which the functionals are divided brings about that in the limit $r \ll R$, where we are dealing with N separate discs, all three Minkowski functionals are equal to one: $M_0^*(r) = M_1^*(r) = M_2^*(r) = 1$.

Note that in all experimental analysis, we apply the Minkowski point pattern approach by disregarding the experimental image boundaries such that, for each iteration of the disc radius r, an unbounded two-dimensional resultant pattern is considered as was shown in Fig. 4.3.

The calculated dimensionless functionals based on the experimental data are shown in Fig. 4.4 for values of ϕ spanning the whole range of patterns, i.e from antinode to node clusters. For all floater concentrations ϕ, we find that when we increase r, the functionals decay due to merging of the disks. When r becomes larger than the floater radius R, the discs start to overlap. Therefore, the normalized area of the resultant pattern $M_0^*(r)$ [Fig. 4.4(a)] and the normalized perimeter $M_1^*(r)$ [Fig. 4.4(b)] become smaller when $r > R$. The normalized Euler characteristic $M_2^*(r)$ [Fig. 4.4(c)] first reaches to negative values, because when particles start to merge into clusters they first leave holes in between, each of which adds -1 to the Euler characteristic.

Then, when r increases further, the holes close and we are left with the number of clusters, i.e., $M_2^*(r)$ becomes positive again.

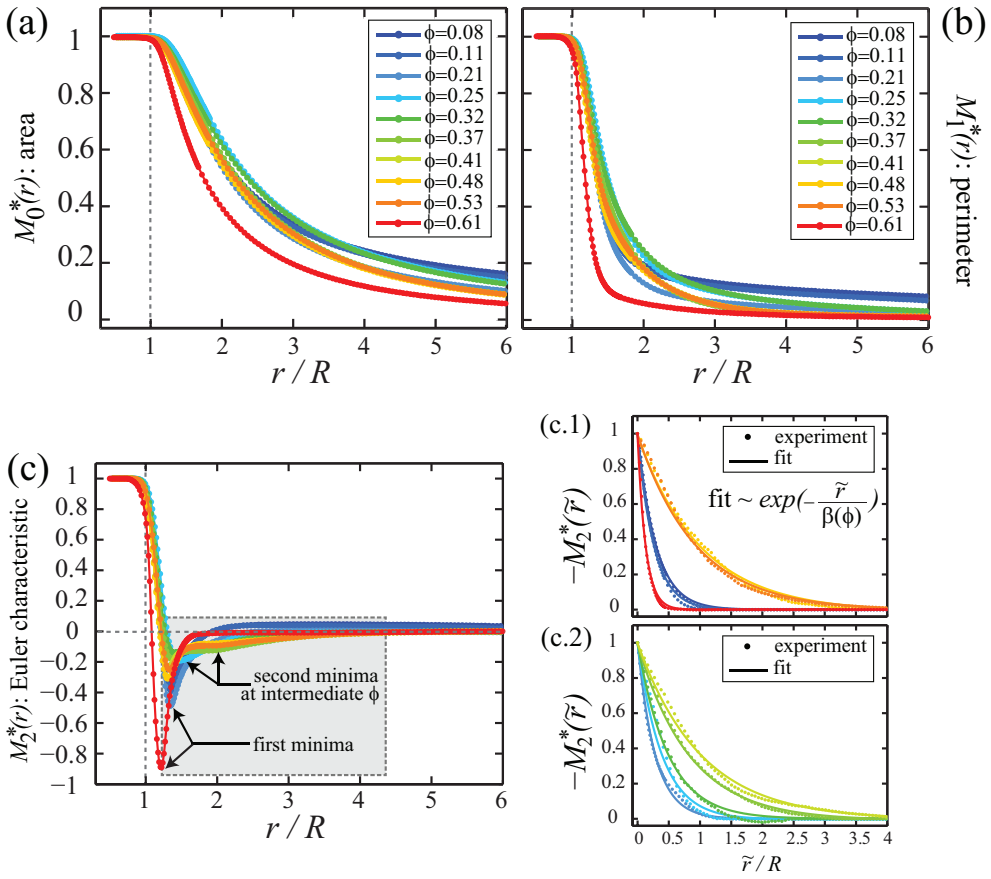

Figure 4.4: The three dimensionless Minkowski functionals of the experimental data from antinode clusters at low ϕ (blue) to node clusters at high ϕ (red) as a function of r normalized by the floater radius R. The normalized area $M_0^*(r)$ (a), the normalized perimeter $M_1^*(r)$ (b), and the Euler characteristic $M_2^*(r)$ (c) are presented. The decay in the curves when $r > R$ indicate increasing amount of overlapping regions due to merging of the disks. Smoother decays at intermediate ϕ (relative to that at low and high ϕ) suggest that more heterogenous and filamentary structures [Fig. 4.1(b-e)] evolve in comparison with the compact circular antinodes [Fig. 4.1(a)] and grid-shaped node clusters [Fig. 4.1(f)]. (c.1, c.2) The decaying part of $-M_2^*(\tilde{r})$ is shown with the corresponding exponential fit. [Shaded gray rectangle in (c): Both the first minima and the second minima are marked. Remarkably, the second minima are only generated at intermediate ϕ, neither at low ϕ nor high ϕ.] The experimental values and the corresponding fits are presented by dots and solid lines, respectively.

The corresponding experimental images that have been introduced in Fig. 4.1 can be instructive to understand the differences in the curves. The idea behind it is as follows: For compact and circular structures such as antinode clusters at low ϕ [Fig. 4.1(a)], the functionals are expected to decay more quickly than for elongated antinode clusters [Fig. 4.1(b)], heterogenous structures [Fig. 4.1(c)], and filamentary structures [Fig. 4.1(d)] at intermediate ϕ. The reason is that the overlapping regions for compact structures are larger than those for filamentary structures at the same r so that the functionals for compact structures decay sharply. This therefore suggests that the decay rate $\beta(\phi)$ [Fig. 4.4(c)] can be used as a measure of the heterogeneity of the pattern: The exponential decays are expected to be sharp for low and high ϕ, where we have antinode and node clusters distributed over the wave surface in an organized way. Consequently, small $\beta(\phi)$ is expected. However, at intermediate ϕ, as mentioned, elongated and filamentary structures occur in a more heterogeneous distribution relative to the antinode and the node clusters so that a smooth exponential decay occurs, i.e., large $\beta(\phi)$.

To investigate the validity of these arguments on the decay of the Minkowski functionals discussed here, we quantify the decay of $M_0^*(r)$, $M_1^*(r)$, and $M_2^*(r)$. Since $M_0^*(r)$ and $M_1^*(r)$ for all ϕ start to decay at the same point $r = R$, we quantify the decay by taking their value at $r = 2R$. [For larger values of r we obtain similar trends as a function of ϕ as presented in Fig. 4.5(a).] In Fig. 4.5(a), the magnitudes of $M_0^*(r = 2R)$ and $M_1^*(r = 2R)$ are presented as a function of ϕ. Both are normalized by their values at the lowest ϕ so that they are equal to 1 for the lowest ϕ, where we observe circular antinode clusters as demonstrated in Fig. 4.1(a).

The situation is different for $M_2^*(r)$ [Fig. 4.4(c)]. $M_2^*(r)$ first quickly descends to a negative minimum and then increases again towards a value around zero. Therefore, in this case we choose a different procedure to examine the corresponding decay: We look beyond the minimum[‡] of $M_2^*(r)$ and try to locally fit an exponential $-M_2^*(r) \sim \exp(-r/\beta(\phi))$, as shown in Fig. 4.4(c.1,c.2)[§] in the gray shaded region of Fig. 4.4(c). At low ϕ and the highest ϕ, there is one minimum, however, at intermediate ϕ, two minima exist. We apply the exponential fit to the region beyond the second minimum at intermediate ϕ. $\beta(\phi)$ is the corresponding exponential decay rate. In Fig. 4.5(b), $\beta(\phi)$ is plotted as a function of ϕ.

All decays indicate three regions: circular (compact) antinode clusters at low ϕ where we observe sharp decays, i.e., small $M_0^*(r = 2R)$, $M_1^*(r = 2R)$, and $\beta(\phi)$, fil-

[‡]Or minima, since for intermediate ϕ there are sometimes two minima before the decay sets in.
[§]The figure is split into two parts (c.1,c.2) for better visualization.

amentary (heterogeneous) clusters at intermediate ϕ where we observe smooth decays, i.e., large $M_0^*(r=2R)$, $M_1^*(r=2R)$, and $\beta(\phi)$, and the decays become sharp again for grid-shaped node clusters at high ϕ.

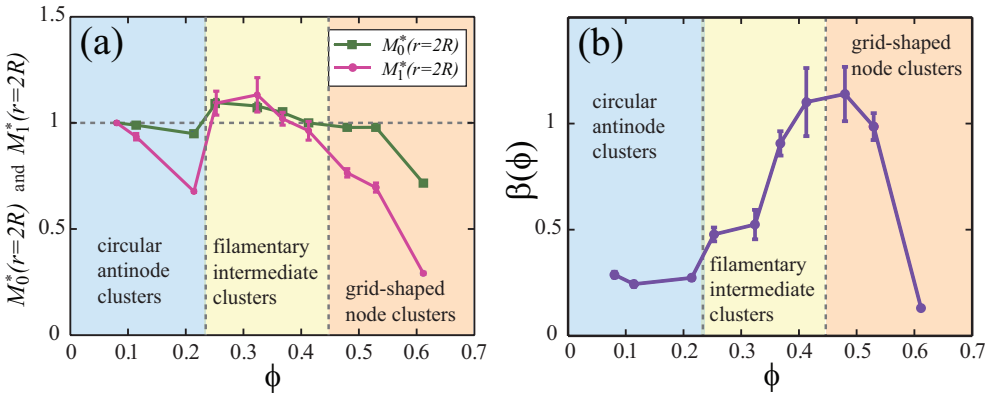

Figure 4.5: Quantification of the decay of the three Minkowski functionals. (a) The magnitude of the first two Minkowski functionals, namely $M_0^*(r)$ [area] and $M_1^*(r)$ [perimeter], for $r = 2R$, normalized by those obtained at the lowest value of ϕ. (b) The exponential decay rate $\beta(\phi)$ in the region where $-M_2^*(\tilde{r})$ decays. All values increase for filamentary and more heterogeneous clusters at intermediate ϕ, and they all tend to decrease when the clusters are more homogeneous and compact. (The mean values of each ϕ are the overall time averages of the experimental data. The error bars are the standard deviations of the time averages obtained by using a subset of a quarter of the data from the corresponding mean value.)

4.3.3 Physical interpretation of the Minkowski functionals

We have shown that characterizing the decay of the functionals works to identify the morphological differences in the clustering patterns. However, a direct physical interpretation of the three Minkowski functionals is hard to provide. It is however feasible to construct quantities from the Minkowski functionals that do have an intuitive physical meaning. For example, if we divide the total area $[M_0(D)]_{\text{clusters}}$, which disregards the open spaces that are contained within the clusters as defined in the previous Subsection, by the number of clusters $[M_2(D)]_{\text{clusters}}$, we obtain the average cluster area $\overline{A}(r)$. We can do a similar division for the average perimeter $\overline{P}(r)$, leading to

- $\overline{A}(r) = \frac{[M_0(r)]_{\text{clusters}}}{[M_2(r)]_{\text{clusters}}}$,
- $\overline{P}(r) = \frac{[M_1(r)]_{\text{clusters}}}{[M_2(r)]_{\text{clusters}}}$.

Finally, we define the average aspect ratio $\overline{S}(r)$ as $\overline{S}(r) \equiv \overline{P}^2(r)/4\pi\overline{A}(r)$ which gives

- $\overline{S}(r) = \frac{[M_1^2(r)]_{\text{clusters}}}{4\pi[M_0(r)]_{\text{clusters}}[M_2(r)]_{\text{clusters}}}$,

where the dimensional Minkowski functionals $M_\nu(r)$ have been given in Eq. 4.3 and the decomposition described in Eq. 4.7 has been used[¶]. Instead of $\overline{A}(r)$ and $\overline{P}(r)$, which for large r are dominated by the area (πr^2) and perimeter ($2\pi r$) of a single disc, we use dimensionless $\overline{A}^*(r)$ and $\overline{P}^*(r)$ instead, which are defined similarly to the dimensionless Minkowski functionals given [Eq. 4.8]

- $\overline{A}^*(r) = \frac{[M_0^*(r)]_{\text{clusters}}}{[M_2^*(r)]_{\text{clusters}}} = \frac{\overline{A}(r)}{\pi r^2}$,
- $\overline{P}^*(r) = \frac{[M_1^*(r)]_{\text{clusters}}}{[M_2^*(r)]_{\text{clusters}}} = \frac{\overline{P}(r)}{2\pi r}$.

When we calculate these quantities from the experimental data of our clustering patterns we obtain Fig. 4.6.

Lets us first look at the limits of these functionals, namely at $r \ll R$ or $r \gg R$. When $r \ll R$, none of the particles (disc) touch each other so that N disconnected particles are expected. Then, the functionals become

$$\begin{aligned} \overline{A}^*(r)\big|_{r\ll R} &\approx \frac{\frac{N\pi r^2}{N\pi r^2}}{\frac{N}{N}} = 1, \\ \overline{P}^*(r)\big|_{r\ll R} &\approx \frac{\frac{N2\pi r}{N2\pi r}}{\frac{N}{N}} = 1, \\ \overline{S}(r)\big|_{r\ll R} &\approx \frac{N^2(2\pi r)^2}{4\pi N\pi r^2 N} = 1, \end{aligned} \tag{4.9}$$

[¶]Mathematically, when moving from the strict (dimensional or dimensionless) Minkowski functionals $M_\nu(r)$ [Eq. 4.3] and $M_\nu^*(r)$ [Eq. 4.8] to the $[M_0(r)]_{\text{clusters}}$, $[M_0^*(r)]_{\text{clusters}}$, $\overline{A}^*(r)$, $\overline{P}^*(r)$, and $\overline{S}(r)$ we loose an important property, namely that of additivity: If we calculate the Minkowski functionals of the union of two arbitrary domains $A \cup B$, the Minkowski functionals can be decomposed as $M_\nu(A \cup B) = M_\nu(A) + M_\nu(B) - M_\nu(A \cap B)$. The gain is however that the latter introduced quantities have a more direct physical interpretation.

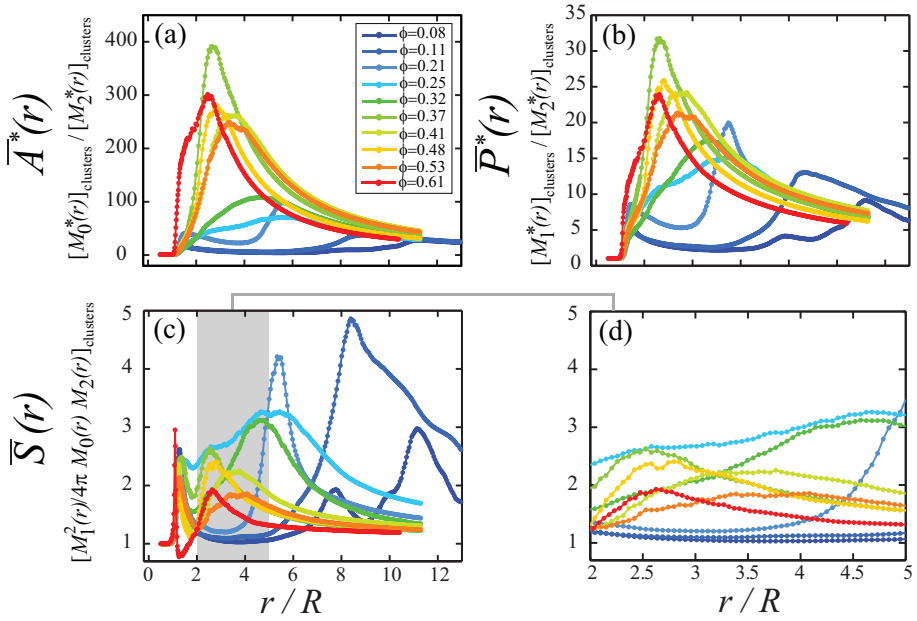

Figure 4.6: Morphological characterization of the clustering patterns from antinode clusters (low ϕ) to node clusters (high ϕ) as a function of r normalized by the floater radius R. (a) Average cluster area $\overline{A}^*(r)$, (b) average cluster perimeter $\overline{P}^*(r)$, and (c) average aspect ratio $\overline{S}(r)$. (d) The shaded region of the average aspect ratio plot (c) is enlarged. The interpretation of these plots is discussed in the main text.

where N is the number of floaters. In Fig. 4.6, all experimental data satisfy this limit when $r \ll R$, i.e all are equal to one. Secondly, let us consider the other limit, $r \gg R$. There, all disconnected groups are expected to merge, and to become a single cluster. Moreover, if r becomes substantially larger than the distances between the individual particles, this final cluster will converge to a disc of radius r [‖] and the functionals

[‖] Note that we are evaluating the Minkowski functionals in an unbounded two-dimensional space, i.e., without boundaries (see Fig. 4.3). We allow the spheres to grow indefinitely in 2D space.

become

$$\begin{aligned} \overline{A}^*(r)\big|_{r\gg R} &\approx \frac{\frac{\pi r^2}{N\pi r^2}}{\frac{1}{N}} = 1, \\ \overline{P}^*(r)\big|_{r\gg R} &\approx \frac{\frac{2\pi r}{N2\pi r}}{\frac{1}{N}} = 1, \\ \overline{S}(r)\big|_{r\gg R} &\approx \frac{(2\pi r)^2}{4\pi^2 r^2} = 1. \end{aligned} \tag{4.10}$$

Similar to the previous case, here, all experimental data indeed converge towards one when $r \gg R$ so that the limit is satisfied [see Fig. 4.6].

Between these two distinct limits, all functionals have several maxima at different r/R. The first peaks in cluster area [Fig. 4.6(a)] and cluster perimeter [Fig. 4.6(b)] correspond to the event that individual particles merge into clusters, at a radius slightly larger than R, depending on how packed the structures are. The heights of the peaks, $\overline{A}^*_{\max}$ and $\overline{P}^*_{\max}$, respectively, give the typical size of the clusters. The corresponding $r_{\max}$ where the peaks occur provides the average distance between the particles in the cluster, and therefore constitute a measure for the size of the porous region in between the particles of the cluster. For two values of ϕ, we observe secondary peaks at a higher value of r. These peaks correspond to individual antinode clusters merging into larger structures that extend on the scale of the wavelength of the standing Faraday wave.

In Fig. 4.6(c), we plot the third quantity we derived from the Minkowski functionals, namely the average aspect ratio $\overline{S}(r)$. The very first peaks, located at $r \approx R$, presumably correspond to touching particles merging into clusters of two or three, which generates large aspect ratios and should be disregarded. The location of the first peaks we find for $r > R$ [grey shaded area in Fig. 4.6(c)] corresponds reasonably well to the ones in $\overline{A}^*(r)$ and $\overline{P}^*(r)$. The corresponding heights $\overline{S}_{\max}$ provide the average aspect ratio of the main clusters in the pattern.

In Fig. 4.6(d), the grey shaded area of Fig. 4.6(c), is magnified to show the aspect ratio in this area of interest in greater detail: For the three lowest values of ϕ, corresponding to the antinode clusters, we hardly find a hint of a maximum and the average aspect ratio is approximately equal to one. This stands to reason, since these antinode clusters are circular in shape and therefore hardly lead to any increase of the aspect ratio. That is to say, until above a certain value of r the antinode clusters themselves start to merge, an effect that is clearly visible in the $\phi = 0.25$ curve in Fig. 4.6(d). For intermediate ϕ there is a clear and high maximum in the average aspect ratio for small $r/R \approx 2-3$ that corresponds to the formation of filamentary

clusters. Finally, for the highest values of ϕ the aspect ratio goes down again, which is connected to the formation of the grid-shaped node clusters.

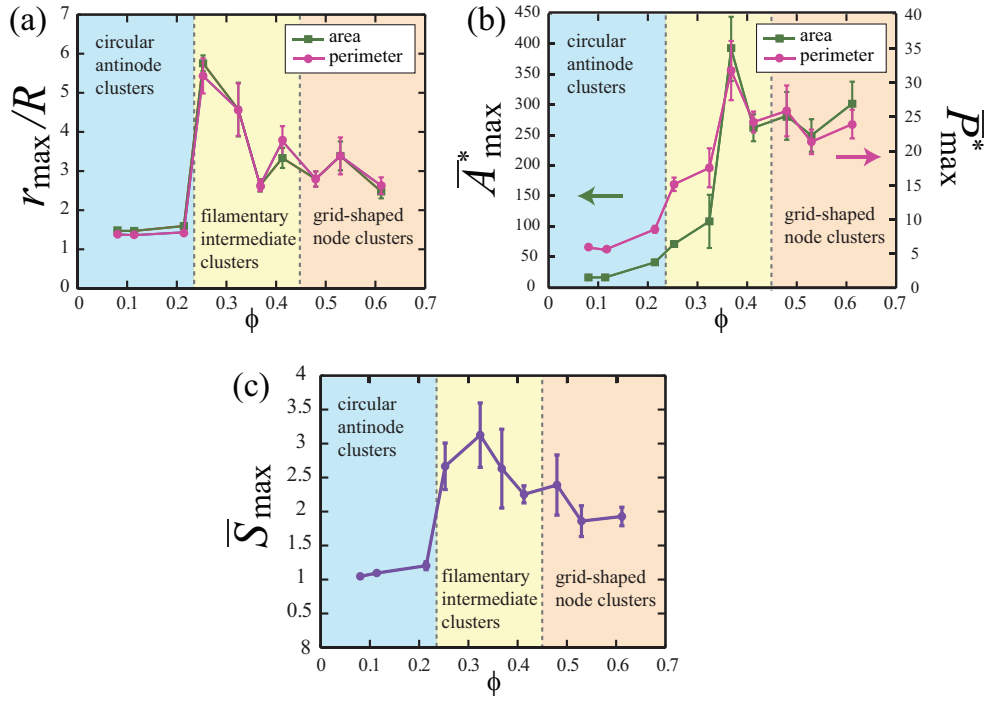

Figure 4.7: Quantification of the morphological properties of the experimentally observed clustering patterns as a function of ϕ, using the location and height of the maxima in Fig. 4.6. (a) The location r_{max}/R of the (first) maximum in the plots of $\overline{A}^*(r)$ [green squares] and $\overline{P}^*(r)$ [pink circles] versus ϕ. (b) The height $\overline{A}^*_{max}$ [green squares] and $\overline{P}^*_{max}$ [pink circles] of the (first) maximum in the plots of $\overline{A}^*(r)$ (left vertical axis) and $\overline{P}^*(r)$ (right vertical axis) again versus ϕ. (c) The height of $\overline{S}_{max}$ of the maximum in the gray shaded area of the plot of the aspect ratio $\overline{S}(r)$ versus ϕ. The interpretation of these plots is discussed in the main text. (The mean values of each ϕ are the overall time averages of the experimental data. The error bars are the standard deviations of the time averages obtained by using a subset of a quarter of the data from the corresponding mean value.)

In Fig. 4.7(a), we plot the location r_{max} of the first maximum of both $\overline{A}^*(r)$ and $\overline{P}^*(r)$ as a function of ϕ. Since the two curves agree excellently with each other, we conclude that the average cluster area and perimeter reach their extreme values for the same r for each ϕ, which is plausible. Clearly, for low ϕ, r_{max} lies close to the particle radius R, indicating that neighboring particles in this antinode cluster

regime are relatively close to one another in all spatial directions. At the boundary of the intermediate regime, the location of the maximum shifts quite suddenly to $r \approx 6R$ as an indication of the formation of loose filamentary structures with holes in the order of 10 particle radii. When ϕ increases even further, the location of the maximum shifts back to lower values of r, because the system as a whole is becoming denser, and consequently the holes in between structures necessarily become smaller again. From the corresponding maxima themselves [Fig. 4.7(b)] a similar picture emerges. For the antinode clusters (small ϕ), the average cluster size is small, and in the intermediate region rises quite steeply to an approximately constant large value, which it keeps inside the node cluster region (large ϕ).

Finally, in Fig. 4.7(c), we plot the maximum value of the average aspect ratio $\overline{S}_{\max}$ in the grey area of Fig. 4.6(c). For low ϕ, there is no maximum value and $\overline{S}(r) \approx 1$ throughout the shaded region, but then a finite maximum $\overline{S}_{\max} \approx 3$ suddenly appears for $\phi = 0.25$, as evidence of the formation of structures that are elongated rather than circular. For higher ϕ, the maximum $\overline{S}_{\max}$ gradually decreases again and becomes approximately equal to 2 in the grid-shaped node clusters.

In conclusion, the global analysis performed in this Section gives us an extensive characterization of the experimentally observed clustering patterns as a function of ϕ. In Chapter 3, the clustering patterns has been also examined by introducing the global correlation coefficient $c(\phi)$, which nicely separate the antinode (low ϕ) and the node (high ϕ) clusters as a function of ϕ with a broad intermediate transition region. In agreement with $c(\phi)$, the intermediate transition region suggested by the global analysis lies in the same region as the one indicated by $c(\phi)$. [The global analysis suggests a slightly larger intermediate transition region.] In addition to what we could learn from $c(\phi)$, we can now also understand the detailed morphology of the clusters. Even though the Minkowski point pattern analysis developed in this Section mainly aims to quantifying the clustering patterns globally, local information can also deduced from the derived quantities such as $r_{\max}$ as was discussed above [Fig. 4.7(a)]. In the following Section, we will analyze the clustering patterns locally.

4.4 Local analysis

In the previous section, the experimentally observed floater patterns have been quantified globally by the Minkowski functional point pattern approach. We have shown that the morphological identities of the clustering patterns at various ϕ are successfully determined by that method. There, the clusters have been evaluated in a global picture, taking the full two-dimensional structure of the patterns into account. We now aim to complement this global analysis with a local counterpart in which we characterize the packing and the local ordering within the clusters at different ϕ. To this end, we apply two methods, namely the local bond orientational order parameter and the pair correlation function which both are frequently used in the context of soft condensed matter [32–37].

4.4.1 Local bond orientational order parameter

The local bond orientational order parameter Ψ_6 provides a measure of to what extent a certain packing of particles is different from the hexagonal packing, and is defined as [32–34]

$$\Psi_{6,j} = \frac{1}{N_{nn}} \sum_{k=1}^{N_{nn}} \exp 6i\,\theta_{jk}. \tag{4.11}$$

This is an expression for the jth particle. Here, N_{nn} is the total number of its (first) nearest neighbors and θ_{jk} is the angle between the bond joining the particles j and k and a reference axis which is kept fixed for each term in the summation. Here, the x-axis is chosen as a reference axis [32]. The absolute value of the complex number $\Psi_{6,j}$, i.e $|\Psi_{6,j}|$, varies between 0 and 1. $|\Psi_{6,j}| = 1$ when the particle is locally in a hexagonal pattern, i.e., $\theta_{jk} = \vartheta + \pi/3\,n$ for each j-th and k-th particle combination, integer n and constant ϑ. For each particle in the experimental snapshot patterns of Figs. 4.1(a-f), the quantity $|\Psi_{6,j}|$ is visualized by gray-scale images [32] in Figs. 4.8(a-f).

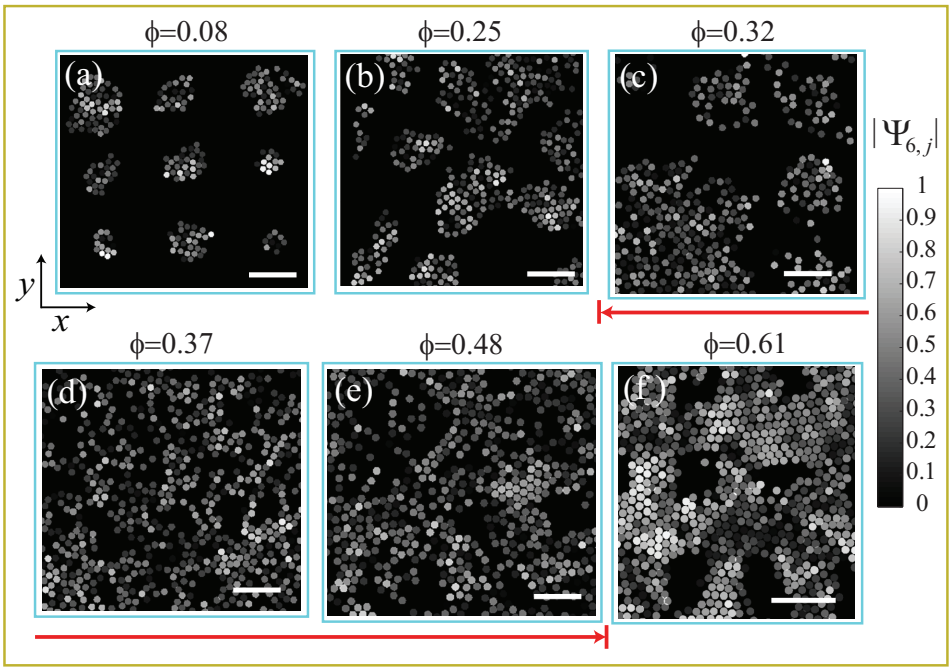

Figure 4.8: The variation in the absolute value of the local bond orientational order parameter $|\Psi_{6,j}|$ of each particle in the experimental snapshots of Fig. 4.1. Each disc, drawn with the average floater radius, represents a floater. (The floaters used in the experiment have a polydispersity of approximately 14%.) The particles are colored according to their $|\Psi_{6,j}|$-value, i.e., when $|\Psi_{6,j}|$ is maximum (1) the corresponding disc is white, whereas the disc is black when $|\Psi_{6,j}|$ is minimum (0). The whiter colors at high ϕ indicate more local ordering (d-e). More specially, the lighter regions at the highest ϕ are due to the hexagonal arrays clearly seen in (f). The bars indicate a length scale of 5 mm.

To quantify the local structure of the clusters, in addition to $|\Psi_6|$, i.e., the local bond orientational order averaged over all particle, further quantities can be valuable such as the (first) nearest neighbor distances averaged over all particles and the number of the nearest neighbors N_{nn} again averaged over all particles. These quantities are plotted as a function of ϕ for all the experimental data (and also time averaged over many experimental frames) in Figs. 4.9(a-c), respectively. Remarkably, these local quantities also mark the three regions, i.e., ordered antinode clusters at low ϕ, loosely packed intermediate clusters at intermediate ϕ, and highly ordered grid-shaped node clusters at high ϕ. However, there are hardly any changes in the local parameters at intermediate ϕ, making these local quantities less suited. In the characterization of the transition from the antinode clusters at low ϕ to the nodal clusters at high ϕ, than the global analysis presented in the previous Section.

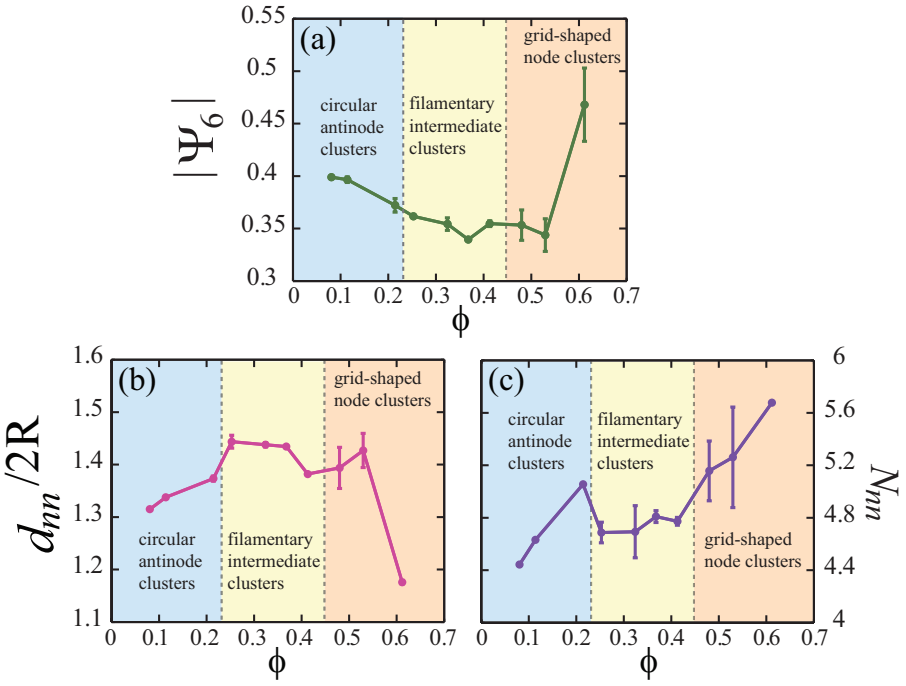

Figure 4.9: Characterizing the local order in floater patterns as a function of ϕ. We plot (a) the absolute value of the local bond orientational order parameter $|\Psi_6|$, (b) the (first) nearest neighbor distances d_{nn} normalized by the floater diameter $2R$, and the number of the (first) nearest neighbors N_{nn} (c), all as function of ϕ. All three quantities are averaged over all particles in the field of view and over time. The time average is performed over 200 wave period ($\approx 200 \times 0.05$ s$= 10$ s) for each ϕ. (The mean values of each ϕ are the overall time averages of the experimental data. The error bars are the standard deviations of the time averages obtained by using a subset of a quarter of the data from the corresponding mean value.)

$|\Psi_6|$ indicates that the ordering decreases for filamentary structures at intermediate ϕ relative to the compact circular antinodes at low ϕ. Beyond a certain ϕ, the ordering starts to increase again due to highly ordered clusters forming at the nodal lines [Fig. 4.9(c)]. Both Figs. 4.9(b,c) show the opposite behavior: d_{nn} and N_{nn} show a slightly increasing trend when moving from low ϕ to the loosely packed filamentary structures at intermediate ϕ. Since the node clusters are packed in a more organized way than irregularly packed antinode clusters due to the breathing (see breathing antinode clusters and non-breathing node clusters in Chapter 3), d_{nn} is smaller and N_{nn} is larger at high ϕ than their values at low ϕ.

Finally, we examine how these local parameters relate to the wave structure. In Chapter 3, we have introduced the global correlation coefficient c which quantifies to what extent the position of the particle patterns is correlated with the wave amplitude maxima, which constitutes another global quantity to evaluate the clustering. In analogy with the above, we now introduce c_{local} which quantifies to what extent the local bond orientational order parameter of the particles is correlated with the amplitude maxima of the wave,

$$c_{local} = \frac{<\mid \Psi_6(\vec{r},t) \mid a(\vec{r}) >_{\vec{r},t}}{<\mid \Psi_6(\vec{r},t) \mid >_{\vec{r},t}}. \tag{4.12}$$

Here, $a(\vec{r})$ are the functions $a_{cos}(\vec{r})$ and $a_{step}(\vec{r})$ introduced in Chapter 3, which are 1 in the antinode region and -1 around the nodal part of the wave. Note that $<\mid \Psi_6(\vec{r},t) \mid >_{\vec{r},t}$ is simply the average value of the absolute local bond orientational order parameter also plotted in Fig. 4.9(a). The resultant $c_{local}(\phi)$ is shown in Fig. 4.10. In contrast to $c(\phi)$, there is no monotonic decrease from the antinode clusters at Region I (low ϕ) to the node clusters at Region III (high ϕ).

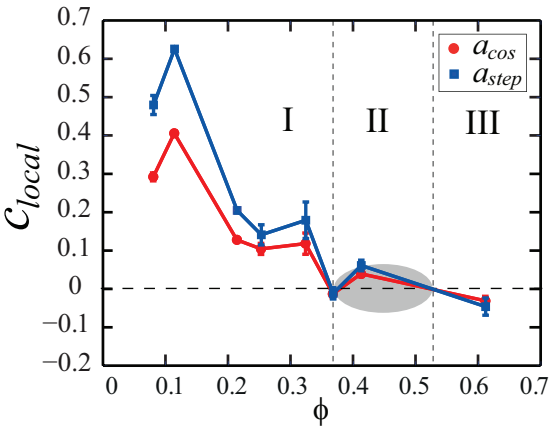

Figure 4.10: Correlation of the local bond orientational order parameter and the standing wave amplitude maxima as a function of ϕ. The correlation $c_{local}(\phi)$ is calculated for both a_{cos} (red circles) and for a_{step} (blue squares). The shaded area indicates the transition region suggested by the global correlation coefficient $c(\phi)$ as was presented in Fig. 3.4 in the previous Chapter. (The mean values of each ϕ are the overall time averages of the experimental data. The error bars are the standard deviations of the time averages obtained by using a subset of a quarter of the data from the corresponding mean value.)

4.4.2 Pair correlation function

The last quantity we discuss in this Chapter is the pair correlation function, which is one of the fundamental quantities to characterize the spatial distribution of the particles, and is frequently used in modeling of particulate systems, i.e., simulations of hard spheres [35, 36] and soft spheres [36, 37]. It is a probabilistic quantity in the sense that it provides the likelihood of finding two particles at a distance r apart. The pair correlation function $g(r)$ in two-dimension is defined as follows

$$g(r) = \frac{1}{N 2\pi r \rho} \sum_{\substack{i=1 \\ i \neq j}}^{N} \sum_{j=1}^{N} \delta(r - \mid \vec{r}_i - \vec{r}_j \mid). \tag{4.13}$$

Here N is the total number of floaters in the system and ρ is the density of floaters, i.e., $\rho = N/\mathrm{A}_T$ with A_T the total area of interest. Practically, to calculate $g(r)$, for every reference particle j, a circle with a radius r is drawn around it. Then, the number of particles i with center in a shell of infinitesimal thickness dr around this circle is counted. Finally, the counting procedure is repeated for all particles j in the system. The calculated $g(r)$ for the experimental data of the clustering patterns is shown for various ϕ in Fig. 4.11(a1-f1), corresponding to the experimentally observed floater patterns of Fig. 4.1(a-f).

In Fig. 4.11(a1-f1) we plot the short range behavior of $g(r)$, where we resolve the particle length scale R. The general trend we find is that, as ϕ increases, $g(r)$ develops more and sharper peaks, corresponding to the development of the more ordered grid-shaped node clusters at the highest ϕ. In addition, in Fig. 4.11(a2, d2, and f2), we plot $g(r)$** on the scale of the wavelength of the standing Faraday wave. For the lowest value, $\phi = 0.08$, we clearly observe correlations of particles in a certain antinode cluster with particles in the neighboring antinode clusters [Fig. 4.11(a2)]. These correlations are lost completely when the heterogeneous filamentary structures develop at the intermediate value of $\phi = 0.37$ [Fig. 4.11(d2)]. Although hardly discernible in Fig. 4.11(f2), for the highest $\phi = 0.61$ where the grid-shaped node clusters develop, there is a slight modulation in $g(r)$ corresponding to the open spots around the antinodes of the standing wave pattern.

**The linear decrease of $g(r)$ in Fig. 4.11(a2, d2, and f2) is a finite size effect caused by the fact that there are fewer particles to be found within the system boundaries as r increases. Here, we did not disregard the finite size effect [38] since we will be only interested in examining the peaks rather than the exact shape of $g(r)$. When one determines the exact $g(r)$ dealing with the boundary effect, $g(r) = 1$ at $r \gg R$ if no structure occurs (i.e., for a uniform distribution of particles) [1].

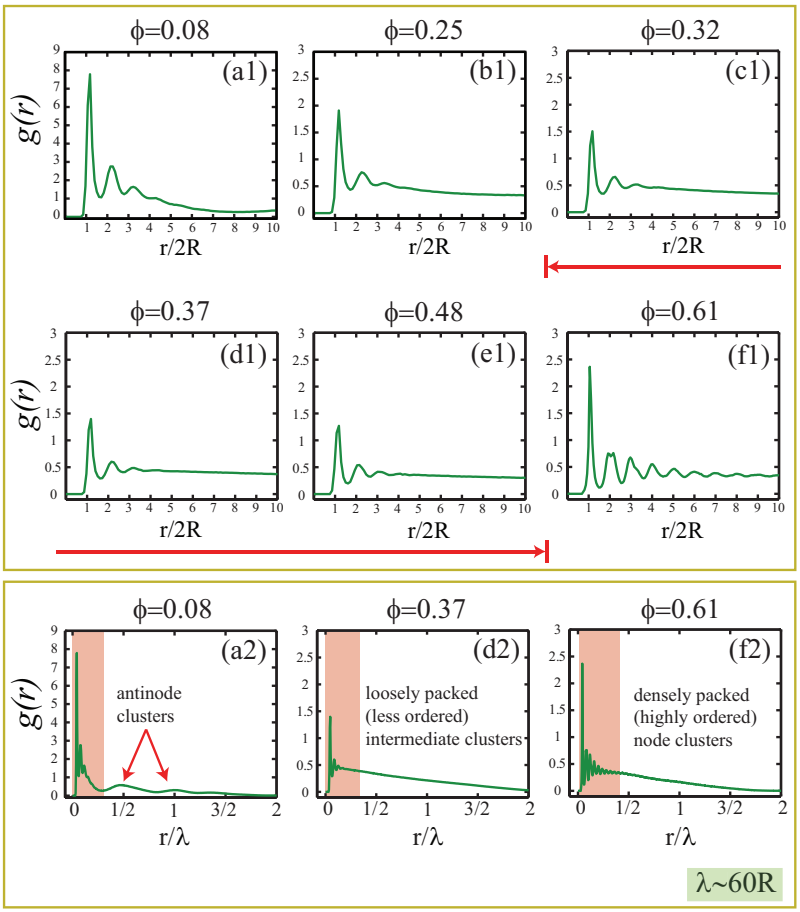

Figure 4.11: Pair correlation functions of the floater patterns from antinode clusters (low ϕ) to node clusters (high ϕ). Both the short range ($r < 20R$) and the long range ($r < 120R$) behavior of $g(r)$ are given. The time average is performed over 200 wave periods ($\approx 200 \times 0.05 = 10$ s) for each ϕ. (a1-f1) The short range behavior of $g(r)$. The red line indicates the intermediate clustering patterns in the transition region. There is a dramatic increase in number of peaks in $g(r)$ at the highest ϕ (f1) which suggests highly ordered structures. (a2-f2) For three values of ϕ, we also provide the long range behavior of $g(r)$. The shaded red rectangles indicate the regions corresponding to those already introduced in (a1-f1). Note that $\lambda \approx 60R$. For the lowest value of $\phi = 0.08$, we find that $g(r)$ nicely detects neighboring antinode clusters when $r = n\lambda/2$ with integer n (a2). At intermediate $\phi = 0.37$ (d2), no large scale correlations can be observed, whereas for the highest $\phi = 0.61$ (f2) there is a hardly visible, tiny variation for $r = n\lambda/2$ connected to the grid-shaped node clusters. The linear decrease of $g(r)$ is a finite size effect caused by the fact that there are fewer particles to be found within the system boundaries as r increases.

We can further analyze the general trend discussed above by examining the peaks in $g(r)$ in some more detail. To this end, we subtract the linearly decreasing average density from the plots in Fig. 4.11 and determine the magnitude of the peaks and valleys. As presented in a semi-logarithmic plot in Fig. 4.12(a), the peak heights of $g(r)$ can be nicely matched to an exponential fit if one neglects the tails*.

The slope of the fits for various ϕ can be used as a measure of the amount of long-range order in the system. If the peak heights decay quickly, i.e., the absolute value $|\alpha|$ of the slope α is large, there is little order. However, when the decay is smooth such that a smaller $|\alpha|$ occurs, the system is highly ordered. We plot $|\alpha|$ as a function of ϕ in Fig. 4.12(b). We find that $|\alpha|$ remains approximately constant throughout the regimes of the circular antinode clusters and the filamentary intermediate clusters and only decreases rapidly when the grid-shaped node clusters form.

Another way of examining the amount of order in the structure is to count the number of peaks above a certain threshold. We perform this as follows: For each peak the ratio of its height and the height of the second peak in the $g(r)$ we are examining is calculated. If this ratio is larger than a chosen threshold, the peak is counted. Otherwise, the corresponding peak is disregarded. To check the sensitivity of the chosen threshold, several thresholds such as 1%, 5%, 10%, and 20% are applied. The results of this procedure [Fig. 4.12(c)] are consistent with the previous method: The number of peaks remains approximately constant for low and intermediate ϕ and only increases rapidly in the region where the grid-shaped node clusters form.

One may wonder why there is so little order in terms of $g(r)$ in the low ϕ regime, where the antinode clusters are observed, as they also seem quite regular in structure. This is because of two reasons: The first is that the clusters are limited in size to a few particle diameters, which is in the order of the capillary length L_c††. This obviously limits the number of peaks that can be present in $g(r)$. The second reason is the breathing motion that is observed for these antinode clusters (see Chapter 3), which will tend to smear out structures in the pair correlation function‡‡.

*$g(r)$ can be approximated to an exponential in classical fluids. Further details can be found in Ref. [1]

††As defined before, the capillary length L_c equals $L_c = \sqrt{\sigma/\rho_l g}$. Here, σ is the surface tension coefficient of the interface, ρ_l is the liquid density, and g is the acceleration of the gravity. In our case (at a lab temperature of about 20 °C), a water-air interface, $L_c = 2.7$ mm, which is $\sim 4.5R$.

‡‡Although the analysis is done stroboscopically (taking those times for which the surface is flat), the breathing effect will still influence the interparticle distance.

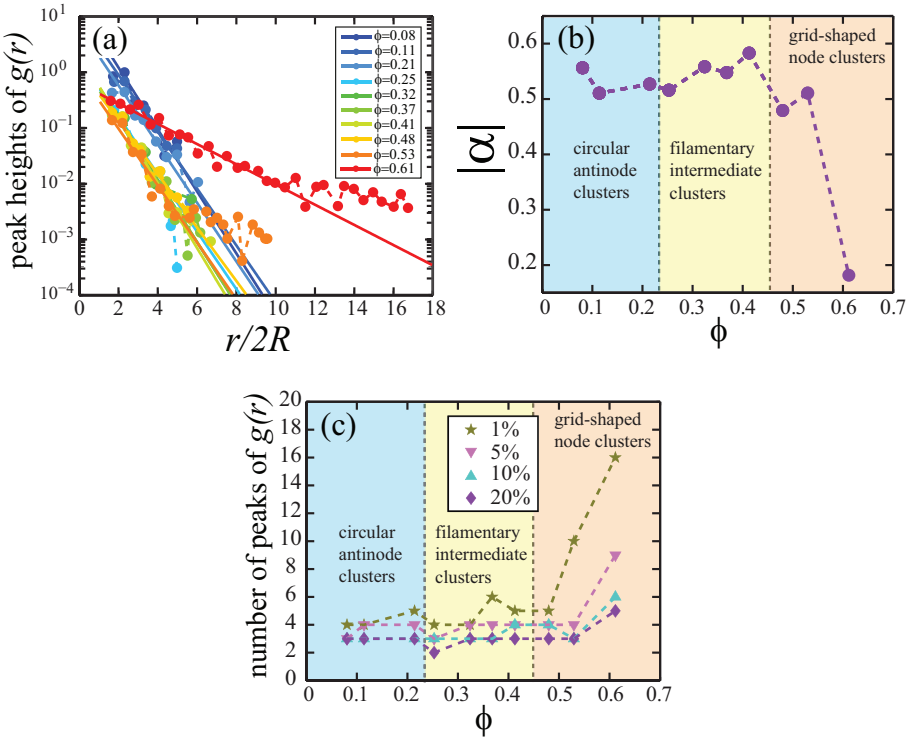

Figure 4.12: The analysis of the peaks and valleys in $g(r)$. (a) The exponential decay of the peak heights of $g(r)$ as a function of $r/2R$ shown in a semi-logarithmic plot for several values of ϕ. (b) Absolute value $|\alpha|$ of the slope α of the exponential fits in (a), plotted as a function of ϕ. (c) Number of peaks in $g(r)$ that are above a certain threshold again as a function of ϕ. We used four different thresholds, namely 1%, 5%, 10%, and 20% of the height of the second peak in $g(r)$.

4.5 Conclusion

We have characterized the morphology of the experimentally observed clusters as a function of the floater concentration ϕ from the antinode clusters to the node cluster regime. In a global picture, cluster area, perimeter, and aspect ratio are quantified utilizing the Minkowski functional point pattern approach. The results show the large variety of floater patterns generated as a result of the competition between the attractive capillary force and the drift due to the standing wave (See Chapter 2). On this large scale, we can distinguish three regions: circular antinode clusters (low ϕ), filamentary and more heterogenous clusters (intermediate ϕ), and grid-shaped node clusters (high ϕ). This richness in the clustering patterns explains the broad transitional region between the antinode and node clusters, and why it is difficult to pinpoint the transition at a single ϕ. In the energy argument of Chapter 3, only hexagonally symmetric patterns were designed without considering the rich morphological details of the structures that form at intermediate ϕ. However, in this Chapter, we successfully characterize these details. In future work, one could improve the energy argument of the previous Chapter by incorporating these details.

Furthermore, in this Chapter we have locally characterized the clustering from the antinode clusters (low ϕ) to the node clusters (high ϕ) in a local picture. In Chapter 3, we discussed the breathing effect, the oscillating interfloater distance in the experimentally observed antinode clusters within a wave period. In contrast, nearly constant floater distance was observed in the node clusters. Moreover, again in Chapter 3, we discussed the breathing has an important influence on the energy results since the breathing causes a huge energy penalty in the antinode region at high ϕ. (Consequently, the node clusters are energetically more favorable at high ϕ.) This encourages us, in this Chapter, to ask how the clustering locally varies from the antinode to the node regime. To this end, several local quantities connected to the floater packing such as the absolute value of the local bond orientational order parameter $|\Psi_6|$, the floater distance between the nearest neighbors d_{nn}, and the number of the nearest neighbors N_{nn} have been determined.

In comparison with the regimes determined by the global analysis, i.e., circular antinode clusters, filamentary intermediate clusters, and grid-shaped node clusters, we show that N_{nn} successfully confirms the existence of these regimes. Even though the general behavior of $|\Psi_6|$ and d_{nn} is consistent with the previously identified regimes, we find that there are no sharp differences between filamentary intermediate clusters and grid-shaped node clusters, except for the highest ϕ. All local quantities are consistent with the breathing effect introduced in Chapter 3 and discussed

above if one compares the quantities at low ϕ to those at high ϕ: Both the antinode and node clusters present more ordered structures relative to the intermediate clusters. However, due to the breathing, the antinode clusters are more irregularly packed* so that $\mid \Psi_6 \mid$ is considerably higher for node clusters. In addition, lower d_{nn} and higher N_{nn} for the node clusters also support that more regularly packed structures evolve at grid-shaped node clusters.

Finally, the clusters are analyzed using the pair correlation function. The attractive capillary interaction is expected to become more important for increasing ϕ and therefore is likely to induce long-range order at high ϕ. To this end, we examine the peaks of $g(r)$ in more detail. Both the peak heights and the number of peaks are quantified as a function of ϕ. The results of the peak height successfully indicate the regions where we observe ordered structures, i.e., where long-range order is expected, namely the densely packed node clusters, and the regions where the correlation length is expected to be shorter, namely the loosely packed intermediate clusters and also the antinode clusters, which are packed irregularly due to the breathing effect. Counting the number of peaks in $g(r)$ agrees with the above observation. The dramatic increase in the number of peaks at high ϕ indicates increasing long-range order. The plateau region at the intermediate ϕ is significant and resembles the global correlation coefficient introduced in Chapter 3, which also gives the broad intermediate plateau. Both imply that a detailed global picture is required to determine the variations in shape of the intermediate clusters such as the Minkowski functional point pattern approach.

In conclusion, this Chapter is devoted to developing a detailed methodology to characterize the complex floater patterns we observed in the experiment. We found that for a full characterization of the patterns, both global (Minkowski) and local [packing, $g(r)$ analysis] is indispensable. We believe that the methods developed here can be applicable to other physical, chemical, and biological systems that exhibit pattern formation, in order to learn more about common large scale motion observed in particulate flow, and so to examine to what degree there is universality in these large scale behaviors.

In the following Chapter, *Dense heterogenous flow*, we utilize the Minkowski point pattern method discussed here to characterize the collective motion of the densely packed cohesive grains.

*In the analysis presented in this Chapter, the quantities are given after performing time averages. If one considers a dynamical analysis, the breathing effect can be seen more strongly in these local quantities as we did in Chapter 3 for the lowest and highest ϕ, i.e., see Fig. 3.3 for further details.

References

[1] D. Chandler, *Introduction to Modern Statistical Mechanics*, (Oxford University Press, Inc. , New York) (1987).

[2] K. E. Bassler and R. K. P. Zia, "Phase Transitions in a Driven Lattice Gas at Two Temperatures", J. Stat. Phys. **80**, 499–515 (1995).

[3] I. S. Aranson, D. Volfson, and L. S. Tsimring, "Swirling motion in a system of vibrated elongated particles", Phys. Rev. E **75**, 051301-1–9 (2007).

[4] V. Narayan, N. Menon, and S. Ramaswamy, "Nonequilibrium steady states in a vibrated-rod monolayer: tetratic, nematic, and smectic correlations", J. Stat. Mech. **P01005**, 1–17 (2006).

[5] J. M. N. T. Gray and K. Hutter, "Pattern formation in granular avalanches", Continuum Mech. Thermodyn. **9**, 341–345 (1997).

[6] I. S. Aranson and L. S. Tsimring, "Patterns and collective behavior in granular media: Theoretical concepts", Rev. Mod. Phys. **78**, 641–692 (2006).

[7] A. J. Koch and H. Meinhardt, "Biological pattern formation: from basic mechanisms to complex structures", Rev. Mod. Phys. **66**, 1481–1507 (1994).

[8] E. Karsenti, "Self-organization in cell biology: a brief history", Nature Rev. Mol. Cell Biol. **9**, 255–262 (2008).

[9] M. Aldana, V. Dossetti, C. Huepe, V. M. Kenkre, and H. Larralde, "Phase Transitions in Systems of Self-Propelled Agents and Related Network Models", Phys. Rev. Lett. **98**, 095702-1–4 (2007).

[10] D. Grossman, I. S. Aranson, and E. Ben Jacob, "Emergence of agent swarm migration and vortex formation through inelastic collisions", New J. Phys. **10**, 023036-1–11 (2008).

[11] D. Helbing, "Traffic and related self-driven many-particle systems", Rev. Mod. Phys. **73**, 1067–1141 (2001).

[12] S. Douady, "Experimental study of the Faraday instability", J. Fluid Mech. **221**, 383–408 (1990).

[13] T. B. Benjamin and F. Ursell, "The stability of the plane free surface of

a liquid in vertical periodic motion", Proc. R. Soc. Lond. A **225**, 505–515 (1954).

[14] K. Kumar and L. S. Tuckerman, "Parametric instability of the interface between two fluids", J. Fluid Mech. **279**, 49–68 (1994).

[15] B. J. Gluckman, C. B. Arnold, and J. P. Gollub, "Statistical studies of chaotic wave patterns", Phys. Rev. E **51**, 1128–1147 (1995).

[16] D. Binks and W. van de Water, "Nonlinear Pattern Formation of Faraday Waves", Phys. Rev. Lett. **78**, 4043–4046 (1997).

[17] W. Zhang and J. Viñals, "Square patterns and quasipatterns in weakly damped Faraday waves", Phys. Rev. E **53**, R4283–R4286 (1996).

[18] A. Kudrolli, M. C. Abraham, and J. P. Gollub, "Scarred patterns in surface waves", Phys. Rev. E **63**, 026208-1–8 (2001).

[19] G. Falkovich, A. Weinberg, P. Denissenko, and S. Lukaschuk, "Floater clustering in a standing wave", Nature (London) **435**, 1045–1046 (2005).

[20] P. Denissenko, G. Falkovich, and S. Lukaschuk, "How waves affect the distribution of particles that float on a liquid surface", Phys. Rev. Lett. **97**, 244501-1–4 (2006).

[21] S. Lukaschuk, P. Denissenko, and G. Falkovich, "Nodal patterns of floaters in surface waves", Eur. Phys. J. Special Topics **145**, 125–136 (2007).

[22] C. Sanlı, D. Lohse, and D. van der Meer, "From antinode clusters to node clusters: The concentration dependent transition of foaters on a standing Faraday wave", arXiv:1202.0051v1 1–5 (2012).

[23] K. R. Mecke, T. Buchert, H. Wagner, "Robust morphological measures for large-scale structure in the Universe", Astron. Astrophys. **288**, 697–704 (1994).

[24] K. R. Mecke, "Morphological characterization of patterns in reaction-diffusion systems", Phys. Rev. E **53**, 4794–4800 (1996).

[25] K. R. Mecke and V. Sofonea, "Morphology of spinodal decomposition", Phys. Rev. E **56**, R3761–R3764 (1997).

[26] H. Mantz, K. Jacobs, and K. Mecke, "Utilizing Minkowski functionals for image analysis: a marching square algorithm", J. Stat. Mech. **P12015**, 1–29 (2008).

[27] E. Calzavarini, M. Kerscher, D. Lohse, and F. Toschi, "Dimensionality and morphology of particle and bubble clusters in turbulent flow", J. Fluid Mech. **607**, 13–24 (2008).

[28] J. Bleibel, A. Domínguez, M. Oettel, and S. Dietrich, "Collective dynamics of colloids at fluid interfaces", Eur. Phys. J. E **34**, 125-1–12 (2011).

[29] K. R. Mecke, "Additivity, Convexity, and Beyond: Applications of Minkowski Functionals in Statistical Physics", Lecture Notes in Physics (Springer) **554**, 111-184 (2000).

[30] K. Michielsen and H. De Raedt, "Integral-geometry morphological image analysis", Phys. Rep. **347**, 461–538 (2001).

[31] K. R. Mecke and D. Stoyan, "Morphological Characterization of Point Patterns", Biometrical Journal **47**, 473-488 (2005).

[32] K. Chen, M. L. Manning, P. J. Yunker, W. G. Ellenbroek, Z. Zhang, A. J. Liu, and A. G. Yodh, "Measurement of Correlations between Low-Frequency Vibrational Modes and Particle Rearrangements in Quasi-Two-Dimensional Colloidal Glasses", Phys. Rev. Lett. **107**, 108301-1–5 (2011).

[33] Y. L. Wu, D. Derks, A. van Blaaderen, and A. Imhof, "Melting and crystallization of colloidal hard-sphere suspensions under shear", PNAS **106**, 10564–10569 (2009).

[34] K. S. Kim, J. Neu, and G. Oster, "Curvature-Mediated Interactions Between Membrane Proteins", Biophysical Journal **75**, 2274–2291 (1998).

[35] A. Donev, S. Torquato, and F. H. Stillinger, "Pair correlation function characteristics of nearly jammed disordered and ordered hard-sphere packings", Phys. Rev. E **71**, 011105-1–14 (2005).

[36] L. E. Silbert, D. Ertaş, G. S. Grest, T. C. Halsey, and D. Levine, "Geometry of frictionless and frictional sphere packings", Phys. Rev. E **65**, 031304-1–6 (2002).

[37] L. E. Silbert, A. J. Liu, and S. R. Nagel, "Structural signatures of the unjamming transition at zero temperature", Phys. Rev E **73**, 041304-1–8 (2006).

[38] See "http://www.physics.emory.edu/ weeks/idl/gofr2.html" to learn an alternative method to disregard the finite size effect in experimental data suggested by J. C. Crocker and E. R. Weeks.

5

Dense heterogenous flow of cohesive floaters on capillary ripples *

When macroscopic spheres with attractive capillary interactions float on capillary ripples in the dense limit, the flow is composed of floater domains, i.e., small floater groups initially moving together, breaking up in a certain way some time later. This process repeats itself continuously. During the break-up process, the initial floater group morphologically deforms. In addition, the formation of such groups shows heterogeneity in space and irregularity in time. We study the effect of the floater concentration on the deformation and the heterogeneity of the floater groups. We characterize the floater groups and the resultant heterogenous dynamics in two ways, namely morphologically and through the four-point dynamic susceptibility. We show that our suggested morphological characterization of the floater groups is a valuable alternative representation of the dynamical heterogeneities, which up to now have mainly been quantified by the four-point dynamic susceptibility in the literature.

*Ceyda Sanlı, Kuniyasu Saitoh, Stefan Luding, and Devaraj van der Meer, "Dense heterogenous flow of cohesive floaters on capillary ripples: A comparative study on morphological and conventional approaches to understand dynamical heterogeneities" (in preparation).

5.1 Introduction

Dynamical heterogeneity is a concept developed to understand and characterize the microscopic fluctuations of a macroscopic system when it undergoes a phase transition. "Dynamic heterogeneity refers to the existence of transient spatial fluctuations in the local dynamical behavior," as stated by Ludovic Berthier in his brief paper [1] which summarizes a decade of understanding of dynamic heterogeneity and the four-point correlation function developed by him and his co-workers [2–6]. He continues: "Dynamical heterogeneity, spatiotemporal fluctuations in local dynamical behavior, may explain the statistical mechanics of amorphous solids that are mechanically rigid but have a disordered structure". This statement reflects why physicists are interested in dynamic heterogeneity in particulate systems such as molecular, colloidal, and granular glasses [1]. Let us give some examples to explain where we observe such transient spatiotemporal fluctuations locally and why this concept is important for macroscopic spheres floating on capillary ripples.

Colloids are reported to exhibit cooperative motion when they approach the glass-transition [6–9]. There, the fast mobile particles localize, form groups, and the group size increases right before and the beyond the glass-transition to up to 4-5 particle radii [7]. The temporal fluctuations in the particle mobility are characterized by the dynamic susceptibility [7], which typically presents a non-monotonic time dependence (due to the transient temporal fluctuations) with a peak centered at the structure relaxation time [3]. The height of this peak is defined by the volume (area) within which the correlated motion takes place [3]. Basically, the height is proportional to the number of particles participating in the heterogeneous dynamics so that it provides a measure for the amount of the heterogeneity. It has been shown that both the relaxation time of the binary colloidal glass and the volume contributing to the correlated motion increase towards the glass transition [7].

Similar to the above observations, a comparative study between hard and soft sphere colloidal glasses show that collective motion, particle rearrangements, and, as a consequence, the peak height of the susceptibility, increase for both types of colloidal glasses when the systems approach the glass transition [8]. However, soft sphere colloidal glasses demonstrate more heterogenous dynamics than the hard ones. In these soft sphere glasses, an extremely long-range correlation up to a hundred particle diameters is observed [8]. Internal elasticity of the dense suspension is stated to be the reason of such correlated long-range displacements. Dynamical heterogeneity in aging colloidal glasses of Laponite is studied by both microrheology and macroscopic rheology [9]. Decoupling between translational and orientational

degrees of freedom, i.e., between translational and rotational relaxation times, is observed, and is suggested to be the origin of the heterogeneities.

In addition to colloidal glasses, the systematic study of the dynamic heterogeneity and the dynamic susceptibility are performed in dense granular systems approaching the jamming transition [10–14]. The granular systems, which up to now have been employed to examine the heterogeneities (at least the studies we are aware of), are bidisperse dense metallic millimeter-size cylinders under cyclic shear [10], air-driven steel macroscopic spheres [11, 12], and horizontally vibrated bidisperse granular hard disks [13, 14]. When approaching the jamming point, all these systems present an increasing number of collective events, i.e., localized mobile particles, particle rearrangements, and varieties of other local events with transient temporal behavior. As a consequence, they display increasing heterogeneities in space and irregularities in time. Just as in the colloidal glasses, the dynamical susceptibility near the jamming point in all these cases gives long relaxation times and a large amount of volume (area) where the correlated motion takes place.

To analyze these type of systems, instead of considering the mobility of single particles [11, 12], a correlation of the mobility of pairs of particles is introduced which is called the four-point correlation function. It measures the correlation in dynamics between any two points in space at two different times [10, 13]. In this way, divergence in the correlation length close to the jamming point is demonstrated [10, 13, 14]. (The same four-point correlation function is also applied to determine the range of the correlation in hard and soft spheres colloidal glasses [8] mentioned above.) Moreover, the divergence in the correlation length close to the jamming point is also captured by a dynamical morphology analysis, i.e., using average mobile cluster and string sizes [11]. Furthermore, a dynamical Voronoi analysis is suggested to quantify the heterogeneities. It gives consistent results with the dynamic susceptibility [12].

How do these time-dependent local events occur in other particulate systems such as a coarsening foam? Dynamical heterogeneities of a coarsening dry foam have been examined using the dynamic susceptibility [15], and agree with the above observations reported in colloidal glasses and granular systems. All these systems have in common an increasing amount of spatiotemporal collective events close to the glass and jamming transitions. They are however governed by totally different interactions (see Fig. 5.1 left panel), e.g., the attractive van der Waals depletion forces or the repulsive electrostatic interactions in colloidal glasses or frictional repulsive interactions in driven granulars. The success of the concept of dynamic heterogeneity with its systematic tools, such as the dynamic susceptibility and the four-point

correlation function, and the morphology analysis of the mobile beads is reflected by the robust measurements close to the phase transitions in this large variety of particulate systems. This brings us to the main question to be answered in this Chapter: How do the cohesive macroscopic spheres floating on capillary ripples behave in the dense limit and how can we analyze their spatiotemporal motion? And, as a secondary question, would it be possible to develop tools that, better than, e.g., the dynamic susceptibility and the four-point correlation function are capable of distinguishing morphological and dynamical structures further away from the jamming point.

In our experimental system, millimeter size hydrophilic spheres are subject to the attractive capillary forces as introduced in Section 2.2.3 in Chapter 2 and driven by erratic forces due to capillary Faraday waves of very small wave length. In Section 5.2, we will introduce the system and the experimental setup. To answer the question whether we will observe spatial heterogeneities with transient fluctuations when the floater concentration ϕ increases is our main interest in this Chapter. As many of the other systems discussed above, our system (see Fig. 5.1 middle panel) is also accessible to perform a local analysis during a long time with a good resolution in both space and time. Therefore, to characterize the dynamical heterogeneities, we analyze the dynamic susceptibility in Section 5.3 and suggest a morphological analysis in Section 5.4.

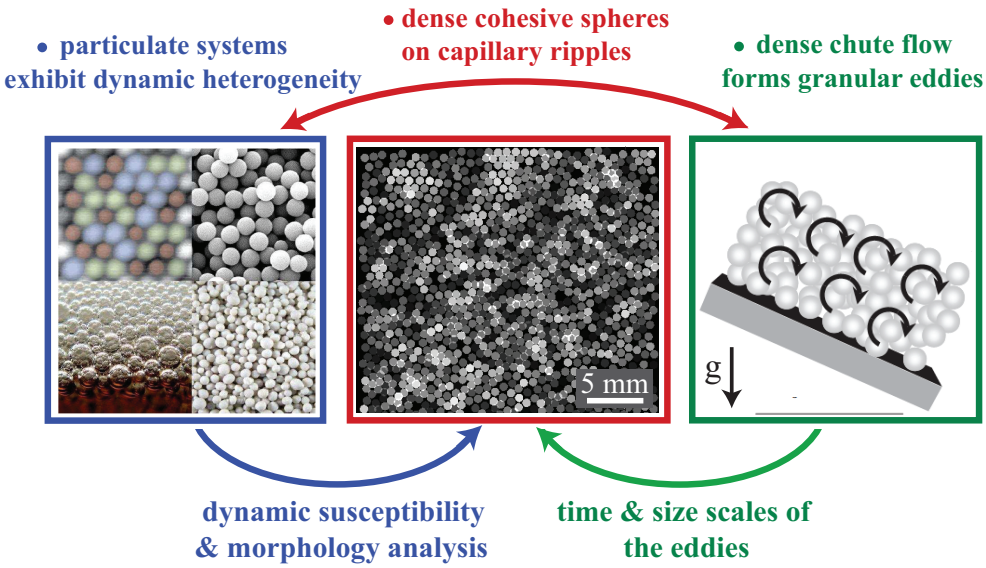

Figure 5.1: A schematic, connecting our system of dense cohesive spheres on capillary ripples with the ideas and methods already developed in the literature. Left panel: Particulate systems, (top left) a nanometer size alloy, (top right) micron size colloids, (bottom left) a submillimeter size beer foam, and (bottom right) millimeter size granular matter, all exhibit dynamical heterogeneity characterized by the dynamic susceptibility and morphological analysis. Picture taken from Ref. [6]. Middle panel: Disordered packing configuration of millimeter size spheres floating on capillary Faraday waves. The gray scale varies from the least hexagonally packed spheres (black) to the most hexagonally packed spheres (white). Right panel: A scenario of granular eddy formation in dense chute flow. An analytical study of typical time and size scales of these structures encourages us to determine these scales in our system, too. Picture is taken from Ref. [16]. Obviously, this system is much further away from the jamming point than those in the left panel.

Besides giving potential contributions to enrich the scheme of dynamical heterogeneities close to jamming, our system would also be valuable to connect to the granular eddies or clusters as argued in granular chute flows [16, 17] (see also Fig. 5.1 right panel). In this system, which is obviously much further from the jamming point, due to the inelastic collisions in the inclined dense grains, the possibility of granular eddy formation is reported and typical time and size scales of the granular eddies are calculated.[†]

In this Chapter, we will experimentally show that the flow is composed of floater domains: Small floater groups initially moving together, break up in a certain way some time later. By extending the technique we have developed in Chapter 4, i.e., utilizing the Minkowski functionals, we will quantify the morphology of the break-up process in Section 5.4. By means of this morphology analysis, we will show that it is possible to determine typical time and size scales of the floater clusters of Refs.[16, 17], i.e., for the granular clusters in dense chute flow. Finally, the methodology and the results will give us a chance to compare the results from the dynamic susceptibility with those of the dynamical morphology. Such a comparative study has also been considered before with different morphology methods, namely the size of groups of mobile beads [11] and dynamical Voronoi analysis [12]. In Section 5.5, we will summarize the results and discuss the agreements and the disagreements.

[†]The connection between the granular eddies and the eddies formed in turbulent flows is still an open issue.

5.2 Experiment

A schematic illustration of the experimental setup is shown in Fig. 5.2. The setup is the same as the one that was already introduced in Chapter 3 with some modifications. Let us briefly summarize the setup and describe these modifications. A rectangular container [Fig. 5.2(a)] is attached to a shaker. The container is completely filled with purified water (Millipore water with a resistivity > 18 MΩ·cm) such that the water level is perfectly matched with the container edge as shown in Fig. 5.2(g) to create the brim-full boundary condition [18]. Spherical polystyrene floaters, contact angle[‡] 74° and density 1050 kg/m^3, with an average radius R of 0.31 mm and a polydispersity of approximately 14% are carefully distributed over the water surface to make a monolayer of floaters. To avoid any surfactant effects, both the container and the floaters are cleaned by performing the cleaning protocol as described in Ref. [19].

A capillary Faraday wave is generated using a shaker which provides a vertical sinusoidal oscillation such that the vertical position of the container varies as a function of time t as $a_0 \sin(2\pi f_0 t)$, where f_0 is the shaking frequency and a_0 is the shaking amplitude. Here, both a_0 and f_0 are fixed to 0.1 mm and 250 Hz, respectively. These combinations are chosen to create capillary ripples on the water surface with a wavelength in the range of the floater diameter (≈ 0.62 mm).

A continuous white fiber light source (Schott) is used to illuminate the floaters from far away as shown in Fig. 5.2(b). As a consequence, white spots at the edge of the floaters are obtained as shown in Fig. 5.2(e). This has the advantage that we are able to detect all floaters in the dense regime as presented in Fig. 5.2(f). The positions of the floaters are recorded with a high-speed camera (Photron Fastcam SA.1) at 60-500 frames per second. The lens (Carl Zeiss 60mm) is adjusted such that it focuses on the floaters at the non-deformed water surface. Here, we use the capillary Faraday waves to agitate the dense floaters so that there is no macroscopic apparent amplitude observed. The wave amplitude is always considerably smaller than the floater radius (≈ 0.31 mm).

[‡]The contact angle is measured using the static balance discussed in Chapter 2. See Section 2.2.1 for further details.

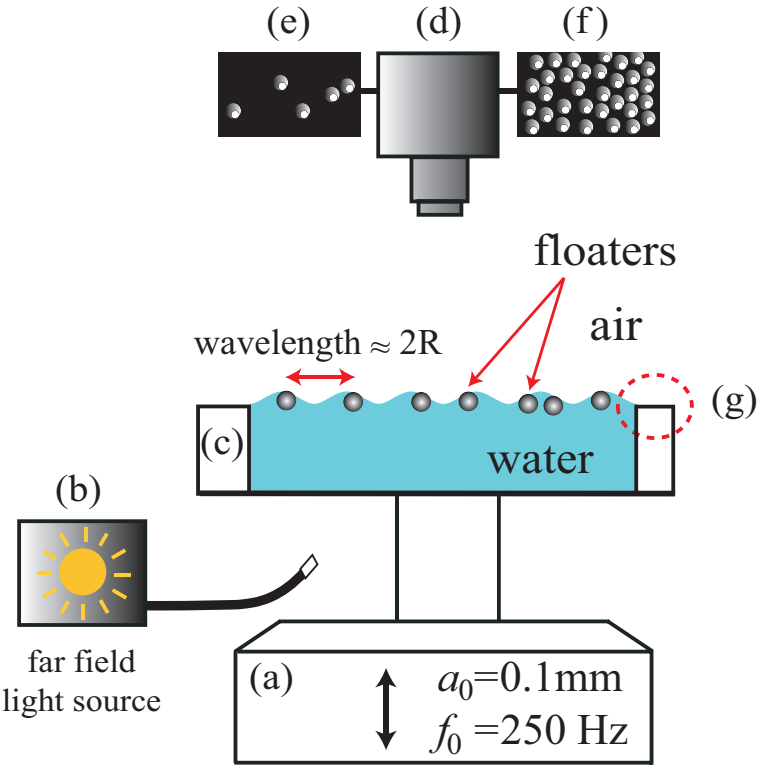

Figure 5.2: Experimental setup: (a) Shaker. All experiments are performed at fixed driving amplitude [0.1 mm] and frequency [250 Hz]. (b) Far field light source generated by a Schott fiber light source. (c) Transparent hydrophilic glass container, (d) high speed camera (Photron Fastcam SA.1), (e-f) illustrations of a camera image for dilute (e) and dense (f) floater concentrations. The advantage of using far field light source is clear, i.e., all particles can be detected using the white spots in the images.

The resultant capillary ripples on the water surface are shown in Fig. 5.3, left panel. The container, made from transparent hydrophilic glass with 10 mm height, has a 81×45 mm^2 rectangular cross section as shown in Fig. 5.3(a). To eliminate the boundary effects due to the sharp corners of the container, an elliptic rim made from plastic (red ellipse) is used. Each image taken with the high speed camera is 512 pixels × 640 pixels (36×28 mm^2) as shown by the yellow rectangle (size ratios are preserved). The horizontal field of view is 35% of the total area of the ellipse.

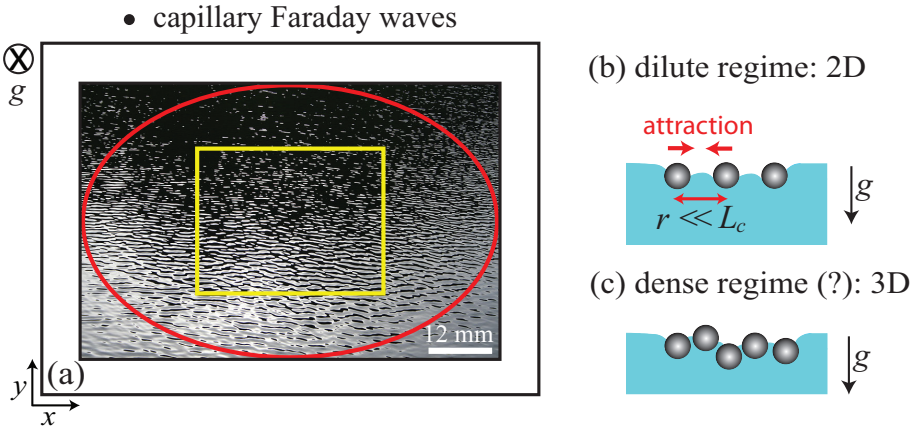

Figure 5.3: Left panel: Top view of an illustration of capillary ripples generated by Faraday waves. (a) Hydrophilic glass container with a rectangular cross section 81×45 mm^2. In addition to the pinned brim-full boundary condition [as was introduced in Fig. 5.2(g)], an elliptic (red) plastic boundary is created to eliminate boundary effects due to the sharp container edges. (c) A rectangular experimental image window (yellow) with area 36×28 mm^2 (35% of the area of the ellipse) represents the horizontal field of view, and is fixed for all experiments. Right panel: Schematic illustrations of our hydrophilic heavy spherical floaters trapped at a static water-air interface. (b) The floaters configuration in dilute case is represented with the meniscus around the floaters. The figure indicates that we are in two-dimensional space. (c) A scenario for the dense case is sketched and suggests a more three-dimensional situation.

In Fig. 5.3(b,c), static configurations of the floaters at a water-air interface are presented. As described in Fig. 5.3(b) and discussed in detail in Section 2.2.3 in Chapter 2, due to the asymmetric surface deformation around each hydrophilic heavy sphere, there is an attraction between the spheres so that our floaters are cohesive. Even in the dilute case, the distance r between the floaters is much smaller than the capillary length $L_c = \sqrt{\sigma/\rho_l g}$. Here, σ is the surface tension coefficient of the interface, ρ_l is the liquid density, and g is the acceleration of gravity. (For an air-water

interface at 20°C, $L_c = 2.7$ mm.) As presented in Fig. 5.3(b), we have a monolayer of spheres at the interface. In the dilute limit, the static system is therefore two-dimensional. However, in the dense regime, as sketched in Fig. 5.3(c), the spheres may not preserve the monolayer so that the resultant configuration would have three-dimensional aspects. What both situations will look like for driven floaters is not known exactly.

5.2.1 Calculating floater concentration from an experimental image

The control parameter of the experiment is the floater concentration ϕ, which is measured by determining the area fraction covered by the floaters in the area of interest. Here, the area of interest is that of the enclosed yellow rectangle shown in Fig. 5.3(a). However, as mentioned above, we have polydispersity (standard deviation of the size distribution divided by the mean size, i.e., 0.31 mm) equal to 14%. In addition, we cannot determine the exact radius of each floater from our experimental point images. Therefore, calculating ϕ by counting the number of floater is insufficient.

To determine ϕ, we construct a binary (black-white) image of each experimental image. The procedure is illustrated in Fig. 5.4. ϕ is equal to sum of the white area divided by the total image area.

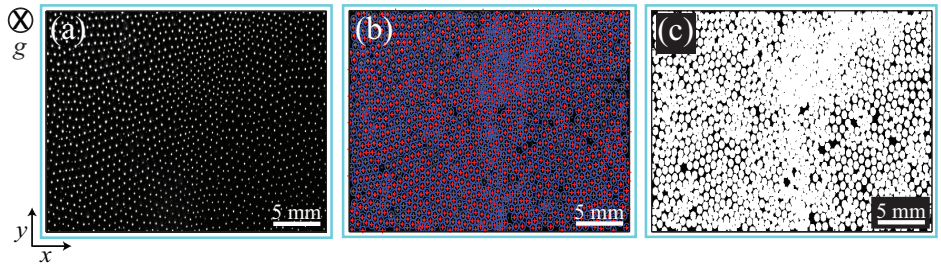

Figure 5.4: Determination of the floater position by assuming a two-dimensional cross section and calculation of the floater concentration ϕ. (a) An experimental image is taken from the top using the high speed camera. Each white spot represents a single floater. (b) The center of each spot is marked with red plus (see Ref. [20] for the numerical code finding the particle centers with the polydispersity). The corresponding boundary of the floater is reconstructed by drawing a blue circle with the average radius $R = 0.31$ mm around each center. Here, we assume that the center of the spot corresponds to the center of the floater. (c) The binary (black-white) image is then constructed by coloring the disk area enclosed by the blue circles to white, leaving the remaining area colored in black. The completely white regions (specially the upper middle part of the resultant binary image) indicate the clustering of the floaters in smaller size than the average floater size. Here, $\phi = 0.71$. The white bars indicate a length scale of 5 mm.

5.3 Dynamic susceptibility

The four-point dynamic susceptibility χ_4 is used to determine to what extend the dynamics of dense granular systems is heterogeneous in space and irregular in time, when they approach the jamming transition [5, 10–13]. The adjective "four-point" here refers to evaluating a correlation in dynamics between any two points in space at two different times. In the literature, χ_4 is defined in several ways.

In the first method described in the literature, the correlation is calculated between two positions of a single floater trajectory which are connected to two different times [11, 12]. In the second method, the correlation is obtained using two different particle trajectories at some distance from each other, at two different times [1, 5, 10]. In a third method, χ_4 is calculated by integrating the four-point correlator, the correlation of the mobilities of two particles a distance apart at two different times, over space [5, 10, 13]. In all three methods, χ_4 is equal to the time average of the spread of the resultant correlation from the ensemble averaged value.

In this Thesis, we restrict ourselves to the first method, i.e., we determine χ_4 by the correlation of single trajectories at two different times. To this end, let us first introduce the instantaneous self-overlap order parameter[§] [12]

$$Q_t(l,\tau) = \frac{1}{N}\sum_{i=1}^{N} \exp\left(-\frac{|\,\vec{r}(t+\tau)-\vec{r}(t)\,|^2}{2l^2}\right), \tag{5.1}$$

where N is the number of floaters tracked, i is the floater index, and so the sum represents the ensemble average of all tracked floaters[¶]. $\vec{r}(t+\tau)$ and $\vec{r}(t)$ are the two-dimensional position of the single floater at time $t+\tau$ and t, respectively[‖]. l is an important quantity, and is a measure for the typical distance over which a single floater can move within time τ. If the floater i travels much less than the distance l, i.e., $|\,\vec{r}(t+\tau)-\vec{r}(t)\,| \ll l$, the exponential term gives 1. On the other hand, if the floater i travels over a distance much larger than l, i.e., $|\,\vec{r}(t+\tau)-\vec{r}(t)\,| \gg l$, the exponential term becomes 0. Therefore, $Q_t(l,\tau)$ expresses the mobility of a single floater; more specifically, it is a measure for its capability of traveling a distance l within a time

[§] In the literature [13], the same quantity is also called the self-intermediate scattering function.

[¶] The MatLab version of the particle tracking program, developed by David Grier, John Crocker, and Eric Weeks, is used in this Thesis. See http://physics.georgetown.edu/matlab/index.html for further details.

[‖] The function in the definition of Eq. 5.1 could be any function that decreases monotonously from 1 to 0 at a length scale l. In Ref. [12], $Q_t(l,\tau)$ is calculated using a step function instead of the Gaussian function we are using in Eq. 5.1 to increase the accuracy of the result. Such a Gaussian was also considered in Ref. [10].

difference τ.

Naturally, at very small τ, for each floater the exponential in Eq. 5.1 evaluates to 1 such that $Q_t(l,\tau) = 1$. In contrast, for very large τ all exponentials are 0, and as a consequence, $Q_t(l,\tau) = 0$. At intermediate τ, we obtain a crossover regime of which the time scale of course depends on the value of l. Fig. 5.5 presents the spread in the self-overlap order parameter $Q(l,\tau)$, which is the time average of the instantaneous counterpart $Q_t(l,\tau)$, e.g., $Q(l,\tau) =< Q_t(l,\tau) >_t$.

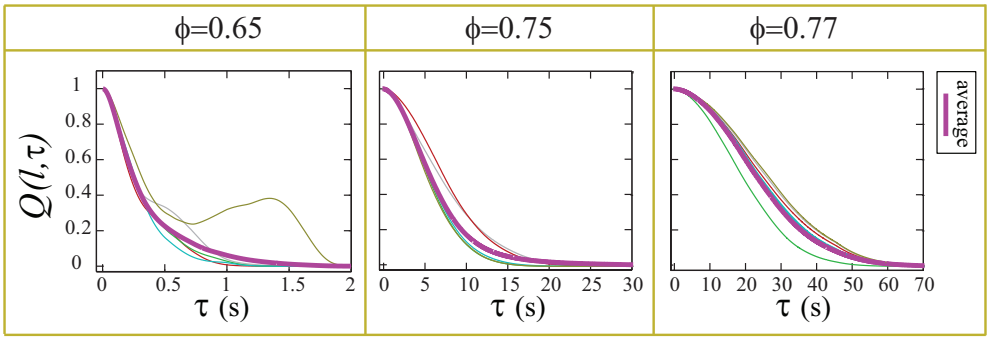

Figure 5.5: Self overlap order parameter $Q(l,\tau)$ as a function of the time difference τ (bold magenta lines), for low, intermediate, and high ϕ [$\phi = 0.65$, $\phi = 0.75$, and $\phi = 0.77$, respectively]. For comparison, the other lines (grey, cyan, green, olive, and red) are the time averages of the same quantity for randomly selected single particles. Here, we have chosen the distance $l = 8R$, with R the floater radius. All curves converge to 1 for early τ and 0 for late τ. The largest deviations from the averages are observed for intermediate τ.

The spread in $Q_t(l,\tau)$ reflects the dynamic heterogeneity, and is measured by the four-point dynamic susceptibility, which is defined as the variance of $Q_t(l,\tau)$

$$\chi_4(l,\tau) = N\big[< Q_t(l,\tau)^2 >_t - < Q_t(l,\tau) >_t^2 \big], \tag{5.2}$$

where $<>_t$ represents the average taken over all times t. For a given value of l, $\chi_4(l,\tau) = 0$ for both very small and very large τ since no spread from $Q(l,\tau)$ is expected. However, at intermediate τ, the increasing amount of spread produces a finite $\chi_4(l,\tau)$. In the next section, we will examine the position and the magnitude of the maximum of $\chi_4(l,\tau)$ for several fixed values of l.

5.3.1 Experimental results for the dynamic susceptibility

In this Subsection, we will examine the self-overlap order parameter $Q(l, \tau)$ and the dynamic susceptibility $\chi_4(l, \tau)$ as a function of the time difference τ for various (fixed) values of l. The results are presented in Figs. 5.6 and 5.7, respectively, for a range of ϕ. Finally, in Fig. 5.8 we will examine the width of the self-overlap order parameter plots, and the location and height of the maximum in the susceptibility.

We first discuss the decay of $Q(l, \tau)$ as a function of τ [Fig. 5.6]. If we concentrate on Fig. 5.6(a), where we chose $l = 2R$, we find that the decay become smoother when ϕ increases. This stands to reason: Since the mobility of individual floaters is more restricted at high ϕ, a longer time difference τ is required to move apart over a distance l. The same observation is made, and for the same reason, in Figs. 5.6(b,c), where $l = 8R$ and $l = 15R$, respectively. Also, if we now compare Figs. 5.6(a-c) for the same ϕ, we observe that the decay becomes smoother going from small l to large l. Again, this is consistent with our expectation, because a longer time difference τ is necessary to decorrelate the mobility for large l.

To quantify the decay time of $Q(l, \tau)$ as a function of both l and ϕ, we examine the position of the half width $w_Q(l, \phi)$ of $Q(l, \tau)$, i.e., the time τ for which $Q(l, \tau) = 1/2$ (the half of the initial value). Before considering $w_Q(l, \phi)$ in detail, let us turn to the dynamic susceptibility $\chi_4(l, \tau)$, which is the variance of $Q(l, \tau)$, defined in Eq. 5.2.

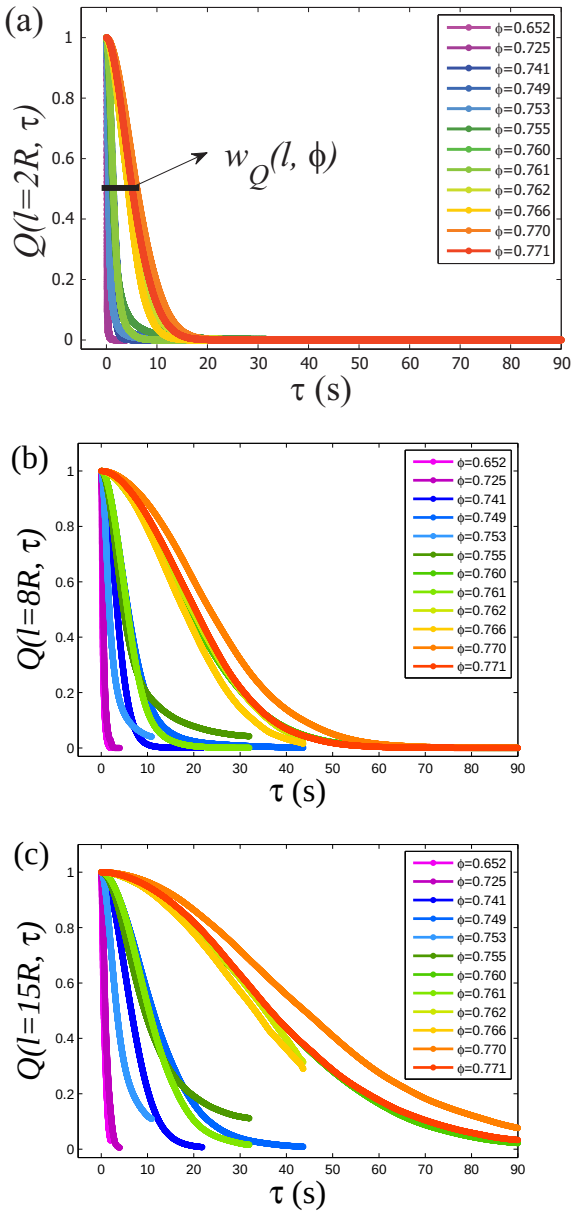

Figure 5.6: The self-order parameter $Q(l,\tau)$ as a function of the time difference τ for various ϕ. The distance l is taken equal to $2R$ (a), $8R$ (b), and $15R$ (c), in which R is the floater radius. The half width of $Q(l,\tau)$, $w_Q(l,\phi)$ is the value of τ for which $Q(l,\tau) = 1/2$. Clearly, as l increases $w_Q(l,\phi)$ increases, because a longer time τ is needed to travel over a distance l.

Fig. 5.7 presents $\chi_4(l,\tau)$ for the same values of l [$2R$, $8R$, and $15R$] and ϕ as were used in the previous Figure. Here, we have similar observations as for Fig. 5.6: First of all, when ϕ increases the maxima shift to larger τ, become wider and less high. The same is true if we fix ϕ and increase l, just as was the case for $Q(l,\tau)$. For the largest value, $l = 15R$, we observe in addition that the curves for the highest ϕ become noisier and less smooth. The origin of this effect is poor statistics: Since our time window is limited, there are relatively few values of t that can accommodate a large time interval τ, such that the time average contains relatively few samples.

For all cases, the peak position $\tau_{\chi_4}(l,\phi)$ indicates when we observe the maximum deviation from the average dynamics. As a consequence, $\tau_{\chi_4}(l,\phi)$ is called the typical time scale of the heterogeneous motion. (In the literature [1, 3], it is also referred to as the relaxation time.) Furthermore, the height of the peak $h_{\chi_4}(l,\phi)$ gives the amount of the floaters that participate in the heterogeneous motion. This height is connected to the area (or volume in three dimensions) within which the correlated motion takes place [1, 3]. Both $\tau_{\chi_4}(l,\phi)$ and $h_{\chi_4}(l,\phi)$ will be quantified afterwards.

The half width $w_Q(l,\phi)$ of $Q(l,\tau)$, the peak position $\tau_{\chi_4}(l,\phi)$, and the height $h_{\chi_4}(l,\phi)$ of the four-point dynamic susceptibility $\chi_4(l,\tau)$ are presented as a function of ϕ in Figs. 5.8(a-c), respectively. Fig. 5.8 presents the two time scales, namely $w_Q(l,\phi)$ [Fig. 5.8(a)] and $\tau_{\chi_4}(l,\phi)$ [Fig. 5.8(b)], that characterize the dynamic heterogeneity exhibited by the dense cohesive grains floating on the capillary ripples, as a function of ϕ. Both time scales qualitatively and quantitatively agree with each other quite well. In general, they increase as a function of ϕ, which indicates that the dynamics slows down. The quite broad range of l [$l = 2R$-$15R$] exhibits almost the same behavior, which shows the robustness of the slowing down of the motion in space.

However, we find that there is no monotonic increase in the time scales when ϕ increases. The trend is anomalously broken at two ϕ values, namely $\phi = 0.753$ and $\phi = 0.761$. There, both time scales are remarkably small relative to the values at the nearby ϕ. We will examine the reason behind this in Section 5.5, the last Subsection of this Chapter.

In Fig. 5.8(c), the heights $h_{\chi_4}(l,\phi)$ of the susceptibility peaks are presented as a function of ϕ. Similar to $w_Q(l,\phi)$ and $\tau_{\chi_4}(l,\phi)$, we find the same trend with ϕ for each of the values of l.

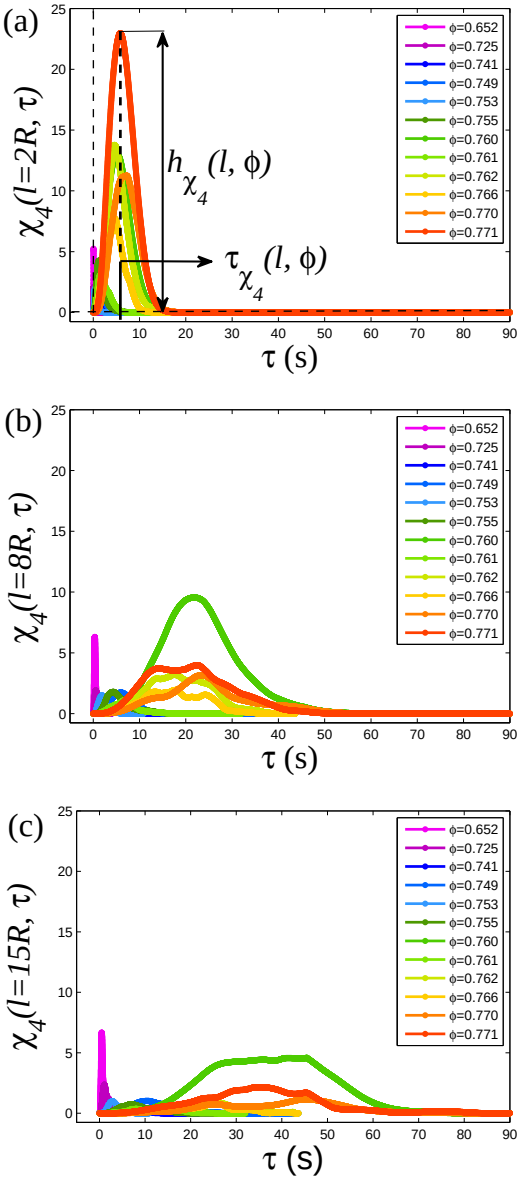

Figure 5.7: The four-point dynamic susceptibility $\chi_4(l, \tau)$ as a function of the time difference τ for various ϕ. The distance l is equal to $2R$ (a), $8R$ (b), and $15R$ (c). The peak position $\tau_{\chi_4}(l, \tau)$ and peak height $h_{\chi_4}(l, \tau)$ characterize the typical time scale of and the amount of floaters contributing to the dynamical heterogeneity.

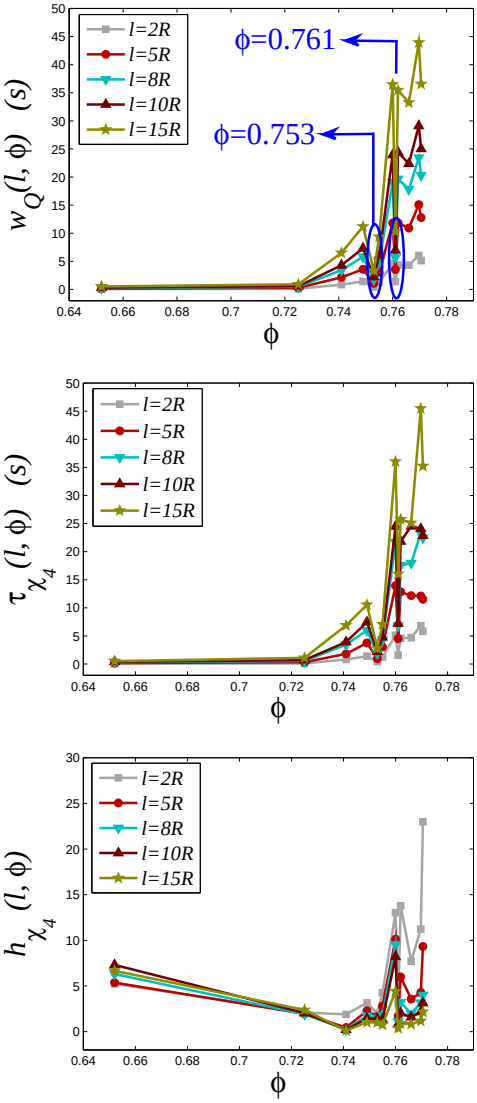

Figure 5.8: The decay width $w_Q(l,\phi)$ of $Q(l,\tau)$ (a), the peak position $\tau_{\chi_4}(l,\phi)$ (b) and the height $h_{\chi_4}(l,\phi)$ (c), both of the dynamic susceptibility $\chi_4(l,\tau)$, as a function of ϕ. For each quantity, the distance l varies from $2R$ to $15R$. The results indicate that l does not change the overall trend when ϕ increases. See main text for further details.

In the literature [5, 10–13], it has been reported that $h_{\chi_4}(l, \phi)$ increases monotonically when the system approaches the jamming point. Here, in addition to anomalies for the same ϕ values mentioned in the context of Figs. 5.8(a,b), we observe that at low ϕ the system exhibit a relatively large amount of heterogeneity compared to intermediate ϕ. This suggests that the dynamic susceptibility analysis may not give a monotonically increasing trend far away from the jamming point.

In the next Section, we develop a different, morphological approach to examine the time scale of the heterogeneities as a function of ϕ. In addition to only calculating the correlations, we will show how the heterogeneous motion of the dense grains cannot only be visualized effectively but also simultaneously with the determination of the quantitative results.

5.4 Visualization and morphology

In this Section, we will develop a new method to quantify the local dynamics of the floaters when the floater concentration ϕ increases. Our method is based on particle tracking, subgroup selection, and subsequently, dynamical morphology analysis in time.

Particle tracking and subgroup selection

First, we track the two-dimensional position of each floater in time. Subsequently, we select subgroups and observe how the particles in the subgroup evolve in time. This procedure is illustrated in Fig. 5.9 for low ϕ [$\phi = 0.65$, Figs. 5.9(I-III)], and high ϕ [$\phi = 0.75$, Figs. 5.9(IV-VI)]. At a certain time $t = 0$, we construct a subgroup of floaters with initial positions, $x(0)$ and $y(0)$, inside a circle with a fixed radius R_{group} [red circles in Figs. 5.9(I,IV)]. Then, we follow the position of the subgroup in time [green disks in Fig. 5.9]. The subgroup undergoes a morphological deformation and the final configuration of the subgroup that we reach [Figs. 5.9(III-VI)] suggests an elongated subgroup rather than the initial compact circular subgroup.

Surprisingly, for both low ϕ and high ϕ, the deformation scheme, i.e., from a circular to a filamentary floater subgroup, turns out to be a quite similar, an observation which is also true for the other ϕ values we investigate. However, the time required to evolve into a filamentary group is much longer (≈ 10 s) at high ϕ than it is at low ϕ (≈ 1.8 s). In addition, at low ϕ, the subgroup breaks into several pieces, whereas the particles at high ϕ tend to remain connected. Consequently, these two remarkable differences, namely the morphological deformation time and the number and shape of the final pieces, will give us a way to characterize the deformation process as a function of ϕ.

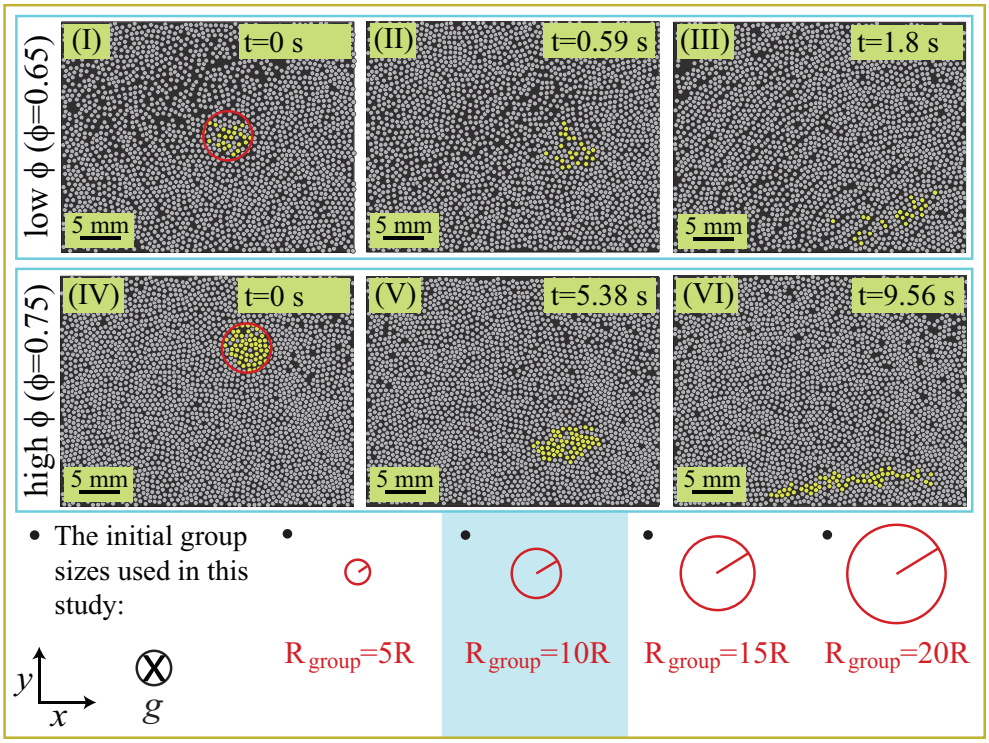

Figure 5.9: Local flow visualization by selecting a circular subgroup and tracking its evaluation in time for a low and a high value of ϕ. Here, each floating sphere on the capillary Faraday wave is represented by a disk with the average floater radius $R \approx 0.31$ mm. The green disks represent the floaters of which the initial positions are inside the red circle with radius R_{group}. (In this example, $R_{\text{group}} = 10R$). The grey disks inside the the red circle are floaters which we cannot track reliably for the complete duration of the experiment; the other grey disks represent the other floaters on the wave surface. The effect of the surface wave is clearly visible if one looks at the position of the gray disks at the entire 2D surface and compares, e.g., (I) and (III). (I-III) The deformation of the initial subgroup (I) at low ϕ [$\phi = 0.65$] is shown at intermediate time (II) and the latest time (III) that we can track. The morphological differences of the subgroup in the different snapshots are clear: From (I) to (III), the circular compact, initial subgroup is evolving into a less compact structure at intermediate time, which is then followed by a stretched, filamentary structure at the final time. (IV-VI) The deformation of the initial subgroup at high ϕ [$\phi = 0.75$]. The circular, compact initial subgroup (IV), evolves into an elongated (V), and finally into a filamentary (VI) floater cluster. The required time to reach the filamentary cluster is remarkably longer at high ϕ [$\approx$ 10 s] than at low ϕ [$\approx$ 1.8 s]. The red disks at the bottom indicate the different initial subgroup sizes (R_{group} varying from $5R$ to $20R$) that will be examined in this Chapter.

Utilizing the Minkowski functionals

In the previous Subsection we have shown how we construct the floater subgroups and track them in time to visualize the dense flow locally. Now, we will explain how one can characterize the morphological differences in the deformation of a single subgroup in time. To this end, we will employ the physical interpretation of the Minkowski functionals that was discussed in Section 4.3.3 of the previous Chapter. There, we showed that when the individual floaters merge into clusters, at a Minkowski radius r_M slightly larger than R, the physical interpretation of the Minkowski functionals, namely area $\overline{A}^*(r_M)$, perimeter $\overline{P}^*(r_M)$, and aspect ratio $\overline{S}(r_M)$ where r_M is the Minkowski radius of the discs which are drawn around each floater center, characterize the shape of the structures.

Before recalling the mathematical form of $\overline{A}^*(r_M)$, $\overline{P}^*(r_M)$, and $\overline{S}(r_M)$, let us first illustrate how we utilize the functionals in the deformation and break-up process. Fig. 5.10 shows schematically a break-up process for $r_M = R$, (a), and $r_M = 2R$, (b). In Fig. 5.10(a), it is not easy to identify the morphological differences between the initial subgroup and the two children subgroups. However, when $r_M = 2R$ in Fig. 5.10(b), where the separated floaters have merged into clusters, the morphological differences between the states before and after the break-up are clear: There is one connected region (cluster) before the break-up and there are two connected regions afterwards. Moreover, the normalized overall cluster area and perimeter** are the smallest in the initial state due to the larger overlapping regions. The normalized area and perimeter are larger in the lower child subgroup and the largest in the upper child subgroup since there the overlapping regions are the smallest relative to those of the initial cluster before the break-up. Furthermore, the aspect ratio is the largest for the filamentary upper child subgroup, slightly less for the elongated lower child subgroup, and close to the minimal value (=1) for the initial, compact circular cluster.

**The overall cluster and perimeter are normalized by the total drawn disc area and perimeter of N disconnected disks, respectively.

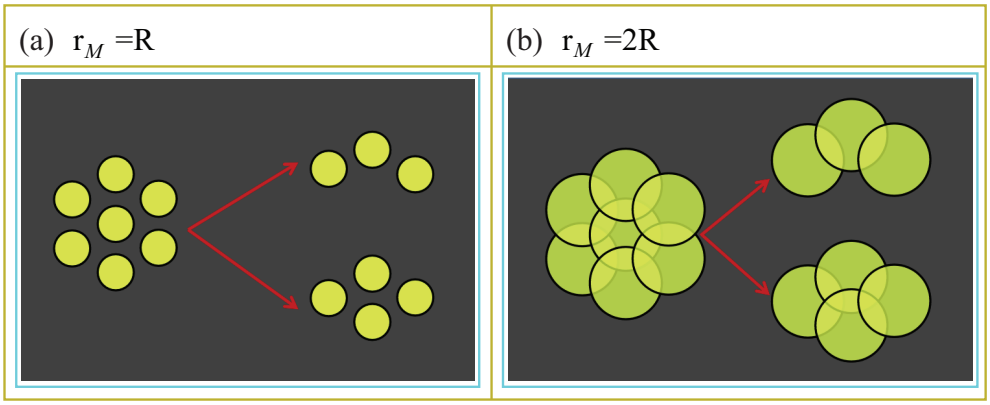

Figure 5.10: A schematic illustration of the break-up process: An initial compact subgroup breaks into two children subgroups when the radius of the discs which are drawn around each floater center is changed from $r_M = R$, (a) to $r_M = 2R$, (b). (a) Since for $r_M = R$ the floaters are separated from each other, it is not easy to characterize a morphological deformation of such a process. (b) For $r_M = 2R$, the individual floaters merge into clusters. By the help of overlapping regions, the morphological deformation in the process can be easily characterized, i.e., one initial cluster gives two children clusters, as a consequence the number of connected regions changes from 1 to 2. If one calculates the area, perimeter, and aspect ratio of the two states, before and after the break-up, they all different due to the different amount and size of the overlapping regions in the resultant two children subgroups relative to the initial subgroup.

We now turn back to the time-dependent deformation of the subgroups of Fig. 5.9, but with $r_M = 2R$ for the floaters which are part of the initial subgroup [i.e., the ones that we can reliably track for the complete duration of the experiment]. The resultant configuration of the floaters, i.e., the resultant clusters that are formed due to merging of individual floaters for this larger value of the Minkowski radius r_M [green disks] are clearly visible in Fig. 5.11.

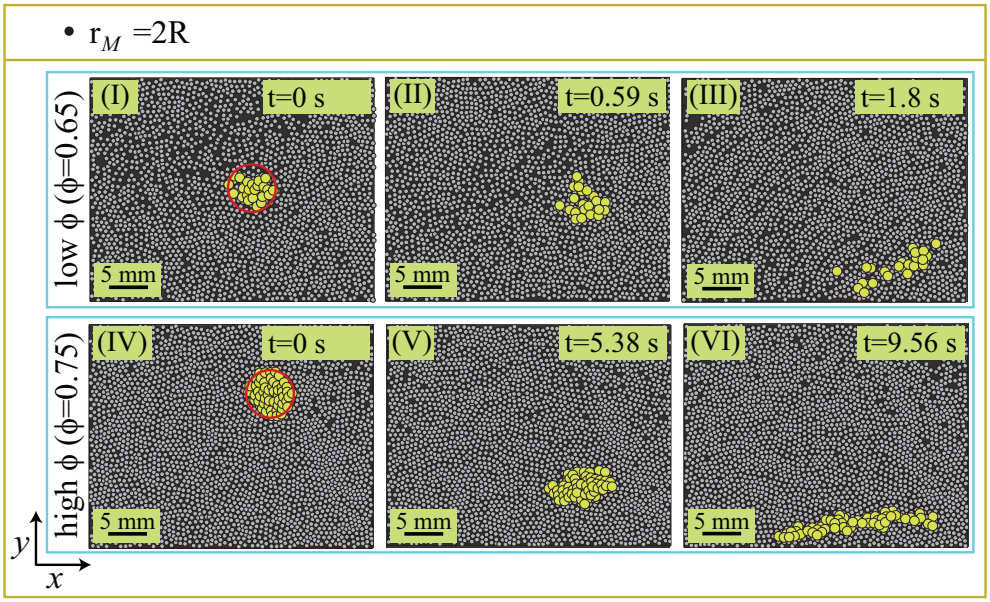

Figure 5.11: Break-up and deformation of an initially round subgroup for low and high ϕ respectively, based on the experimental snapshots. This Figure is identical to Fig. 5.9(I-VI), but here the tracked floater discs [green] are drawn with a Minkowski radius $r_M = 2R$ where R is the average floater radius (≈ 0.31 mm). Since the individual floater discs overlap, floaters have merged into clusters and can be easily distinguished. Consequently, the morphological deformation of these clusters, from the initial compact circular clusters (I,IV), to slightly deformed and elongated clusters (II,V) at moderate time, and then to the final stretched filamentary clusters (III,VI), can be now quantified by calculating the physical Minkowski functionals (see main text).

Let us recall the physical interpretation of the Minkowski functionals, namely area $\overline{A}^*(r)$, perimeter $\overline{P}^*(r)$, and aspect ratio $\overline{S}(r)$

- $\overline{A}^*(r_M) = \frac{[M_0^*(r_M)]_{\text{clusters}}}{[M_2^*(r_M)]_{\text{clusters}}} = \frac{\overline{A}(r_M)}{\pi r_M^2}$,
- $\overline{P}^*(r_M) = \frac{[M_1^*(r_M)]_{\text{clusters}}}{[M_2^*(r_M)]_{\text{clusters}}} = \frac{\overline{P}(r_M)}{2\pi r_M}$,
- $\overline{S}(r_M) = \frac{[M_1^2(r_M)]_{\text{clusters}}}{4\pi [M_0(r_M)]_{\text{clusters}} [M_2(r_M)]_{\text{clusters}}}$.

Here, the normalized Minkowski functionals (marked with asterisk) are related to the original three Minkowski functionals M_0, M_1, and M_2 in two-dimensional unbounded Euclidean space by $M_0^*(r_M) = M_0(r_M)/N\pi r^2$, $M_1^*(r_M) = M_1(r_M)/N 2\pi r_M$, and $M_2^*(r_M) = M_2(r_M)/N$. Here, N is the number of the floaters determined in the subgroups. In the above expressions, the subscript "clusters" in the Minkowski functionals indicates that we disregard the holes in our analysis. This procedure is discussed in detail in Section 4.3 in the previous Chapter.

Finally, in Fig. 5.12 the time evolution of the area $\overline{A}^*(r_M = 2R, t)$, the perimeter $\overline{P}^*(r_M = 2R, t)$, and the aspect ratio $\overline{S}(r_M = 2R, t)$ of the single subgroups selected in Fig. 5.11 are determined at both low ϕ, [$\phi = 0.65$, Fig. 5.12(a,c,e)] and high ϕ [$\phi = 0.75$, Fig. 5.12(b,d,f)].

At low ϕ, the initial floater cluster breaks into more pieces, as a consequence, the Euler characteristics $[M_2^*(r)]_{\text{clusters}}$ increases. Therefore, all morphological quantities $\overline{A}^*$, $\overline{P}^*$, and $\overline{S}$ decay for later times. However, at high ϕ, instead of the break-up process, we observe that the initial cluster evolves to an elongated cluster at intermediate time, and then into a filamentary cluster at the final time. As a result, the aspect ratio and the perimeter will increase with time. Since the area of the elongated and filamentary clusters do not vary much in comparison with the circular initial subgroup, the area at high ϕ increases only very slightly when compared to the perimeter and the aspect ratio at the same ϕ. In the next Section, we will perform this analysis over the entire experimental data range, averaging over many random subgroups in the system, and measure the deformation time.

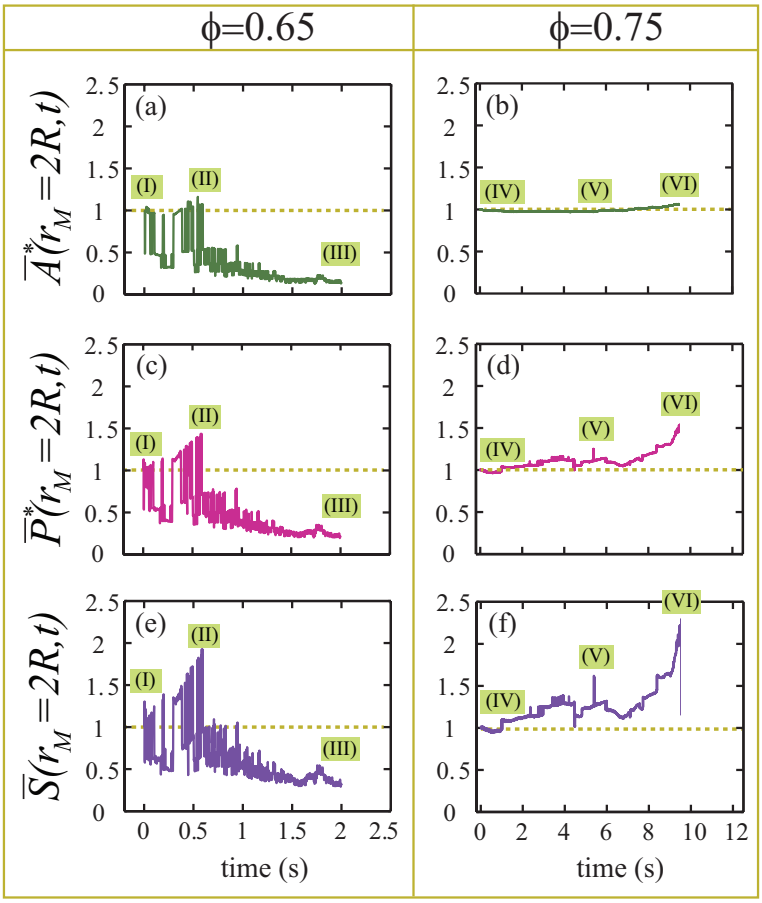

Figure 5.12: The time evolution of the morphological quantities area $\overline{A}^*(r_M = 2R, t)$ [a,b], perimeter $\overline{P}^*(r_M = 2R, t)$ [c,d], and aspect ratio $\overline{S}(r_M = 2R, t)$ [e,f] of the tracked floater clusters at low ϕ [$\phi = 0.65$] and high ϕ [$\phi = 0.75$]. All are normalized by their initial values at $t = 0$. The time values corresponding to the snapshots of the initial subgroups (I,IV), the floater clusters at intermediate time (II,V), and at final time (III,VI) [see Fig. 5.11] are indicated in the plots. The time required to observe noticeable deformations from the initial shape is remarkably shorter at low ϕ (≈ 0.5 s) than at high ϕ (≈ 6 s). In addition, at low ϕ the size of the deformations, specially the area and the perimeter, is larger than they are at high ϕ.

5.4.1 Experimental results of the morphology analysis

Deviations from the average in the deformation process

In this Subsection, we will examine the time-dependent deformation process of the initially constructed subgroups. By applying the methodology that was explained in the previous Subsection, we try to understand the deviations of individual subgroups from the average value. Let us first examine the deformation of the individual floater clusters relative to the corresponding average values, where the averaging was performed over all constructed subgroups (≈ 200 for each ϕ).

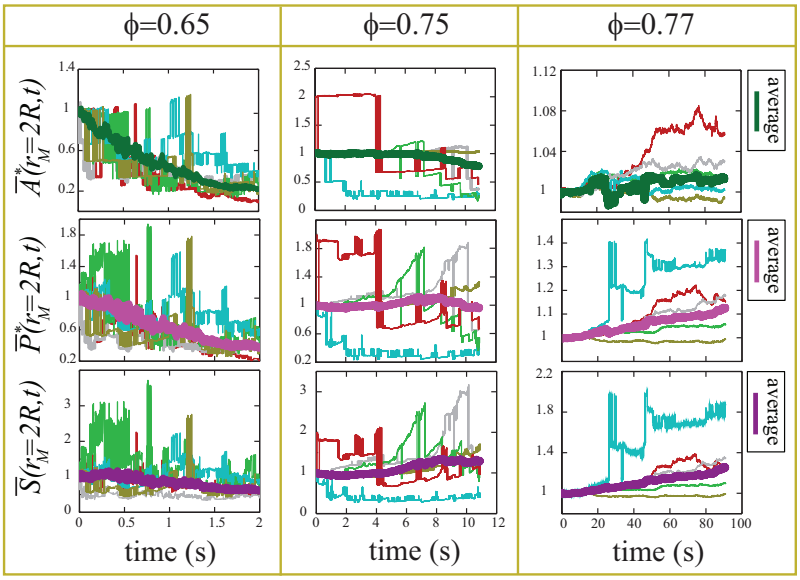

Figure 5.13: Deviations from the average in the deformation process of the floater clusters in time, for low, intermediate, and high ϕ [$\phi = 0.65$, $\phi = 0.75$, and $\phi = 0.77$, respectively]. In all cases, the initial groups are defined by $R_{\text{group}} = 10R$, which is the radius of the circle inside which the floaters are initially positioned. Three morphological quantities of the floater clusters, the area $\overline{A}^*$ [upper row], perimeter $\overline{P}^*$ [middle row], and aspect ratio $\overline{S}$ [bottom row] are shown as a function of time. All are calculated with the Minkowski disc radius $r_M = 2R$, where R is the average floater radius. The average quantities, represented by the bold green line for $\overline{A}^*$, the bold magenta line for $\overline{P}^*$, and the bold purple line for $\overline{S}$, are determined by averaging over many subgroups (≈ 200). The other lines (grey, cyan, green, olive, and red), are the time evolution of the same quantities for arbitrarily chosen, individual subgroups. Clearly, the individual subgroups exhibit a much larger spread when compared to the behavior of the average. [All curves are normalized by the corresponding values at the initial time, such that they are equal to 1 when t=0.]

In Fig. 5.13, we compare the time evolution of $\overline{A}^*$, $\overline{P}^*$, and $\overline{S}$ of individual floater clusters to the average of these quantities for three values of ϕ. The time evolution for the five individual floater clusters presents a much larger spread than the averages. At low ϕ, the deformations of the individual groups follow the average behavior, i.e., all curves almost immediately decay as a function of time [the first column in Fig. 5.13]. There, each cluster breaks up into many children clusters so that the number of clusters $[M_2(r)]_{\text{clusters}}$ increases. This is the reason why all morphological quantities decrease for later times. The quantities fluctuate a lot due to highly mobile floater clusters. At low ϕ, both the amount of free space in which the clusters can spread is large, and the oscillatory forces that are due to the capillary Faraday waves dominate the system [see the clearly visible surface waves in Fig. 5.9, 5.11(III)]. As a consequence, the floater clusters frequently break up and come together again. Each disjointing event increases $[M_2(r)]_{\text{clusters}}$, on the other hand, when the separated parts rejoin the main body $[M_2(r)]_{\text{clusters}}$ decreases again. Therefore, large temporal fluctuations in $\overline{A}^*$, $\overline{P}^*$, and $\overline{S}$ are observed.

In contrast, at intermediate and high ϕ [the second and the third columns in Fig. 5.13, respectively], the floater clusters are less likely break into pieces so that less temporal fluctuations occur compared to the fluctuations at low ϕ. Most notably, the fluctuations are drastically decreased at high ϕ. Moreover, similar to what happens at low ϕ, at high ϕ the deformations of the individual clusters follow the average behavior. However, in sharp contrast to low ϕ, all curves increase as a function of time. This is because the deformation from the compact circular initial cluster to the stretched filamentary cluster is much more frequent than the break-up process at these high values of ϕ. Remarkably, at intermediate ϕ, the deformations of individual clusters do not necessarily follow the average behavior: Where the grey and olive curves increase, the others mainly decrease as a function of time. This suggests that at intermediate ϕ, the deformation towards the filamentary structures and the break-up process compete with each other such that large deviations from the average behavior can occur. Nevertheless, the above qualitative view is not sufficient to understand the complete spreading behavior of the floater clusters. Therefore, we will now calculate the variance of $\overline{A}^*$, $\overline{P}^*$, and $\overline{S}$

$$\begin{aligned}
\text{var}(\overline{A}^*) &= (1/N)\left[<\overline{A}^*(r_M=2R,t)^2>_{\text{group},t} - <\overline{A}^*(r_M=2R,t)>^2_{\text{group},t} \right], \quad (5.3)\\
\text{var}(\overline{P}^*) &= (1/N)\left[<\overline{P}^*(r_M=2R,t)^2>_{\text{group},t} - <\overline{P}^*(r_M=2R,t)>^2_{\text{group},t} \right],\\
\text{var}(\overline{S}) &= (1/N)\left[<\overline{S}(r_M=2R,t)^2>_{\text{group},t} - <\overline{S}(r_M=2R,t)>^2_{\text{group},t} \right],
\end{aligned}$$

where $<>_{\text{group},t}$ indicates that the averages are taken with respect to both the ensemble of subgroups and time. Here, N is the average number of floaters within the subgroup such that $N \approx \phi \pi R_{\text{group}}^2/\pi R^2$. The results are shown in Fig. 5.14 as a function ϕ for various values of the initial group radius R_{group}. For all three morphological quantities we observe an expected large spread at low ϕ, which for increasing ϕ first decreases, but then increases again at intermediate ϕ due to the competition between break-up and stretching. Finally, for the largest values of ϕ, the amount of spread decreases significantly.

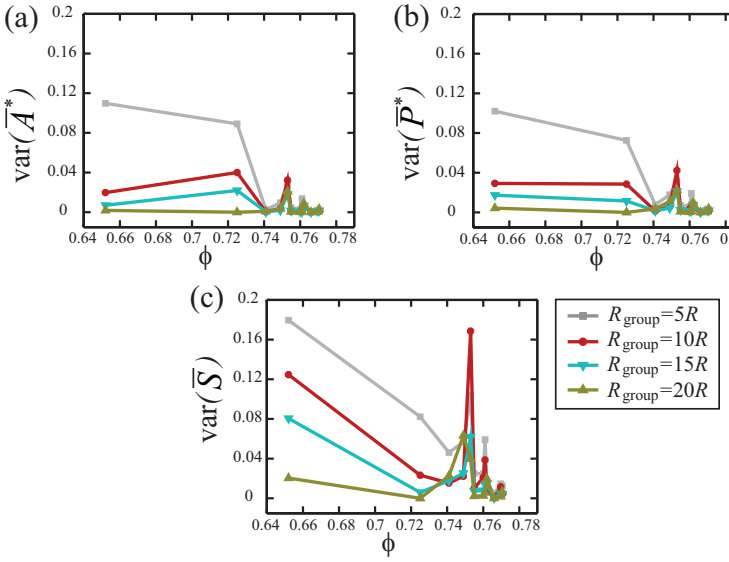

Figure 5.14: The variance of the morphological quantities as a function of ϕ. The radius which determines the initial subgroup size R_{group} is varied from $5R$ to $20R$. The agreement in the results for all morphological quantities and R_{group} is remarkable. The variance of the area $\overline{A}^*(r_M = 2R,t)$ (a), perimeter $\overline{P}^*(r_M = 2R,t)$ (b), and aspect ratio $\overline{S}(r_M = 2R,t)$ (c) indicate an increasing amount of spread at the intermediate ϕ region, i.e., $\phi = 0.753$-0.761 for each R_{group}. Besides this, there is a large amount of spread at low ϕ due to the highly mobile clusters, in this end of the spectrum.

Time analysis of the deformation process

In this Subsection, we will characterize the typical time scale of the morphological deformation of the floaters clusters as a function of ϕ. The resultant experimental analysis is presented in Fig. 5.15.

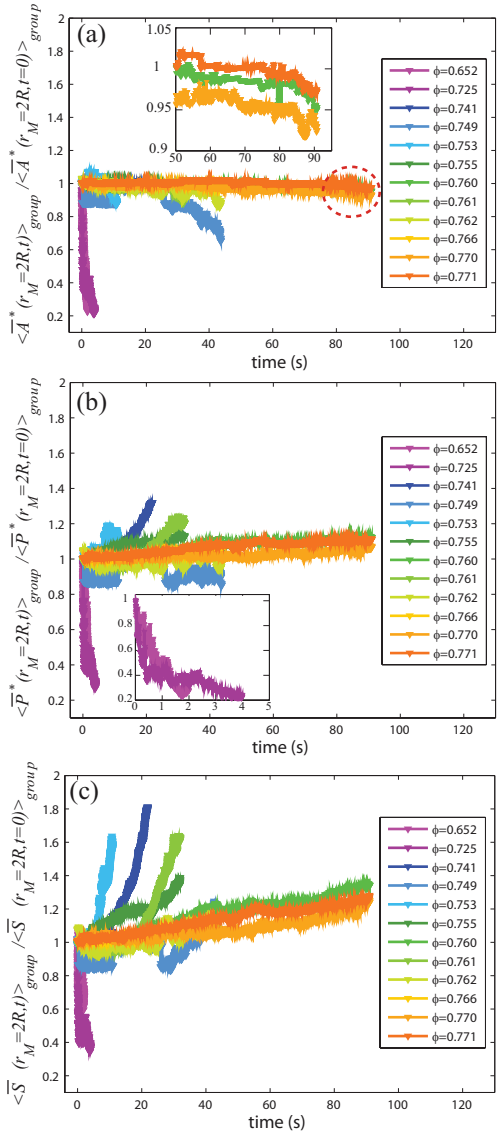

Figure 5.15: The time evolution of the averaged morphological quantities area (a), perimeter (b), and aspect ratio (c) as a function of ϕ. The average has been taken over many subgroups with a fixed size $R_{\text{group}} = 15R$ for each ϕ. See main text for an extensive discussion of these results.

In the previous Subsection, in Fig. 5.11, the time evolution of the three morphological quantities, namely the area $\overline{A}^*(t)$, perimeter $\overline{P}^*(t)$, and aspect ratio $\overline{S}(t)$ have been examined at low, intermediate and high ϕ values. Here, we perform a statistical analysis for many different values of ϕ, where we determine the quantities average over many subgroups (≈ 200 for each ϕ).

In Fig. 5.15, each morphological quantity is normalized by the ensemble average ($<>_{\text{group}}$) of the corresponding values at the initial time ($t = 0$). As a consequence, all are equal to 1 when $t = 0$. From this initial value, both an increase and a decrease can occur. To understand the physical reason for this behavior, the discussion of Fig. 5.13 provided in the previous Subsection is useful, where we explained the decays and growths of the curves in terms of the competition between the break-up and stretching processes. When the break-ups dominate the quantities decay. This is commonly observed at low ϕ, and is the reason why in this case all curves sharply decay as a function of time [ϕ =0.652, 0.725 in Fig. 5.15(a-c); an illustration of this sharp decays at low ϕ is provided in the inset of Fig. 5.15(b).]

In $\overline{A}^*(t)$ [Fig. 5.15(a)], next to the sharp decays at low ϕ, we observe smooth decays at intermediate ϕ [ϕ =0.741-0.762]. For high ϕ, large plateau regions indicate that a very large time is required to observe any deformation of the floater clusters [as far as it is reflected in $\overline{A}^*(t)$]. The slight decay afterwards is again the resultant of the competition between the break-up and the deformation. For all ϕ, the deformation towards the filamentary clusters is expected to increase $\overline{A}^*(t)$. The increase in $\overline{A}^*(t)$ is however much smaller than the amount of increase in $\overline{P}^*(t)$ [Fig. 5.15(b)] and $\overline{S}(t)$ [Fig. 5.15(c)]. This stands to reason, because when a round cluster deforms into a filamentary one, its perimeter and aspect ratio increase significantly, in contrast to its area.

Whereas for intermediate ϕ we observe a decay of $\overline{A}^*(t)$ due to the occurrence of break-ups, in $\overline{P}^*(t)$ and $\overline{S}(t)$ we find an increase with time due to the large growth of perimeter and aspect ratio during the deformation to filamentary clusters, which completely overpowers the break-ups. This effect is particularly strong for the aspect ratio $\overline{S}(t)$. Furthermore, we observe that the curves become less steep when ϕ increases which stands to reason since there we expect less and slower deformation.

As stated above, for the highest values of ϕ [ϕ =0.766-0.771], almost no variation is observed in $\overline{A}^*(t)$. As was the case for intermediate ϕ, $\overline{P}^*(t)$ [Fig. 5.15(b)] and $\overline{S}(t)$ [Fig. 5.15(c)] are much more sensitive and are able to capture the deformation very well for large ϕ, where the quantities increase in an almost linear way. Again, the amount of increase in $\overline{S}(t)$ is larger than in $\overline{P}^*(t)$. Before commenting on the non-

monotonic behavior in the deformation at some ϕ values, we will quantify first the time required to observe a finite deformation when ϕ increases.

In Fig. 5.15, we have observed very rich behavior of the deformation in time as a function of ϕ. How can we determine an accurate and meaningful typical morphologic deformation time τ_m precisely determined for each ϕ? To this end, several procedures will be applied. Let us start with the method we use at low ϕ where we only see sharp decays which may be approximately expected to be fitted by an exponential. In this regime, as presented in the inset of Fig. 5.15(b), the decays are heavily fluctuating, such that directly fitting the curve to an exponential is hard. Therefore, we use an integral measure instead

$$\tau_m = \frac{\int_0^\infty t\, f(t)\, dt}{\int_0^\infty f(t)\, dt}, \tag{5.4}$$

where $f(t)$ is the measured decay. This integral measure is equivalent to the value obtained from a fit when $f(t)$ is exponential and is valid for an infinite data set. To utilize the definition for a finite data set, we extend the data with an exponential fit $C\exp(-t/\tau_m)$ from the end limit of the data t_{end} to infinity

$$\tau_m = \frac{\int_0^{t_{end}} t\, f(t)\, dt + \int_{t_{end}}^\infty t C \exp\left(-\frac{t}{\tau_m}\right) dt}{\int_0^{t_{end}} f(t)\, dt + \int_{t_{end}}^\infty C \exp\left(-\frac{t}{\tau_m}\right) dt}. \tag{5.5}$$

Here, the coefficient of the exponential fit $C = 1$ since the decaying curves are equal to 1 when $t = 0$. In this expression, the first integrals are obtained by numerically integrating the data, and the second integrals can be calculated exactly:

$$\tau_m = \frac{\int_0^{t_{end}} t\, f(t)\, dt + \tau_m(t_{end} + \tau_m)\exp\left(-\frac{t_{end}}{\tau_m}\right)}{\int_0^{t_{end}} f(t)\, dt + \tau_m \exp\left(-\frac{t_{end}}{\tau_m}\right)}. \tag{5.6}$$

This equation works nicely for the concave decays. For other values of ϕ we have a linear decay or growth or even a concave growth [Fig. 5.15(b,c)]. The linear decays and growths are fitted to $1 \pm t/\tau_m$, and the concave growths are fitted to an exponential in the same spirit as the decays discussed above.

τ_m is determined for each of the morphological quantities in Fig. 5.15. As a consequence we have three deformation time $\tau_{\overline{A}^*}$, $\tau_{\overline{P}^*}$, and $\tau_{\overline{S}}$ for $\overline{A}^*(t)$, $\overline{P}^*(t)$, and $\overline{S}(t)$,

respectively. The results are given as a function of ϕ in Fig. 5.16. For all three quantities we observe a clear slowing down of the dynamics. The time scale at which our morphological observables change increase with more than two orders of magnitude for the ϕ interval we have studied here.

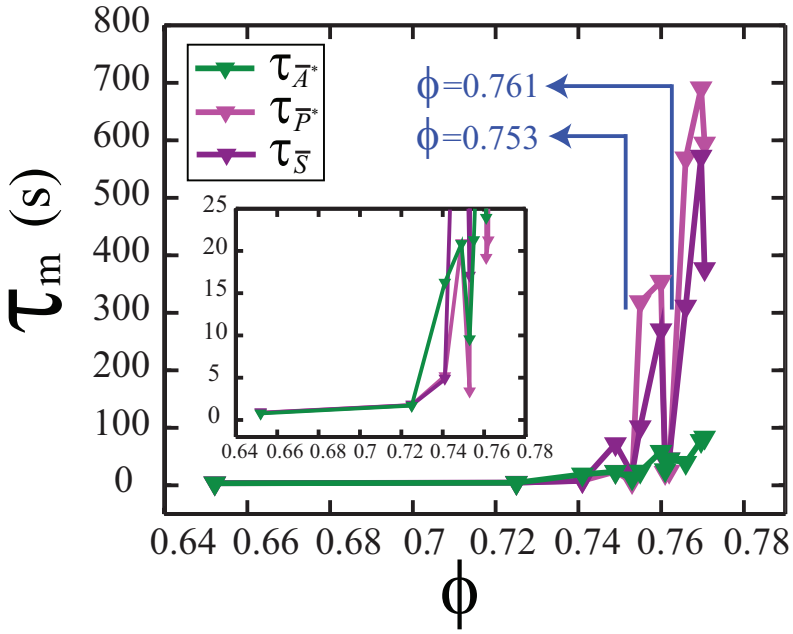

Figure 5.16: The morphologic deformation times τ_m as a function of ϕ. There is a general increasing trend for each τ_m, namely the deformation time of the area $\tau_{\overline{A}^*}$, perimeter $\tau_{\overline{P}^*}$, and aspect ratio $\tau_{\overline{S}}$, which indicates the slowing down of the dynamics when ϕ increases. There are two values of ϕ, namely $\phi = 0.753, 0.761$, which deviate substantially from the expected increasing trend. This is discussed in the main text. The deformation time is found to be much larger for $\overline{P}^*$ and $\overline{S}$ relative to the values for $\overline{A}^*$ at intermediate and high ϕ regimes. The inset shows the typical time scales at low ϕ.

There are however two values of ϕ, namely $\phi = 0.753, 0.761$, in that do not follow the trend in Fig. 5.16. This brings us to the comparison with the time analysis of the heterogeneities performed using the half width of the self-overlap order parameter $Q(l, \tau)$ and the peak position of the dynamic susceptibility $\chi_4(l, \tau)$ in the previous Section. There, both time scales, namely $w_Q(l, \phi)$ and $\tau_{\chi_4}(l, \phi)$, give anomalous minima at precisely the same values of ϕ, namely $\phi = 0.753, 0.761$. In the next section, we both comparatively discuss the all time scales obtained using $\chi_4(l, \tau)$ and the morphology approach, and explain the broken trend observed for all these time scales at $\phi = 0.753, 0.761$.

5.5 Comparison between two methods

In the previous Sections, we have quantified the ϕ dependence of the typical time scale of the dynamics of dense cohesive floaters on capillary ripples using the four-point dynamic susceptibility $\chi_4(l, \phi)$ [see Section 5.3.1] and the morphological approach [Section 5.4.1]. Two main results are shown comparatively in Fig. 5.17.

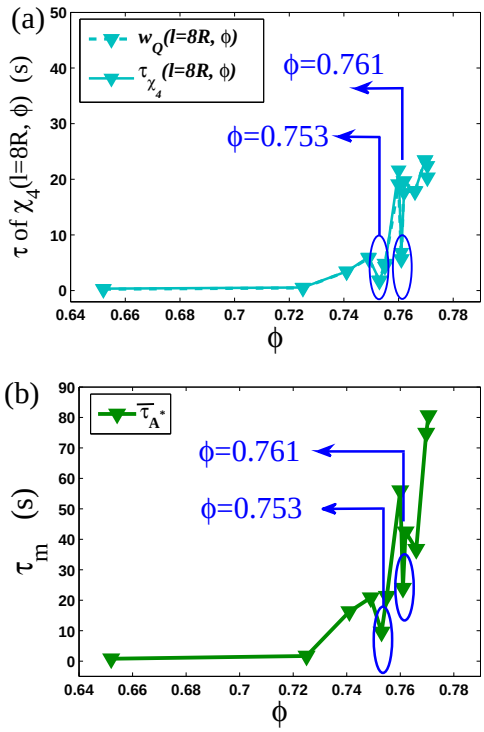

Figure 5.17: Comparing the time scales of the dynamics of dense cohesive floaters on capillary ripples determined using the two different methods discussed in this Chapter. (a) The time scales following from the four-point dynamic susceptibility $\chi_4(l = 8R, \phi)$, namely the decay width $w_Q(l = 8R, \phi)$ and the peak position of the susceptibility $\tau_{\chi_4}(l = 8R, \phi)$, both as a function of ϕ. (b) One of the time scales following from the morphology approach, namely the deformation time of the area $\tau_{\overline{A}^*}$, as a function of ϕ. There is a good qualitative agreement between the two methods. Remarkably, in both cases the trend is broken for the same values of ϕ, namely $\phi = 0.753$ and 0.761.

For both methods, we observe a broken trend in the ϕ dependence of the time scales for the same two values of ϕ, namely $\phi = 0.753, 0.761$. This encourages us to go back to the experiments, where we observe a large scale floater motion which appears to vary significantly with ϕ. This large scale motion has a range in the order of

one hundred floater radii for each ϕ and is markedly larger for some of our experimental runs. It could well be that the presence of a large drift significantly changes the dynamics of our system in the sense that it influences the speed at which the stretching and break-up processes we are studying take place. To test this, we compute the following measure for the average drift velocity

$$< v >_{\text{floater},t} = \sqrt{\left\langle \left(\frac{1}{N} \sum_{i=1}^{N} v_{x,i}(t) \right)^2 + \left(\frac{1}{N} \sum_{i=1}^{N} v_{y,i}(t) \right)^2 \right\rangle_t}, \tag{5.7}$$

where $v_{x,i}(t)$ and $v_{y,i}(t)$ are the horizontal and vertical velocities of each floater i respectively, and the summations run over all floaters in our experimental field of view (namely N). $<>_t$ represents the time averages. Essentially, in Eq. 5.7 we compute the average velocity of the particles for each time step and subsequently average their squared magnitudes over time.

The results are shown in Fig. 5.18 as a function of ϕ. Indeed we find that the values of ϕ that break the trend in Figs. 5.17(a,b), namely $\phi = 0.753$ and $\phi = 0.761$, are characterized by anomalously large drift velocity in Fig. 5.18, in agreement with our expectation.

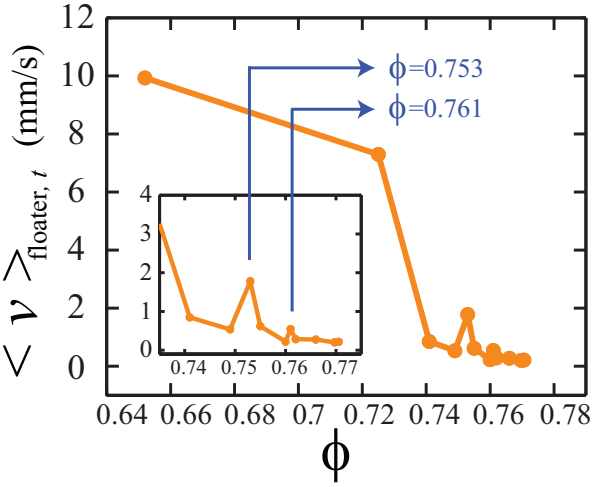

Figure 5.18: The mean velocity of the floaters $< v >_{\text{floater},t}$ as a function of ϕ. The very sharp decrease from $\phi = 0.72$ to $\phi = 0.74$ suggests a dramatic slowing down of the dynamics. However, no monotonic decreasing trend is observed when ϕ increases. The positions of the peaks (marked with the blue arrows) are remarkable, since they indicate that the drift is anomalously large for those values of ϕ for which also all of the time scales characterizing the dynamics are anomalously small [see Figs. 5.17(a,b)].

5.6 Conclusion

We have studied the dynamics of dense cohesive floating macroscopic spheres on capillary ripples. Our experimental observations suggest highly heterogeneous motion in space and irregular dynamics in time. These heterogeneities and irregularities are the resultant of floater clusters formed under the influence of the driving by erratic forces due to short-wavelength capillary Faraday waves and attractive capillary forces. Such kind of heterogenous motion is also reported in the other particulate systems where it has been called dynamic heterogeneity. Examples are colloidal glasses [6–9] and dry granular media [10–14]. There, the dynamics is characterized by the four-point dynamic susceptibility when the systems are close to the jamming point.

To characterize the heterogeneous dynamics of our attractive floaters, we also apply the four-point dynamic susceptibility $\chi_4(l,\tau)$, but further away from the jamming point than the previous studies. Examining the decay of the self-overlap order parameter $Q(l,\tau) =< Q_t(l,\tau) >_t$ (also referred to as the time-averaged mobility) and the position of the maximum of $\chi_4(l,\tau)$ as a function of ϕ provides the time scales of the dynamics, namely $w_Q(l,\phi)$ and $\tau_{\chi_4}(l,\phi)$, respectively, which are in very good agreement with each other both qualitatively and quantitatively. We show that the general trend is that $w_Q(l,\phi)$ and $\tau_{\chi_4}(l,\phi)$ increase with ϕ [except for two values, $\phi = 0.753, 0.761$], which suggests a slowing down of the dynamics at high ϕ. By varying l in a reasonably large range (from $2R$ to $15R$ with R the floater radius), we have showed that the results are robust, i.e, changing l does not change the resultant behavior of the time scales significantly, apart from the expected increase for increasing l.

Next to the time scales, also the peak height $h_{\chi_4}(l,\phi)$ of $\chi_4(l,\tau)$ is examined to quantify the amount of the heterogeneity as a function of ϕ. At intermediate and high ϕ, the increasing trend of $h_{\chi_4}(l,\phi)$ demonstrates that the dynamics more heterogenous with increasing ϕ. This is consistent with the results in the literature for both colloidal glasses [6–9] and dry granular systems [10–14], where the systems are close to the jamming point. However, at low ϕ, we have found that the amount of heterogeneity is larger at the lowest ϕ compared to the intermediate ϕ and decreases afterwards, and as a consequence does not follow the same trend as in the dense limit. To confirm this behavior, it would be valuable to perform additional experiments in the low ϕ limit.

In addition to the analysis based on the four-point dynamic susceptibility, in this Chapter we have developed a new morphological approach to characterize the dy-

namics of the floaters and visualize the floater clusters in time. This analysis is based on the Minkowski functionals that were already introduced and discussed in detail in Chapter 4 of this Thesis. By utilizing the physical interpretation of the Minkowski functionals, we have characterized the morphological deformation of initially constructed subgroups in time, namely the area $\overline{A}^*(t)$, the perimeter $\overline{P}^*(t)$, and the aspect ratio $\overline{S}(t)$. Decreasing $\overline{A}^*(t)$, and increasing $\overline{P}^*(t)$ and $\overline{S}(t)$ with time t at intermediate and high ϕ suggest that the initial compact, circular floater clusters evolve into stretched filamentary clusters with time. At low ϕ, however, all quantities decrease indicating that here break ups dominate the deformation process and the stretching mechanism is less important.

Moreover, we have determined the three typical morphological deformation times τ_{m}, namely $\tau_{\overline{A}^*}$, $\tau_{\overline{P}^*}$, and $\tau_{\overline{S}}$ for $\overline{A}^*(t)$, $\overline{P}^*(t)$, and $\overline{S}(t)$, respectively. All increase as a function of ϕ, consistent with a slowing down of the dynamics. In addition, all curves, although quantitatively different, qualitatively show the same trend. Remarkably, we have shown that the increasing trend is broken by the same two ϕ values, $\phi = 0.753, 0.761$ for which we have also observed anomalous minima in $w_Q(l,\phi)$ and $\tau_{\chi_4}(l,\phi)$.

Finally, we have comparatively discussed the time scales obtained from the two methods, i.e., the four-point dynamic susceptibility and the morphology approach. We have found very good qualitative agreement. In how far there is quantitative agreement is still an open question. Furthermore, by determining the average floater velocity as a function of ϕ, we have shown that two maxima occurs at $\phi = 0.753, 0.761$, where the velocity becomes anomalously large compared to that at the nearby ϕ. These are the same ϕ for which the trend in the time scales is broken. The presence of a large mean floater flow may therefore well be a plausible explanation for the occurrence of the anomalous behavior in the time scales for these values of ϕ.

References

[1] L. Berthier, "Dynamic heterogeneity in amorphous materials", Physics **4**, 42-1–7 (2011).

[2] L. Berthier, "Time and length scales in supercooled liquids", Phys. Rev. E (R) **69**, 020201-1–4 (2004).

[3] L. Berthier, G. Biroli, J.-P. Bouchaud, L. Cipelletti, D. El Masri, D. L'Hôte, F. Ladieu, M. Pierno, "Direct Experimental Evidence of a Growing Length Scale Accompanying the Glass Transition", Science **310**, 1797–1800 (2005).

[4] L. Berthier, G. Biroli, J.-P. Bouchaud, W. Kob, K. Miyazaki, and D. R. Reichman, "Spontaneous and induced dynamic fluctuations in glass formers. I. General results and dependence on ensemble and dynamics", J. Chem. Phys. **126**, 184503-1–21 (2007).

[5] L. Berthier, G. Biroli, J. P. Bouchaud, L. Cipelletti, and W. van Saarloos, *Dynamical Heterogeneities in Glasses, Colloids, and Granular Media*, (Oxford University Press, Oxford), (2011).

[6] L. Berthier and G.Biroli, "Theoretical perspective on the glass transition and amorphous materials", Rev. Mod. Phys. **83**, 587–645 (2011).

[7] T. Narumi, S. V. Franklin, K. W. Desmond, M. Tokuyama, and E. R. Weeks, "Spatial and temporal dynamical heterogeneities approaching the binary colloidal glass transition", Soft Matter **7**, 1472–1482 (2011).

[8] Y. Rahmani, K. van der Vaart, B. van Dam, Z. Hu, V. Chikkadi, and P. Schall, "Dynamic heterogeneity in hard and soft sphere colloidal glasses", Soft Matter **8**, 4264–4270 (2012).

[9] S. Jabbari-Farouji, R. Zargar, G. H. Wegdam, and Daniel Bonn, "Dynamical heterogeneity in aging colloidal glasses of Laponite", arXiv:1201.4795v2 [cond-mat.soft] (2012).

[10] O. Dauchot, G. Marty, and G. Biroli, "Dynamical Heterogeneity Close to the Jamming Transition in a Sheared Granular Material", Phys. Rev. Lett. **95**, 265701-1–4 (2005).

[11] A. S. Keys, A. R. Abate, S. C. Glotzer, and D. J. Durian, "Measurement of growing dynamical length scales and prediction of the jamming transition in a granular material", Nature Phys. **3**, 260–264 (2007).

[12] A. R. Abate and D. J. Durian, "Topological persistence and dynamical heterogeneities near jamming", Phys. Rev. E **76**, 021306-1–9 (2007).

[13] F. Lechenault, O. Dauchot, G. Biroli, J. P. Bouchaud, "Critical scaling and heterogeneous superdiffusion across the jamming/rigidity transition of a granular glass", Eur. Phys. Lett. **83**, 46003-1–6 (2008).

[14] F. Lechenault, R. Candelier, O. Dauchot, J. P. Bouchaud, and G. Biroli, "Super-diffusion around the rigidity transition: Levy and the Lilliputians", Soft Matter **6**, 3059–3064 (2010).

[15] P. Mayer, H. Bissig, L. Berthier, L. Cipelletti, J. P. Garrahan, P. Sollich, and V. Trappe, "Heterogeneous Dynamics of Coarsening Systems", Phys. Rev. Lett. **93**, 115701-1–4 (2004).

[16] D. Ertaş and T. C. Halsey, "Granular gravitational collapse and chute flow", Europhys. Lett. **60**, 931–937 (2002).

[17] T. C. Halsey and D. Ertaş, "Coherent Structures in Dense Granular Flows", arXiv:cond-mat/0506170v1 (unpublished), 1–4 (2005).

[18] S. Douady, "Experimental study of the Faraday instability", J. Fluid Mech. **221**, 383–408 (1990).

[19] C. Duez, C. Ybert, C. Clanet, L. Bocquet, Nat. Phys. 3, 180 (2007). See the section Methods for the cleaning protocol of both hydrophilic (wetting) glass material and hydrophobic teflon (non-wetting) particles. Note that we immerse the hydrophilic glass container in piranha solution (1 vol H2O2, 2 vol H2SO4) for 25 min. The cleaning procedure for our hdrophilic polystyrene consists of rinsing the spheres with isopropanol. Then, both the container and the spheres are dried separately, and further heated to remove all the chemicals. Since the spheres are hydrophilic polystyrene, the suggested heating temperature is 70°C at most. We heated the spheres, as well as the container, at 65°C for 1 hour. Finally, both the container and the spheres are left to cool to ambient temperature.

[20] T. Peng, "Detect circles with various radii in grayscale image via Hough Transform", http://www.mathworks.com/matlabcentral/fileexchange/9168, Copyright (c) 2006.

6

General conclusion and outlook

In this Thesis, we studied a monolayer of macroscopic particles floating on a surface wave. The liquid is pure water so that the particles are at a water-air interface. The particles are hydrophilic polystyrene spheres with an average radius R around 0.31 mm, polydispersity 14%, and slightly heavier than water. The surface wave is a Faraday wave, generated at a liquid-air interface when a layer of liquid is exposed to a vertical periodic driving. We examined experimentally the effect of the floater concentration on the dynamics of the floaters in two different regimes, namely where the wavelength λ is much larger than R and where λ is of the order of R.

In Chapter 2, we described a floating sphere on a static liquid-air interface. Following the literature [1, 2], we showed how the sphere's hydrophobicity and density combine into a single equation providing the sign of the curvature and the equilibrium depth of the sphere. We then calculated the magnitude of the attractive capillary force and energy between two identical spheres and generalize them for an ensemble of spheres. In the second part of this Chapter, we summarized the dynamics of a single sphere on a standing wave. We provided a derivation of the drift force and showed that the direction of the drift force is determined by the direction of the surface tension force on the sphere in the static case. In the literature [3–5], it was stated that a hydrophilic sphere drifts towards a standing wave amplitude

minimum (node), whereas a hydrophobic sphere goes to the maximum (antinode). We showed that this is an oversimplification and that it is actually the sign of the curvature that determines the direction of the drift force.

In Chapter 3, we investigated the role of the particle concentration ϕ on the spatial distribution of our hydrophilic heavy spheres floating on a standing Faraday wave, with a wavelength much larger than the particle radius R. For low ϕ, we observed that our floaters form clusters at the antinodes, as expected because the sign of the curvature of our floater is positive. Just by increasing ϕ to a high value, we observed the spontaneous formation of the inverse patterns, i.e., clusters at the nodal lines of the wave. A key difference between the two patterns is that the antinode clusters *breath*: The floaters periodically move towards and away from the antinodes and, as a consequence, also from each other. We analyze the pattern formation using the two mechanisms driving the floaters, namely the drift and the attractive capillary interaction. More specifically, we developed an energy calculation in which we show that for low ϕ antinode clusters are energetically favorable and for large ϕ node clusters have the lowest energy. We showed that this effect is dominated by the drift energy and that breathing plays a crucial role: Without incorporating the breathing, no transition occurs.

In Chapter 4, we examined the morphological differences between the experimentally observed concentration dependent floater patterns of the previous Chapter in various ways. The observation that there are three different length scales that determine the patterns, namely the wavelength λ (≈ 18 mm), the capillary length ($L_c = 2.7$ mm), and the mean floater radius ($R = 0.31$ mm), incites us to perform the analysis both globally ($\sim \lambda$) and locally ($\sim L_c$ and $\sim R$). In the global part, we applied the Minkowski point pattern approach, and moved beyond the existing literature [6–8] by introducing derived functionals with a direct physical interpretation. From the three original Minkowski functionals as well as the three derived functionals we confirm and quantify three regimes of the clustering patterns suggested by the experiment: Circular compact antinode clusters at low ϕ, filamentary heterogeneous clusters at intermediate ϕ, and grid-shaped node clusters at high ϕ. In the local part of the analysis, we calculated the local bond orientational order parameter $|\Psi_6|$ and determined the pair correlation function $g(r)$. Using $|\Psi_6|$ we determine where and to what extent the floater patterns are different from a hexagonal packing. From the number and decay of the peaks of $g(r)$ we demonstrated how the amount of order in the structures varies as a function of ϕ. We showed that the order in the low ϕ region is limited due to the restricted size of the antinode clusters and the breathing.

There is also little order at intermediate ϕ due to the loosely packed structures in this regime. For the highest ϕ however, we observe a dramatic increase in the height and number of peaks indicating that highly long-range ordered structures evolve.

In Chapter 5, we moved from the standing Faraday wave limit towards nonlinear chaotic waves with a much smaller wavelength in the order of the floater diameter (≈ 0.62 mm). Here, we use a monolayer of our hydrophilic polystyrene spheres in a densely packed situation such that the floater concentration is between $\phi = 0.65$ and $\phi = 0.77$. Wave drift is absent, and the floaters are driven by the erratic driving forces due to the Faraday waves and held together by the capillary attraction. We demonstrated that the flow of such a floater layer is composed of floater domains: Floater groups that initially move together, break up into small pieces some time later. During the break-up process, groups also deform morphologically. We characterized the deformation by applying the technique introduced in Chapter 4, using the physical Minkowski functionals. By characterizing the average area, perimeter, and aspect ratio of each subgroup as a function of time, we found that at low ϕ ($\approx 0.65 - 72$), the break-ups dominate the motion. However, at intermediate ϕ ($\approx 0.74 - 0.76$) and high ϕ ($\approx 0.76 - 0.77$), instead of breaking up, the initial compact, circular floater clusters evolve into stretched filamentary clusters. In addition to this, we examined the heterogeneous dynamics by a technique borrowed from the literature, the four-point dynamic susceptibility χ_4 [9–14]. We compare τ_{χ_4}, the time scale from χ_4, with τ_{m}, the time scale following from the Minkowski analysis and found good qualitative agreement, i.e., both increase with increasing ϕ indicating the slowing down of the dynamics. The anomalously small time scales we found for two values of ϕ were connected to the presence of a very large average velocity in the system.

To summarize this Thesis in a single sentence, we studied two aspects of floaters on Faraday waves: The spatial distribution of clusters on a standing Faraday wave and the dynamics of densely packed floaters on chaotic Faraday waves. As most scientific research, also ours opens more questions than it answers. This is especially true since the research of the behavior of floaters on water-air interfaces has just started and still needs to become a mature field. We will now address a few of these questions.

In Chapter 3, we examined the system roughly for an hour of experimental runtime. However, especially for the patterns at intermediate ϕ how the patterns evolve in the very long term is an open question. Does the observed pattern at certain ϕ undergo a transition to yet another pattern? Is there a robust final pattern? If so, what

controls the position and the shape of the final pattern? Possibly, answers to these questions and the observations reported in this Thesis, specifically self-organization of the floaters and the emergence of order, would be useful to understand much more general research issues, such as some aspects in social life. Groups of people walk in a very organized way in a crowded street, i.e., the people going a certain direction spontaneously organize into lanes without any enforcement. Cars in traffic move in an organized way. People fill a seminar room exhibiting an order at the end. People in a shopping center prefer to move in similar very restricted pathways, and as a consequence, certain parts of the floor get dirty and old very quickly compared to other parts. All those examples suggest that, just like physical systems, we have also some internal dynamics forcing us to organize. In the system studied in this Thesis, floating macroscopic spheres on a standing Faraday wave, emergence of order is described by a simple model considering only two mechanisms, namely the wave drift and attractive capillary interaction (we also showed that even the drift mechanism together with the breathing is sufficient). For both fundamental understanding and contributing to how we can build our cities, roads, and shopping centers in a more desirable way for large groups of people, social sciences may get very well benefit from our knowledge of how similar self-organization occurs and structures emerge in a relatively simple and well-controlled physical system.

In Chapter 4, we briefly studied the packing of the floaters. Especially in the dynamic case, a more detailed packing analysis would be valuable, and the same is true for establishing a connection to the literature on packings of emulsions [15], polydisperse frictionless spheres [16], polydisperse hard disks [17], and local volume fluctuations of driven dense dry granulars [18] which all suggest universal laws in packings.

Chapter 5 which deals with the dynamics of densely packed floaters on capillary Faraday waves, contains many remaining unexplored issues. First, we limited our study of the system to floater concentrations relatively far from the jamming point. A more detailed analysis of the heterogeneities could be performed by studying the dense cohesive grains much closer to the jamming point using a well-defined and well-studied method, the four-point correlation function G_4 [11–14]. G_4 has successfully explained the drastic increase in collective events and characterized the divergence of the correlation length close to the jamming point in driven dry granular materials [11–14]. This diverging correlation length could be essential to pinpoint the jamming point ϕ for our chaotically driven cohesive floaters.

Second, we observed the formation of dynamic groups in a densely packed monolayer of cohesive floaters. Our observation reminds us of the granular clusters formed in dense chute flow [19, 20]. Local events such as formation of these clusters and fluctuations [21, 22] at the surface of the chute are highly dependent on the angle of inclination and the thickness of the chute. The similarity between these granular clusters and the eddy structures observed in turbulent flow has been pointed to, and the time and length scales of the granular eddies in dense chute flow were theoretically characterized [19, 20]. Experimentally, we found no study providing comparative analysis between the granular and turbulent eddies. (A comparative numerical study on fluctuations generated in two-dimensional sheared granular motion with turbulent fluctuations [23] is the only study we are aware of.) To perform such an analysis would be valuable for both the granular and the turbulence community. Our system is very well suited for this purpose since we can detect all the groups/clusters/eddies on the two-dimensional wave surface. In addition, the analysis developed in Chapter 5 in principle provides the typical sizes, shapes, and time scale of the structures.

This Thesis is devoted to studying fundamental aspects of floaters on Faraday waves. However, a brief discussion on potential application areas would be valuable. Lets first probe the areas that have already been developed such as the separation processes of ore particles in aqueous systems [24], removing impurities in a melted metal surface [25, 26], and removing plastic contaminants of a paper pulp by injecting gas bubbles [27, 28]. In all areas, floater agglomerations are trapped at a fluid-fluid interface. To design all these methods in an efficient way, knowledge of how an agglomeration floats on a perturbed dynamic interfaces is required. The theories [1, 2, 29, 30] however, have assumed flat and static interfaces. Therefore, understanding how the interface dynamics creates and forms the floater agglomerations, as we contributed to the present Thesis, is essential, and still mainly unexplored.

A further potential application would be cleaning of sea surfaces. A huge amount of waste is disposed into the sea on a worldwide scale, and the consequences are a threat to all its living inhabitants. Effective and less energy consuming cleaning methods need to be developed. We found that creating surface waves can enhance floater agglomerations in an organized way. The segregation of different types of contaminants would also be possible since the contaminants having different physical properties may experience wave drift in opposite directions. Therefore, recycling contaminants from clumps of waste on sea surfaces may be efficiently realized in a

less energy consuming way.

References

[1] D. Y. C. Chan, J. D. Henry, Jr., and L. R. White, "The interaction of colloidal particles collected at fluid interfaces", J. Colloid Interface Sci. **79**, 410–418 (1981).

[2] D. Vella and L. Mahadevan, "The Cheerios effect", Am. J. Phys. **73**, 817–825 (2005).

[3] G. Falkovich, A. Weinberg, P. Denissenko, and S. Lukaschuk, "Floater clustering in a standing wave", Nature (London) **435**, 1045–1046 (2005).

[4] P. Denissenko, G. Falkovich, and S. Lukaschuk, "How waves affect the distribution of particles that float on a liquid surface", Phys. Rev. Lett. **97**, 244501-1–4 (2006).

[5] S. Lukaschuk, P. Denissenko, and G. Falkovich, "Nodal patterns of floaters in surface waves", Eur. Phys. J. Special Topics **145**, 125–136 (2007).

[6] K. R. Mecke, "Additivity, Convexity, and Beyond: Applications of Minkowski Functionals in Statistical Physics", Lecture Notes in Physics (Springer) **554**, 111–184 (2000).

[7] K. Michielsen and H. De Raedt, "Integral-geometry morphological image analysis", Phys. Rep. **347**, 461–538 (2001).

[8] K. R. Mecke and D. Stoyan, "Morphological Characterization of Point Patterns", Biometrical Journal **47**, 473–488 (2005).

[9] A. S. Keys, A. R. Abate, S. C. Glotzer, and D. J. Durian, "Measurement of growing dynamical length scales and prediction of the jamming transition in a granular material", Nature Phys. **3**, 260–264 (2007).

[10] A. R. Abate and D. J. Durian, "Topological persistence and dynamical heterogeneities near jamming", Phys. Rev. E **76**, 021306-1–9 (2007).

[11] F. Lechenault, O. Dauchot, G. Biroli, J. P. Bouchaud, "Critical scaling and heterogeneous superdiffusion across the jamming/rigidity transition of a granular glass", Eur. Phys. Lett. **83**, 46003-1–6 (2008).

[12] F. Lechenault, R. Candelier, O. Dauchot, J. P. Bouchaud, and G. Biroli,

"Super-diffusion around the rigidity transition: Levy and the Lilliputians", Soft Matter **6**, 3059–3064 (2010).

[13] L. Berthier, "Dynamic heterogeneity in amorphous materials", Physics **4**, 42-1–7 (2011).

[14] L. Berthier, G. Biroli, J. P. Bouchaud, L. Cipelletti, and W. van Saarloos, *Dynamical Heterogeneities in Glasses, Colloids, and Granular Media*, (Oxford University Press, Oxford), (2011).

[15] M. Clusel, E. I. Corwin, A. O. N. Siemens, and Jasna Brujić, "A granocentric model for random packing of jammed emulsions", Nature (London) **460**, 611–616 (2009).

[16] E. I. Corwin, M. Clusel, A. O. N. Siemens, and Jasna Brujić, "Model for random packing of polydisperse frictionless spheres", Soft Matter **6**, 2949–2959 (2010).

[17] M. P. Miklius and S. Hilgenfeldt, "Analytical Results for Size-Topology Correlations in 2D Disk and Cellular Packings", Phys. Rev. Lett. **108**, 015502-1–5 (2012).

[18] J. G. Puckett, F. Lechenault, and K. E. Daniels, "Local origins of volume fraction fluctuations in dense granular materials", Phys. Rev. E **83**, 041301-1–8 (2011).

[19] D. Ertaş and T. C. Halsey, "Granular gravitational collapse and chute flow", Europhys. Lett. **60**, 931–937 (2002).

[20] T. C. Halsey and D. Ertaş, "Coherent Structures in Dense Granular Flows", arXiv:cond-mat/0506170v1 (unpublished), 1–4 (2005).

[21] O. Pouliquen, "Velocity Correlations in Dense Granular Flows", Phys. Rev. Lett. **93**, 248001-1–4 (2004).

[22] O. Baran, D. Ertaş, T. C. Halsey, G. S. Grest, and J. B. Lechman, "Velocity correlations in dense gravity-driven granular chute flow", Phys. Rev. E **74**, 051302-1–10 (2006).

[23] F. Radjai and S. Roux, "Turbulentlike Fluctuations in Quasistatic Flow of Granular Media", Phys. Rev. Lett. **89**, 064302-1–4 (2002).

[24] J. D. Henry, M. E. Prudich, and K. R. Vaidyanathan, "Novel separation processes for solid/liquid separations in coal derived liquids", Separa-

tion and Purification Reviews **8**, 81–118 (1979).

[25] H. Shibata, H. Yin, and T. Emi, "The capillary effect promoting collision and agglomeration of inclusion particles at the inert gas-steel interface", Phil. Trans. R. Soc. Lond. A **356**, 957–966 (1998).

[26] K. Nakajima and S. Mizoguch, "Capillary interaction between inclusion particles on the 16Cr stainless steel melt surface", Metall. Mater. Trans. B **32**, 629–641 (2001).

[27] J. Ralston, D. Fornasiero, and R. Hayes, "Bubble-particle attachment and detachment in flotation", Int. J. Miner. Process. **56**, 133–164 (1999).

[28] A. V. Nguyen and H. J. Schulze, "Colloidal Science of Flotation (Surfactant Science)", CRC Press, New York (2003).

[29] N. D. Vassileva, "Behavior of 2D aggregates in shear flow", PhD Thesis, University of Twente (2006).

[30] N. D. Vassileva, D. van den Ende, F. Mugele, and J. Mellema, "Capillary forces between spherical particles floating at a liquid-liquid interface", Langmuir **21**, 11190–11200 (2005).

SUMMARY

Floating bubbles on our drinks, a collection of sea plants floating on a wavy sea surface, or as was studied in this Thesis, floating spherical particles on a surface wave all exhibit a variety of phenomena which look particularly simple, but require detailed study upon closer inspection. When we pour our favorite drink in a glass cup, lots of bubbles are generated at the surface. Most of them immediately move towards the wall of the glass cup, and accumulate there. When we try this with a plastic cup, the bubbles stay in the middle of the surface. A collection of sea plants agglomerate and move with respect to the surface wave elevation. Floating spherical particles on a Faraday wave agglomerate, drift, and as a result, demonstrate pattern formation.

In Chapter 2, following the literature we showed that a macroscopic sphere can float on a static liquid-air interface in four different situations depending on its hydrophobicity and density relative to the carrier liquid. These four possibilities are nicely summarized in a single equation, which describes the shape of the meniscus generated around the floater, and determines the direction of surface tension force. Furthermore, we showed that a single small sphere with a finite wetting angle has to drift towards either the amplitude maximum (antinode) or minimum (node). Contrary to what has been stated in the literature, we found that if the meniscus around the sphere is convex (i.e., when surface tension acts upwards) the sphere drifts towards the antinode, whereas if it is concave (and surface tension acts downwards) the sphere drifts towards the node. Next to the drift, there is an attractive interaction among the floaters induced by gravity and surface tension. We present analysis of both the drift force of a single macroscopic sphere on a standing wave and the attractive capillary force of floating two identical macroscopic spheres on a static liquid-air interface.

In Chapter 3, we found that the same floaters that cluster at the antinodes of the standing water wave at low ϕ, cluster at the nodal lines of the wave at high ϕ. We systematically studied the transition from low to high ϕ. Using high-speed video imaging, we observed that, when the pattern is inverted from antinode to node clus-

ters, not only the position of the floater clusters, but also their dynamics is changed. The antinode clusters breath, i.e., the floaters periodically move towards and away from the antinodes and, as a consequence, also from each other, whereas the node clusters do not breath. By considering drift energy, attractive capillary energy, and the breathing effect, we developed an energy calculation from which we were able to explain the antinode to node cluster transition. Here, including the breathing effect is essential: Without breathing, no transition occurs.

Pattern formation, emergence of order, and self-organization have been observed in many systems from geophysics to biophysics. There, usually a variation in a control parameter enforces the system to form or change a certain pattern. In our system, however, the driving parameters, i.e., the wavelength and amplitude of the wave, are kept constant. Patterns form, change and even invert solely by increasing the number of floating particles per unit of surface area. This sets our system apart from most others that show pattern formation.

In Chapter 4, we characterized the observed floater patterns on a standing Faraday wave from low ϕ to high ϕ, applying both global and local analysis. In a global picture, we employed the Minkowski functionals point pattern approach. We showed that it is a very useful tool to study a variety of properties, such as cluster size, aspect ratio, and connectivity, of the complex floater patterns. In a local context, we studied the local bond orientational order parameter $\mid \Psi_6 \mid$, which measures the deviation from a hexagonal packing, and the pair correlation function $g(r)$. We found that even though $\mid \Psi_6 \mid$ is not a robust tool to characterize our patterns, which often are far from hexagonal order, the method provides a nice illustration of them. $g(r)$ constitutes a better representation of the increasing local order with increasing ϕ. In summary, the concentration dependent floater patterns were characterized as follows: The circular irregularly packed antinode clusters at low ϕ are replaced by loosely packed filamentary structures at intermediate ϕ, and then followed by densely packed grid-shaped node clusters at high ϕ.

In Chapter 5, we turned to a different regime and drove a densely packed monolayer of the same floaters using nonlinear chaotic Faraday waves with a wavelength of the order of the size of a single floater. In this regime, we observed that the flow is composed of floater domains. At low ϕ, small floater groups initially moving together, break up some time later. This process repeats itself continuously. During the break-up process, the initial floater group morphologically deforms such that the initially selected compact, circular subgroups evolve into a stretched, filamentary floater clusters. At intermediate and high ϕ however, the break-up process is less

likely to occur and the motion of the floater clusters is dominated by the morphological deformation due to the stretching. To characterize the resultant heterogenous dynamics of the floater clusters, we developed a morphological method, inspired by the Minkowski point pattern approach of Chapter 4. We also evaluated the dynamical heterogeneities generated by our densely packed cohesive floaters using the four-point dynamic susceptibility known from the literature. When comparing the time scale from the morphological approach with that from the dynamic susceptibility we find good qualitative agreement. This suggests that the morphological approach constitutes a valuable alternative representation of the dynamical heterogeneities. It may even be a stronger tool since it not only provides the time scale and amount of the heterogeneities, as can also be deduced from the dynamic susceptibility, but in addition abundant information on the dynamics of the system, such as providing a visualization of the flow (see the back side of the Thesis cover), morphological deformations in time, and the correlation of the simultaneous motion of many floaters in space. To obtain those from the dynamic susceptibility is hardly (if at all) feasible.

SAMENVATTING

Wat hebben bellen op onze frisdrankjes, hoopjes zeewier op een golvend zeeoppervlak, of zoals in dit proefschrift, drijvende balletjes op een oppervlaktegolf gemeen? Alle vertonen een groot aantal verschijnselen die er bijzonder eenvoudig uitzien, maar bij nadere beschouwing om een meer gedetailleerde bestudering vragen. Als we onze favoriete frisdrank in een glas gieten, ontstaan er veel belletjes aan de oppervlakte, die zich vrijwel allemaal meteen naar de wand van het glas verplaatsen, en zich daar verzamelen. Doen we nu hetzelfde in een plastic beker, dan zien we dat de belletjes midden op het oppervlak blijven drijven. Een hoeveelheid zeewier agglomereert en verplaatst zich voortdurend ten opzichte van de golven op het oppervlak. Drijvende deeltjes op een staande Faraday golf agglomereren, vertonen drift, en vormen als gevolg daarvan patronen.

In Hoofdstuk 2 laten we op basis van bestaande literatuur zien dat een macroscopisch bolletje op vier manieren kan drijven op een stilstaand vloeistofoppervlak, afhankelijk van zijn hydrofobiciteit en zijn dichtheid ten opzichte van die van de vloeistof. Deze vier mogelijkheden kunnen goed worden samengevat in een enkele vergelijking die de vorm van de meniscus rond het deeltje beschrijft, en de richting van de oppervlaktespanningskracht op het bolletje bepaalt. Verder tonen we aan dat een klein deeltje met een eindige contacthoek zowel in richting van een amplitudemaximum (buik) of minimum (knoop) van de staande golf kan afdrijven. In tegenstelling tot hetgeen in de literatuur is vermeld, vonden we dat als de meniscus convex is (en de oppervlaktespanning dus omhoog werkt) het deeltje in de richting van een buik drijft, terwijl een concave meniscus (met naar beneden gerichte oppervlaktespanning) het naar een knoop toe beweegt. Naast de drift is er een aantrekkingskracht tussen de drijvende deeltjes die veroorzaakt wordt door een combinatie van de zwaartekracht en de oppervlaktespanning. We analyseren ook deze tweede kracht die werkt op identieke macroscopische deeltjes op een bewegend vloeistofoppervlak.

In Hoofdstuk 3 beschrijven we onze waarneming dat dezelfde drijvende deeltjes die bij een lage deeltjesdichtheid ϕ clusters vormen op de buiken van de staande

golf, bij hoge ϕ juist rond de knooplijnen van de golf gaan clusteren. We hebben de overgang van het gedrag bij lage ϕ naar dat bij hoge ϕ systematisch onderzocht. Dankzij hogesnelheidsopnamen hebben we waargenomen dat, bij de inversie van het clusterpatroon bij de buiken in dat rond de knooplijnen, niet alleen de positie van de deeltjes maar ook hun dynamica verandert. De buikclusters ademen, wat wil zeggen dat de deeltjes periodiek naar de buiken toe en er vanaf bewegen waarbij de onderlinge afstand eveneens periodiek varieert. De clusters rond de knooplijnen vertonen dit soort ademend gedrag niet. Door de driftenergie, de attractieve capillaire energie, en het ademen te combineren, hebben we een energieberekening ontwikkeld waarmee we in staat zijn om de transitie van buik- naar knooplijnclusters te beschrijven. In deze berekening is het in rekening brengen van het ademend gedrag essentieel: zonder het ademen, vindt er geen transitie plaats.

Patroonvorming, emergentie, en zelforganisatie zijn fenomenen die in een veelheid aan gebieden zijn waargenomen, van geofysica tot biofysica. Gewoonlijk is de vorming of wijziging van een bepaald patroon terug te voeren op het variëren van een of meer controleparameters van het systeem. In ons systeem worden de controleparameters, de golflengte en amplitude van de staande golf, echter constant gehouden. De waargenomen patronen vormen, veranderen of inverteren alleen door het wijzigen van het aantal drijvende deeltjes per oppervlakte-eenheid. Hiermee onderscheidt ons systeem zich van de meeste andere die patroonvorming vertonen.

In Hoofdstuk 4, hebben we de op een staande Faraday golf waargenomen deeltjespatronen door het toepassen van zowel een lokale als een globale analyse gekarakteriseerd. Op globaal niveau hebben we een methode gebruikt die gebaseerd is op de Minkowski functionalen voor een puntverzameling. We hebben aangetoond dat dit een zeer nuttig instrument is voor het bestuderen van een veelheid aan eigenschappen, zoals clustergrootte, aspect ratio, en connectiviteit van de complexe deeltjespatronen. In een meer lokale context hebben we gekeken naar de zogeheten lokale bindingsordeparameter $\mid \Psi_6 \mid$, die een maat is voor de wijze waarop een tweedimensionale pakking afwijkt van de ideale hexagonale pakking, en tevens naar de paarcorrelatiefunctie $g(r)$. Ook al blijkt $\mid \Psi_6 \mid$ geen voldoende robuust instrument te zijn om onze, vaak sterk van de zeshoekige ideale vorm afwijkende, patronen te karakteriseren, het biedt uitstekende mogelijkheden om ze op een prachtige manier te illustreren. De paarcorrelatiefunctie $g(r)$ blijkt een betere manier om de steeds groter wordende lokale ordening voor toenemende ϕ te beschrijven. Kort samengevat hebben we de concentratie-afhankelijke deeltjespatronen als volgt kunnen karakteriseren: De ronde, onregelmatig gepakte buikclusters bij lage ϕ transformeren zich

in los gepakte, ketenvormige structuren voor gemiddelde ϕ, die vervolgens veranderen in dicht op elkaar gepakte netwerk-vormige knooplijnclusters bij hoge ϕ.

In Hoofdstuk 5 bestuderen we een nieuw regime, namelijk een dicht op elkaar gepakte monolaag van identieke deeltjes die wordt aangedreven met behulp van niet-lineaire chaotische Faraday golven met een golflengte in de orde van een deeltjesdiameter. In dit regime nemen we een deeltjesstroming waar die uit domeinen bestaat. Bij lage ϕ breken kleine groepen deeltjes die in eerste instantie gezamenlijk bewegen na enige tijd op. Dit proces herhaalt zich doorlopend. Tijdens het opbreken veranderen de groepen deeltjes zich zodanig dat de oorspronkelijk compacte en ronde groepen morfologisch dusdanig vervormen dat ze uitgroeien tot langgerekte, ketenvormige clusters. Voor gemiddelde en hoge waarden van ϕ speelt het opbreken een ondergeschikte rol en wordt de beweging van de deeltjesclusters gedomineerd door de morfologische vervorming die het gevolg is van het uitrekken. Om de daaruit voortvloeiende heterogene dynamica van de deeltjesclusters te karakteriseren, hebben we een morfologische methode ontwikkeld, die geïnspireerd is op de Minkowski puntverzameling aanpak uit Hoofdstuk 4. We hebben deze heterogene dynamica tevens met de vierpunts dynamische susceptibiliteit beschreven die ook in de literatuur al voor dit doel is gebruikt. Bij het vergelijken van de tijdschalen in onze morfologische benadering met die afkomstig van de dynamische susceptibiliteit vinden we kwalitatief een goede overeenstemming. Dit suggereert dat de morfologische benadering een waardevol alternatief zou kunnen zijn voor het bestuderen van dynamische heterogeniteit. Het zou zelfs een aanzienlijk sterker instrument kunnen zijn, omdat het niet alleen net als de susceptibiliteit de tijdschaal en de mate van heterogeniteit levert, maar ook veel informatie bevat over de dynamica van het systeem. Voorbeelden zijn de uitgebreide mogelijkheden voor visualisatie van de deeltjestroming (zie de achterzijde van de omslag van dit proefschrift), het karakteriseren van morfologische vervormingen in de tijd en de correlatie van de gelijktijdige beweging van vele deeltjes op het oppervlak. Met behulp van de dynamische susceptibiliteit is dit niet mogelijk.

Acknowledgements

I would like to express my deep gratitude to Devaraj van der Meer and Detlef Lohse. When I met with them, I was a student who attempted to do something new related with experimental fluid mechanics even though I had neither enough background in fluid mechanics nor in experimental physics. Their very instructive remarks, critical corrections, patience, and broad-minded attitude make me love this subject and love to be a PhD student.

Devaraj is the one who had to spend all hard times with me. The first two years, except for the comments related with the experimental part of the project, I never followed his suggestions. It was too difficult for me to picture how one can explain such a complex phenomenon by the drawings and equations he suggested. I began trusting him in my third year, and this is why I have Chapter 3 in this Thesis with a nice confirmation of our experimental observations. Since I listened to his suggestions completely during my fourth year, I have Chapter 5 with a simple, but a powerful tool, the morphological approach, in my Thesis. When I could not convince myself with his explanations, he made a zillion different connections related with my previous condensed matter background and social sciences. It took two and a half years, but I am now 75% convinced that one has to first start with a very toy model. His critical readings of my reports, manuscripts, and the Chapters of this Thesis, and very valuable suggestions before and after the oral presentations are unforgettable. Besides project-related stuff, he is always an open person to discuss and solve problems, with which one is faced during a PhD life. It is a great pleasure for me to study with him in my reasonably early career. I wish I keep the attitudes that I learned from him in my future career, as well.

Detlef is the one of the most broad-minded and patient persons that I met. He has the ability to study with people from anywhere and any kind of background. He has no rigid rules about people and research topics. The flexibility, freedom, and variety in the PoF group originates from his broad-minded perspective, and I will miss it a lot after leaving PoF. His valuable critics and completely reconstructing my presentation before my first serious talk gave me excellent tools to improve my pre-

sentation skills. His suggestions during my job applications were very useful, and as a consequence, I found the job which fits with my skills and wishes excellently. I am thankful to him for helping me to figure out my own way in the jungle of physics of fluids.

One shouldn't forget to thank to Mrs. Joanita Leferink. How many different problems this lady can solve very efficiently makes me always appreciative towards her. It is also so nice to see a nice lady in man-dominated society. Let me continue to thank Bas who solves a zillion different computer problems in a timely manner, Gert-Wim and Martin who are always kind and solve a large variety of technical problems that we face with doing experiments. I specially thank Martin for building my setup and dealing with lots of stuff related to the shaker.

I would like to express my gratitude to Stefan Luding and Kuniyasu Saitoh. After you became involved in the project, we have moved together and many hidden things in the system have become more clear. I am thankful to both for very useful discussions, and looking forward to further collaborations.

I would like to thank my gentle and helpful office friends Bram V., Ivo, Rajaram, and also my old office friend Erik. How many different questions did I ask you during my PhD times? Thanks a lot for your patience! Bram, Ivo, and Erik, your great help in my first two years mainly related with experiments and experimental equipment are unforgettable. Rajaram, you are the one who was exposed to my chaotic nature a lot. In first three years in my PhD, every morning I decided that I should not continue my PhD. After solving something in the afternoon, what I said to you is "no, we should continue". I do not even understand myself what kind of mood I had during the evenings. However, these tiring, repetitive cycles continued for a long time until my fourth year. Since I was really busy in this year, you were lucky that I did not find time to criticize anything. Thanks for all your motivating talks, and thanks for being a great friend.

Next, I want to thank the other gentlemen Edip, Koen and Jacco involved in teaching Physics of fluids course to Bachelor students. It was a valuable experience for me to adopt myself to a different educational system. Thanks a lot for your patience when I suggested "let's change this question, and make a new one". If I had realized that it would take that much time and effort, I would have never ever suggested it.

Let me further thank our former PostDoc Daniel, and PhDs Dennis and Julián, and our current PhDs Daniela, Hrudya, Tak, and Vivek for their always kind and friendly attitude. You are always open to discuss something new and exchange

ideas, which were very motivating and helpful for me. I am also thankful to Federico and Sander H. for nice movie nights at the Roomweg, which were enjoyable. Dear Enrique, Dear Mexican Charlie Chaplin, I did not know how much I could help you during your short stay in PoF as a student intern, but discussing something with you was always great for me. Thanks for being a very organized and efficient student. I am sure that you will do a very good job during your PhD in PoF. The movie that you made/acted in for Julián, is simply unforgettable. I can still laugh very heavily when I remember some scenes!

Before starting to thank my family members, I want to acknowledge the Stichting FOM both for funding this project and for organizing very useful courses during my PhD time, from which I learned a lot.

Dear Deniz, my dear husband, thanks a lot not only for cropping the experimental images for the front cover of this Thesis at the middle of the night, but also for all the useful suggestions, comments, and critical reviews related with this Thesis, my manuscripts, and presentations. However, the most thanks should go to the past colorful seven years! You really increase the quality of my life with your good heart. I am so sorry that you have now more white hairs compared to seven years ago. I promise that I force myself very much to be an easier person in Okinawa.

Sevgili ailem, Sevim, Mustafa, Sevgi ve Nadir...Herşey için çok teşekkür ederim. Sevim ve Mustafa, ilk Bilkent Üniversitesi'ne giderken beni siz götürmüştünüz. Her mutlu, heyecanlı ve kimi zaman da umutsuz anlarımda hep yanımdaydınız. Sevginiz, sabrınız, ve özveriniz için çok teşekkür ederim. Yaptıklarınızın bendeki anlamı inanın çok büyük.

Dear Rıfat Süha, even though we have been separated from each other for almost a decade, you are and have always been a very important person in my life. I am so thankful to you for all those great lectures that you taught in Bilkent Drama Atölyesi, and for how you always shared your life experiences in a honest way to force us to act with a maximum performance, both on the theatre stage and in real life. Maybe, because of that, after those lectures I became a completely different person. In addition, I still apply some of the practices that you gave. You suggested us one of the practices of Jack Nicholson as follows: He enters a super market with a black mask on his head and a gun in his hand, and asks one of the beautiful cashier ladies to give him all the money. She is terrified. When she attempts to give him the money he opens his mask and with his favorite smile, which we all know from his Hollywood movies, gives her a red rose. By doing so, he experiences all changes in her mimic and gesture. Of course, I perform this act using my own method, and

very much enjoy to realize how human reactions are so common from India to the Netherlands!

Ceyda Sanlı
Enschede,
The Netherlands
June, 2012

About the author

Ceyda Sanlı was born on the 9th of January 1983 in Kayseri in central Anatolia of Türkiye. She started the Savaştepe (Balikesir) Anatolian Teacher High School in 1996. In 1998, she moved to the Aksu (Antalya) Anatolian Teacher High School, and graduated from there in 2000. In the same year, she began her studies of fundamental physics at the Bilkent University, Ankara, Türkiye. There, she completed her Bachelor (2000-2006) and Master of Science in Physics (2006-2008).

During her Bachelor, she studied Langevin dynamics for classical and quantum open systems. In her Master, she tried to develop an analytical model to characterize the phase transition from ferromagnetism to paramagnetism in a nonequilibrium two-dimensional Ising system. In the summer of 2007, she visited the Theoretical Condensed Matter Department of the Tata Institute for Fundamental Research, Mumbai, India as a student intern. There, she studied Feynman diagrams and Green's function techniques to understand phase transitions in nonequilibrium quantum systems. In addition to this theoretical project, she attended variety of seminars given to all student interns. The seminars covered all fundamental physics branches from Astrophysics to Biophysics. In one of the great talks given by Prof. Deepak Dhar, her interest in fluid mechanics and granular matter began.

After graduating from the Bilkent Physics Department, she started her PhD project in the Physics of Fluids group, University of Twente in 2008 under the guidance of Dr. Devaraj van der Meer and Prof. Detlef Lohse.

Besides physics and fundamental science, she worked at the Bilkent University theatre, Drama Atölyesi, for two years (2000-2002) and afterwards at the theatre of the Nazim Hikmet house of culture (Ankara, 2003-2004). Her interest in performance art still continues. In addition, she is a fan of social media and politics. In her view, performance art and social media are the strongest tools available to humanity to protest against a large range of social unequal treatments and unjust regulations which one is confronted with in all parts of the world.

Propositions

accompanying the Thesis

FLOATERS ON FARADAY WAVES:
CLUSTERING AND HETEROGENEOUS FLOW

Ceyda Sanlı

6th of July 2012 at 16:45

1) Contrary to what is written in the literature, it is the meniscus, generated around a macroscopic sphere floating on a standing wave, which determines the wave drift: If the meniscus is convex the drift is towards the wave antinodes; on the other hand, if the meniscus is concave the drift is towards the wave nodes. *Chapter 2 of the Thesis*

2) The inversion of the pattern of floating particle clusters on a standing wave, from antinode clusters to node clusters, occurs by only adding more particles to the wave surface, without varying any other parameters. *Chapter 3 of the Thesis*

3) Without incorporating the breathing phenomenon into the antinode clusters, it is not possible to understand the transition from the antinode clusters to the node clusters. *Chapter 3 of the Thesis*

4) If one wants to employ a painting of M. C. Escher, one is advised to ask the opinion of Dutch colleagues in advance. *Chapter 4 of the Thesis*

5) Not all iterative terms in Feynman diagrams can be understood, and they may suggest unexplored subjects in theoretical physics.

6) We believe that our fundamental physics rules are valid in this world and all other parts of the universe. In this light, It is remarkable how many different opinions and suggestions professors can give about just a single plot in a presentation.

7) The flatness and beautiful depressive gray clouds of the Netherlands might be the origin of the creativity of the Dutch people for centuries: The flatness encourages continuously to think about infinity, the gray clouds stress that nothing, neither science nor art, can be simply represented by black or white.

8) Nature exhibits a variety of unpredictable dynamical events such as earthquakes; smart people having humanity in their inside know how to deal with them.

(On the 17th of August 1999, a 7.6 magnitude earthquake struck northwestern Turkey located mainly around the town İzmit. Approximately 20 thousand people died, in addition, 16 million people's lives were directly affected. The great majority of those buildings that became graves of people within a few seconds, including my friend Göknur Temiz, were younger than 10 years old and constructed by well-educated engineers! Since C. Sanlı stayed at the 35 years old house constructed by her grandfather who was a tailor, she can now defend this Thesis.)